8-2011

Transport and Optical Properties of Quantized Low-Dimensional Systems

Xiaoguang Li
xli22@utk.edu

To the Graduate Council:

I am submitting herewith a dissertation written by Xiaoguang Li entitled "Transport and Optical Properties of Quantized Low-Dimensional Systems." I have examined the final electronic copy of this dissertation for form and content and recommend that it be accepted in partial fulfillment of the requirements for the degree of Doctor of Philosophy, with a major in Physics.

Zhenyu Zhang, Major Professor

We have read this dissertation and recommend its acceptance:

Robert Compton, Adolfo Eguiluz, Thomas Papenbrock, Hanno Weitering

Accepted for the Council:

Carolyn R. Hodges

Vice Provost and Dean of the Graduate School

(Original signatures are on file with official student records.)

Transport and Optical Properties of Quantized Low-Dimensional Systems

A Dissertation

Presented for the

Doctor of Philosophy

Degree

The University of Tennessee, Knoxville

Xiaoguang Li

August 2011

Dedicated to my wife Ruochen

Acknowledgements

My utmost gratitude goes to my PhD advisor, Dr. Zhenyu Zhang, for his comprehensive guidance and enormous inspirations. I feel very fortunate to have an advisor who gives me the opportunity to enjoy physics and also tells me how to start my career as a researcher.

I am pleased to thank the members of my doctoral committee, Dr. Robert Compton and Dr. Adolfo Eguiluz, for reading the drafts of this dissertation and providing many valuable comments that improved the contents of this dissertation; Dr. Thomas Papenbrock, who also serves on my computational minor committee, for his guidance in computational skills; Dr. Hanno Weitering, for useful discussions.

My thanks go to my collaborators, Dr. Di Xiao, for regular discussions that helped me sort out the technical details of my work; Mr. Hua Chen, for daily discussions on a wide range of interesting topics; Mr. Ao Teng, for providing me with stimulating experimental data.

My graduate studies would not have been the same without Dr. Ke Zhao, who was my labmate and now is at Rice University, and Dr. Yuri Kamyshkov. They introduced me to my advisor, Dr. Zhenyu Zhang, and encouraged me throughout my period of PhD study.

I would also like to thank Dr. Ted Barnes for his guidance in my earlier PhD study providing me the foundation in research. Although his decision to leave the University of Tennessee caused a great deal of suffering for me at the time, in the long run, his passion and persistence in physics still impress me. Additionally, I am grateful to

Dr. Winston Robert at the Florida State University for detailed discussions of high energy physics.

My thanks also go to my other labmates, Dr. Wenguang Zhu, Dr. Claudia Troparevsky, Mr. Guo Li, Ms. Guangfen Wu, Mr. Wei Chen, and Mr. Robert Van Wesep, for valuable discussions.

Finally, and most importantly, my deepest gratitude goes to my family for their unflagging love and support, especially my wife Ruochen whose understanding and encouragement enable me to complete this dissertation.

Abstract

In this thesis, we present a systematic investigation of the static and dynamic response properties of low-dimensional systems, using a variety of theoretical techniques ranging from time dependent density functional theory to the recursive Green's function method.

As typical low-dimensional systems, metal nanostructures can strongly interact with an electric field to support surface plasmons, making their optical properties extremely attractive in both fundamental and applied aspects. We have investigated the energy broadening of surface plasmons in metal structures of reduced dimensionality, where Landau damping is the dominant dissipation channel and presents an intrinsic limitation to plasmonics technology. We show that for every prototype class of systems considered, including nanoshells, coaxial nanotubes, and ultrathin films, Landau damping can be drastically tuned due to energy quantization of the individual electron levels and e-h pairs. Both the generic trend and oscillatory nature of the tunability are in stark contrast with the expectations of the semiclassical surface scattering picture.

For a more realistic environment of low-dimensional systems, the effect of a dielectric substrate is considered to mimic the experimental setup. We have studied the dispersion of various plasmon excitations in metal thin films with growth substrates. Our results qualitatively reproduce the experimentally observed plasmon spectra of the Mg/Si systems. The underlying physics for the formation of various absorption peaks can be understood with a simple hybridization concept. Based on

this concept, the coexistence of surface and bulk plasmons in experimental observation turns out to be a clear evidence for the existence of multiple-multipole surface plasmons due to the quantum confinement in thin films.

To step into more confined worlds, we choose the real two-dimensional material graphene as our representive system, which is a semi-metal with zero band-gap. As the first step, the static electric response of graphene is investigated by exploring its transport properties. We have studied the pseudospin valve effect in bilayer graphene nanoribbons. The pseudospin degree of freedom is associated with the electron density in two layers and can be controlled by external gate electrodes. We find that the conductance of nanoribbons shows different behaviors compared with infinite systems due to the appearance of edge states and quantum confinement. Remarkably, a large on-off ratio can be achieved in nanoribbons with zigzag edges, even when the Fermi energy lies in the bulk energy gap. The influence of possible edge vacancies and interface conditions is also discussed.

Finally, we discuss the possibility of using plasmon excitations to detach the graphene from its growth substrate, where the dynamic electric response of the graphene-metal system is expected to play a central role.

Contents

List of Figures

Chapter 1

Introduction

Both the transport and optical properties of a material describe the response of its enclosed particles (mainly electrons) to an external electric field. Previously, measurements of the corresponding macroscopic response signals have provided information on the microscopic world. Recently, improved fabrication techniques have offered a reversed routing that can effectively control the macroscopic response by engineering the microscopic contents [4, 5]. The studies of physical properties, in the so-called low-dimensional systems, then are not only fundamentally interesting, but also technologically attractive. In this chapter, we first introduce a variety of interesting physical properties of low-dimensional systems, and then focus on the transport and optical properties, to show the important role of quantum mechanics in these systems.

1.1 Physical Properties of Low-Dimensional Systems

Low-dimensional systems refer to materials that are strongly confined in at least one dimension. Examples include semiconductor quantum wells, heterostructures, thin films, nanowires, nanotubes, quantum dots, nanoparticles, etc. The physical

properties in these systems are expected to deviate significantly from their bulk counterparts due to quantum size effects and boundary effects, and also differ from their enclosed atoms due to many-body interactions.

The quantum size effect plays an extremely important role in low-dimensional systems. Within a simple particle-in-box model, we illustrate one example in Fig. 1.1, where the electron density of states, $n(E)$, is evaluated in structures of different reduced dimensionality. For a noninteracting electron gas in $3D$, we have the relation $n(E) \propto \sqrt{E}$. As for low-dimensional cases, $n(E)$ includes the contribution from both the quantized energy levels and their corresponding continuous compensations in extended direction, and eventually shows the discontinuous behavior. The completely different $n(E)$ implies the qualitative contrast between the bulk and low-dimensional systems, since the density of states has a major impact on many physical properties, such as the transport, magnetism, and optical absorption. One readily can see one example by noticing that the electrons in a semiconductor conduction band can be described by the noninteracting electron gas model. When the confinement modifies the density of states from $3D$ to $2D$, the energy increase of the band bottom indicates the change of the optical absorption energy of the semiconductor material.

Another important issue of the low-dimensional systems is the appearance of a boundary. The boundary, dividing materials with different physical properties, provides many unique phenomena, which occur along the boundary itself or sometimes even across the boundary involving the whole system.

Since the $3D$ electronic band structures are forced to change from one material to another, a special state usually exists in the atom layers close to the boundary. This so-called boundary (surface) state, widely existing at metal-vacuum interfaces and semiconductor heterostructures, serves as the main resource for a two-dimensional electron gas [6]. The topological insulator [7], which has become one of the hottest topics in recent years, is another example of the boundary effect. Essentially, the insulators can be classified into different topological groups. When we join two insulators from different topological groups, the electronic bandgap has to be closed

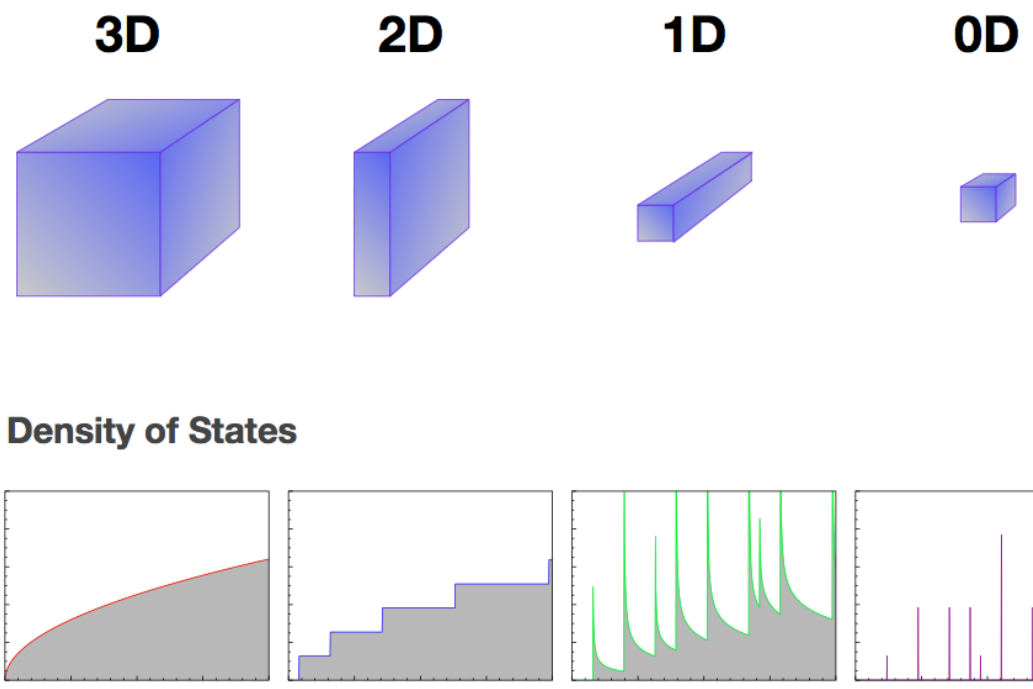

Figure 1.1: Electron density of states of different dimensionality within free electron gas model.

and reopened from one side to the other, which implies the existence of a remarkable conductive band at the boundary between the two insulators.

The boundary also can serve as a domain wall in a system, which sometimes will drastically change the physical properties of the whole system. When the boundary separates two ferromagnetic regions with parallel (P) or antiparallel (AP) magnetization, the conductance G perpendicular to the boundary will show a large conductivity ratio G_P/G_{AP} [8]. This is the so-called giant magnetoresistance effect [9] which is widely used in today's hard disk drives. In addition, the conductance across a metal-semiconductor junction can become asymmetric due to the Schottky barrier [10], which is caused by the electron redistribution at the boundary. This property has been used for manufacturing the Schottky diode [11] instead of the traditional semiconductor p-n junction diode. Moreover, people are attemping to use this special junction for the photocurrent generation [12]. In next section, we will get into more details of the boundary effect on optical properties.

On the other hand, it is the many-body interaction that gives the low-dimensional systems different properties from its constituent. The change of dimensionality has a large impact on the interaction between the electrons and other excitations. For instance, Luttinger liquid theory [13] is needed in a $1D$ system instead of the widely used Fermi liquid theory. Some physical effects, such as metal-insulator transition [14], Kohn anomaly [15], Friedel oscillation [16], etc, become more pronounced in low-dimensional systems due to the many-body interaction.

In the following of this chapter, we focus on the transport and optical properties to see briefly how they will be changed in low-dimensional systems.

1.2 Optical Properties in Nanostructures

The optical properties of materials refer to the response of materials to electromagnetic fields. They are important because they can tell us how to manipulate light to carry information in materials or how to use light to detect the materials.

Understanding of the optical properties of materials begins from the reflection and refraction of light on the interface of different materials. These phenomena are described by the complex refractive index $N = n + ik$, which tells us how the light will be scattered at interface and travel in materials. Many interesting phenomena relate to those properties, such as light with different colors have different refraction angles, the insulators are usually transparent, metals are used to make mirrors, etc.. The physics behind those phenomena is that materials respond differently to the light with different frequencies. Microscopically, this is related to the interaction between the light and electrons in a material. These interactions including the scattering and absorption of light are usually described with the dielectric function of material $\epsilon = \epsilon_1 + i\epsilon_2$.

In recent years, the optical properties in low-dimensional systems have attracted a lot of attentions mainly because of the existence of surface plasmons [17]. Plasmons refer to collective excited states of electrons in materials, and play a crucial role in the optical response of systems. The surface plasmon is one kind of plasmon state that is localized on the boundary of systems. The most attractive aspect of surface plasmons is that it can be strongly coupled with light, offering pronounced electric field enhancement near the boundary, and therefore results in a slew of intriguing phenomena and potential applications. The corresponding technology, plasmonics, is widely used in a variety of aspects, including the surface enhanced Raman spectroscopy (SERS) [18, 19], metamaterial [4, 5], solar cells [20], etc.

In 1952, David Pines and David Bohm [21] indicated the existence of collective motion of electrons in a dense electron gas (Fig. 1.2(b)). This so-called *bulk plasmon* mode has a characteristic frequency around $\omega_p = \sqrt{4\pi ne^2/m_e}$ depending on the electron density n and effective mass m_e in the material. In fact, before this theoretical study, evidence for this special mode was detected in the experiment of energy loss of electrons as they pass through metal thin films [1]. Fig. 1.2(a) shows the quantized energy loss spectra, implying the existence of new absorption mode. However, what really stimulates today's plasmonics is the surface plasmon.

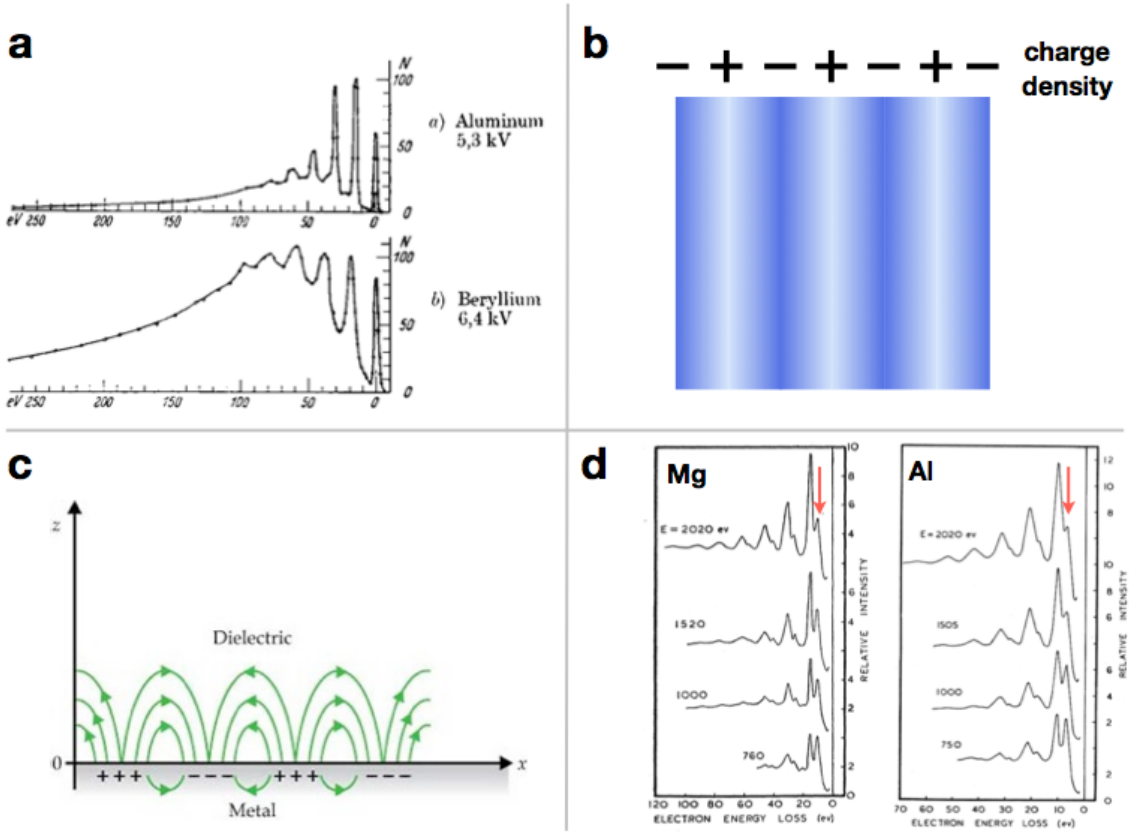

Figure 1.2: (a) Bulk plasmons of Al and Be measured by electron energy loss spectroscopy (EELS) [1]. (b) Charge density oscillations of bulk plasmons. (c) Charge density oscillations and induced electric fields of surface plasmons. (d) Surface and bulk plasmons of Mg and Al measured by EELS (Small shoulders aside huge the bulk plasmon peaks marked by the red arrows are due to the surface plasmon absorptions.) [2, 3].

In 1957, Rufus Ritchie discovered the concept and theory of surface plasmon [22]. After two years, this prediction was confirmed by a series of experiments (Fig. 1.2(d)). As shown in Fig. 1.2(c), a surface plasmon is the electron collective motion existing at a metal surface (strictly speaking at an interface between two materials with opposite-sign dielectric constants). Its frequency depends on the geometry of the corresponding interface. For example, for a flat surface this frequency is $\omega_p/\sqrt{2}$, and for a spherical nanoparticle many different modes exist following the formula $\omega_p\sqrt{l/(2l+1)}$ [17].

After briefly going through the history and applications of plasmons, we turn to its theoretical framework. The earliest analysis for the bulk plasmon by Pines and Bohm was based on quantum mechanical studies, where the plasmon mode is ascribed to electron collective oscillation due to the long-range Coulomb interactions, and the individual electron oscillations are thus governed by short range screened Coulomb potential with the Yukawa potential form [23]. Surface plasmon, on the other hand, can be described by classical electromagnetic theory. In Ritchie's paper, he predicted surface plasmon with a classical method, even though he mentioned the possible quantum approach. Later Peter Feibelman [24] showed a more rigorous result with quantum mechanics. However, many researchers still like to use classical methods, because in most cases the dielectric function can describe the response of system very well, and therefore makes the classical theory accurate enough. Also, presently the powerful computer can describe the plasmon in very complex systems with classical methods, such as the finite-difference time-domain method (FDTD). For those systems, the quantum study, involving the much larger electronic degrees of freedom, is too expensive to be used.

However, as will be shown in Chapter 3, when electronic structures are strongly affected by confinement, a simple dielectric function will not be good enough to describe the response of the system. Then more accurate quantum studies are required. One of our purpose in this thesis is by using some highly symmetric prototype systems to seek the unique properties, which are only able to be explored

with quantum analysis. Then by carefully manipulating these building blocks, we can take the plasmonics into the quantum age.

1.3 Transport Properties in Mesoscopic Systems

Right after the discovery of electron, a classical model was proposed in 1900 by Paul Drude [25] to explain the microscopic origin of Ohm's law. In the Drude model, driven by the external electric field, the electrons are moving in the material and are constantly scattered by ion cores to obtain resistivity. The current then is derived as

$$\mathbf{J} = \sigma \mathbf{E}, \quad \sigma = \frac{ne^2\tau_m}{m}, \tag{1.1}$$

where n,e,m are, respectively, the density, charge, and mass of electron, and τ_m is the mean time interval of scattering events. This model is a successful attempt to connect the microscopic quantity with macroscopic observable, and the idea of the mean free path l_m depending on the $v\tau_m$ is still used in today's theory, where v is the average velocity of free electrons. However, this model encounters serious problems when the temperature dependence is considered and the ion scattering picture of the resistivity is not accurate [26].

Following the development of quantum mechanics in 1920s, Sommerfeld applied the Fermi-Dirac distribution to electrons instead of the Boltzmann distribution used in Drude model. This change turns out to be very successful in explaining the observed temperature dependence. It tells us that only the electrons around the Fermi level participate in the conduction. Thus, instead of using the average velocity of free electron v, we should use the Fermi velocity v_F to define the mean free path $l_m = v_F\tau_m$.

In low-dimensional systems, we consider not only the Fermi-Dirac distribution of a quantum system, but also the wave-like property of electrons, essentially, the phase coherence of the wavefunction. Due to the reduced dimensionality, the scale of system L may become comparable with the phase relaxation length of electron l_ϕ. In this

so-called *mesoscopic system* [27], quantum interference becomes very important, and electrons behave like waves rather than classical pinballs.

The electron scattering events in materials can be divided into elastic and inelastic scattering. Elastic scattering includes the scattering with static impurity, which will not destroy the phase coherence since the phase shift is uniquely determined by the scattering source. On the other hand, inelastic scatterings include the scattering with phonons, other electrons, and impurities with relevant degree-of-freedom, which washes out the phase information of the electrons. We thus can define the corresponding mean free path as l_{el} and l_{in}, and recognize the different transport regimes based on various characteristic lengths. For example, at low temperature, we usually have $l_{el} < l_{\phi} < l_{in}$.

When the Fermi wavelength l_F is comparable with l_{el}, we encounter the effect of Anderson localization, which means the conductivity is zero. When $l_{in} < L$, we have the normal macroscopic conductivity, following the Ohm's law. However, when $l_{el} < L < l_{\phi}$, we encounter the mesoscopic system, where phase coherence and the elastic scattering produce the weak localization effect, providing resistivity to the system. If we go one more step to shrink the size of a system to satisfy $L < l_{el}$, electrons will not be scattered in the whole device region. The conductivity is then simply described by the Landauer formula [28],

$$G = \sum_i n_i \frac{e^2}{h} |T_i|^2, \tag{1.2}$$

where n_i and T_i are the density of state i and its transmission rate across the whole system including the electrodes. This conductivity formula in the so-called *ballistic transport* regime can be understood by analogy with the light transmitting through a glass or electron traveling across a potential well, where the "resistivity" essentially comes from the boundaries.

1.4 Outline of the Thesis

In the following part of this thesis, I will check into more details of the aforementioned topics, and introduce the theoretical and numerical methods used to study those problems. Essentially, we examine how the quantum size effect will affect the transport and optical properties of materials.

In the next chapter, various methods are introduced, including the tight-binding model, (time dependent) density functional theory, and Green's function method.

Chapter 3 investigates the quantum size effect of plasmons in metal nanostructures. I will start with a general introduction for the current theories, including the classical EM field calculation and the hydrodynamic model. The detailed formalism in the quantum studies will be presented following the methodologies introduced in chapter 2. The advantage of quantum studies will be shown in the last section, where we apply it to different metal nanostructures and show intriguing results for both energy and linewidth of plasmons.

In chapter 4, we study various plasmon modes in more realistic systems, where the contribution of dielectric environments is considered.

The static electric properties of the real two-dimensional material graphene are investigated in chapter 5. I will introduce some basic knowledge of graphene, and then use the recursive Green's function method to study transport properties of a confined system, bilayer graphene nanoribbon, where an intriguing pseudospin valve effect is presented.

The prospectives of current studies are presented in chapter 6.

In appendixes, I will show some details of our calculations and my publications in high energy physics.

Chapter 2

Methodologies

2.1 Density Functional Theory

The ground state of a many-body system can be well explored through the density functional theory (DFT). The concept of DFT originated from the Thomas-Fermi model, while its theoretical foundation was laid in two theorems derived by Hohenberg and Kohn in 1964 [29]. The Hohenberg-Kohn theorems state that the ground state properties of a many-electron system are uniquely determined by the electron density, and there exists a universal energy functional with respect to electron density, such that the exact ground state density can be found by minimizing this energy functional. These are very powerful results since they offer an opportunity to reduce the many-body problem of N electrons with $3N$ spatial coordinates to electron density with only 3 spatial coordinates. After the Hohenberg-Kohn theorems, Kohn and Sham developed a simple scheme to carry out DFT calculations by solving the so-called Kohn-Sham equation [30].

Within the Kohn-Sham (KS) scheme, one studies a system of non-interacting electrons that generate the same electron density as the real interacting electrons. The non-interacting electrons move in an effective KS potential $V_{eff}[n](\mathbf{r})$, including the mean-field Hartree potential $V_H[n](\mathbf{r})$ and the additional many-body correction

$V_{xc}[n](\mathbf{r})$. The functional $V_{eff}[n](\mathbf{r})$ depends on the electron density distribution $n(\mathbf{r})$, which can be obtained by summing up the density contributions from occupied individual electronic states

$$n(\mathbf{r}) = \sum_{i=occ} |\psi_i(\mathbf{r})|^2, \tag{2.1}$$

where, inversely, the wavefunction of individual electronic state $\psi_i(\mathbf{r})$ can be solved from KS equation

$$\left(-\frac{\nabla^2}{2} + V_{eff}[n](\mathbf{r})\right)\psi(\mathbf{r}) = \epsilon_i\psi(\mathbf{r}). \tag{2.2}$$

Therefore, by self-consistently solving Eq. (2.1) and (2.2), we can finally arrive at the ground state density.

2.2 Green's Function Methods

The Green's function is a useful tool to solve linear differential equations subject to the special boundary condition. Essentially, a Green's function builds up a mapping from boundary conditions to corresponding solutions through an integration. In a physical system described by a certain differential equation, the boundary condition and solution usually have a clear physical meaning. The Green's function then offers a very intuitive way of describing their connection. Here, we introduce the applications of the Green's function from classical to quantum systems. In later sections, we will show its usages in the studies of both transport and optical properties.

2.2.1 Classical Green's functions

In classical studies, even though you may not be familiar with this terminology, you must use some Green's functions many times. One example is the Coulomb interaction, which is the Green's function of the Poisson equation

$$\nabla^2\phi(r) = 4\pi n(r), \tag{2.3}$$

where $n(r)$ is the charge density and $\phi(r)$ is the electric potential field. The Green's function is defined to be the solution with a delta-function boundary condition as

$$\nabla_r^2 G(r, r') = \delta(r - r'). \tag{2.4}$$

Then as we mentioned before, this function builds up a direct mapping from $n(r)$ to $\phi(r)$,

$$\phi(r) = \int dr' G(r, r') 4\pi n(r'). \tag{2.5}$$

This is an explicit expression of Coulomb potential. To get $G(r, r')$, we first transfer Eq. (2.4) into k-space,

$$-k^2 G(k) = 1. \tag{2.6}$$

Clearly $G(k) = -1/k^2$, then its r-space form can be obtained as

$$\begin{aligned} G(r, r') &= -\int \frac{d^3k}{(2\pi)^3} \frac{e^{ik\cdot(r-r')}}{k^2} = -\int \frac{dk d\cos\theta}{(2\pi)^2} e^{ik\cdot|r-r'|\cos\theta} \\ &= -\int \frac{dk}{(2\pi)^2} \frac{2\sin k|r-r'|}{k|r-r'|} = \frac{1}{4\pi} \frac{1}{|r-r'|}. \end{aligned} \tag{2.7}$$

Finally, we obtain a familiar expression for the coulomb interaction,

$$\phi(r) = \int dr' \frac{n(r')}{|r-r'|}. \tag{2.8}$$

This is a simple example of Green's functions. We will discuss its connection with a quantum example later.

2.2.2 Quantum single particle Green's functions

In quantum mechanics, Green's functions are handy to deal with perturbations. For example, in the Schödinger equation

$$H\psi = (H_0 + V)\psi = \epsilon\psi, \tag{2.9}$$

where the total Hamiltonian H is divided into an easily solvable part H_0 and a small perturbation V. We can consider $V\psi$ as the boundary condition, or a source term, as its role in our previous classical example. To solve the differential equation

$$(\epsilon - H_0)\psi = V\psi, \tag{2.10}$$

we can first obtain its Green's function from

$$(\epsilon - H_0)G_0(r, r', \epsilon) = \delta(r - r'). \tag{2.11}$$

There are some *differences* between this quantum case and the previous classical example. First, without the source, i.e. $V = 0$, we have the field ψ_0 solved from

$$(\epsilon - H_0)\psi_0 = 0. \tag{2.12}$$

Here, generally $\psi_0(r) \neq 0$ and should be considered as a background field contributing to the total field. In our classical example, we can also have a background field, such as a constant. However, there is no specific physical meaning for that. The total field $\psi(r)$ now should be written as

$$\psi(r) = \psi_0(r) + \int dr' dr'' G_0(r, r', \epsilon) \left[V(r', r'')\psi(r'')\right], \tag{2.13}$$

where we note another difference from the second term. Since the source term in this quantum case relates to the field itself, the field can only be obtained by self-consistent iteration.

We can of course define the Green's function directly as

$$(E - H_0 - V)G(r, r', \epsilon) = \delta(r - r'). \tag{2.14}$$

Then, conversely we obtain

$$\psi_0 = \psi + G(-V\psi_0) \Rightarrow \psi = \psi_0 + GV\psi_0, \tag{2.15}$$

where, for simplicity, we ignore the integrals by just considering them as matrix multiplications. By comparing Eq. (2.13) and (2.15), We can obtain the Dyson equation, which connects G_0 and G,

$$GV\psi_0 = G_0V\psi_0 + G_0VG_0V\psi_0 + \cdots \Rightarrow G = G_0 + G_0VG. \tag{2.16}$$

Then G can be written explicitly as

$$G = \frac{G_0}{1 - G_0V}. \tag{2.17}$$

This is a very useful relation, since it provides a way to obtain G by simply solving H_0. In the next section, we will see that for a time dependent H, we can always extract the time independent part H_0, leaving $V(t)$ as the perturbation.

2.3 Time Dependent Density Functional Theory

We will show in this section the reason that we need a time dependent theory and the way to derive it. Combining it with the density functional theory of ground states introduced in the section 2.1, the time dependent density functional theory can be obtained to deal with excited states of the system.

2.3.1 Absorption and excited states

The response properties of systems provide the information of their internal degrees of freedom. Energy absorption (or dissipation) is one of these response properties directly reflects the energy difference between the ground state?? and excited states.

Before going through a long rigorous derivation in the next section, we first build up the relation between the absorption and excited states with a very intuitive way. Assuming an external field $V_{ext}(t) = V_0\delta(t)$ acting on the system, the absorption can be readily written as

$$S(\omega) = \sum_f \omega \left|\langle f|V_0|i\rangle\right|^2 \delta(E_f - E_i - \omega), \tag{2.18}$$

where $|i\rangle$ and $|f\rangle$ are the initial and final states of the system, respectively. The physics is that $|\langle f|V_0|i\rangle|^2$ indicates the possibility for the system to jump from the ground state to a certain excited state, and the delta function ensures energy conservation in this process. The total absorption is thus simply calculated as the summation of contributions from all available channels.

We now go through the linear response theory to build up the time dependent framework, which is crucial for both transport and optical properties.

2.3.2 Linear response theory

The linear response theory describes the response of systems to time dependent external perturbations. The final goal is to find the intrinsic quantity of a system usually called susceptibility, which connects the response and the perturbation through a linear relation. To understand this, we start from a simple classical example, the Lorentz oscillator model, where we consider a set of noninteracting electrons, acting as classical harmonics oscillators with frequency ω_0 due to confinement and also affected by a frictional force proportional to their velocity $\dot{x}$ as $m\gamma\dot{x}$. Generally, the harmonics approximation is true for small displacement x of electrons, and the linear frictional force is also a good approximation in many cases. Now, we calculate their behaviors under an external electric field E_{ext}. For each electron, we have the equation of motion

$$\ddot{x} + \gamma\dot{x} + \omega_0^2 x = \frac{eE_{ext}}{m}. \tag{2.19}$$

Assuming $x(\omega,t) = x_0(\omega)e^{-i\omega t}$ and $E_{ext}(\omega,t) = E_0(\omega)e^{-i\omega t}$, this equation can be readily solved in the frequency domain as

$$x_0(\omega) = \frac{e}{m}\frac{E_0(\omega)}{-\omega^2+\omega_0^2-i\gamma\omega}. \tag{2.20}$$

Assuming the density of electron is n, we obtain the polarization

$$P = nex_0(\omega) = \epsilon_0\frac{\omega_p^2}{-\omega^2+\omega_0^2-i\gamma\omega}E_0(\omega) = \epsilon_0\chi(\omega)E_0(\omega), \tag{2.21}$$

where $\chi(\omega)$ is exactly the electric susceptibility of the system and ϵ_0 is vacuum permittivity introduced conventionally to make $\chi(\omega)$ dimensionless;

$$\omega_p^2 = \frac{ne^2}{\epsilon_0 m} \tag{2.22}$$

is a very important quantity, which will be discussed later in the optical studies. We now keep only the real part of E_{ext} and x to calculate the energy dissipation, which indicates the strength of the coupling between external field and the electronic system. Suppose the external field is

$$\tilde{E}_{ext}(\omega,t) = E_0(\omega)\cos\omega t. \tag{2.23}$$

Then the displacement is

$$\tilde{x}(\omega,t) = \frac{\epsilon_0 E_0(\omega)}{ne}\left[Re\chi(\omega)\cos\omega t + Im\chi(\omega)\sin\omega t\right]. \tag{2.24}$$

The average energy absorption rate is calculated through

$$\begin{aligned}\bar{P}(\omega) &= \frac{ne}{2\pi}\int_0^{2\pi} dt\tilde{E}_{ext}(\omega,t)\dot{\tilde{x}}(\omega,t) = \frac{1}{2}\epsilon_0\omega Im\chi(\omega)E_0^2(\omega)\\ &= \frac{\epsilon_0 E_0^2(\omega)}{2}\frac{\gamma\omega^2\omega_p^2}{(\omega^2-\omega_0^2)^2+\gamma^2\omega^2}.\end{aligned} \tag{2.25}$$

This result states the relation between absorption and susceptibility, essentially the dynamic response function. Actually, we can calculate the energy dissipation directly using a complex external field by

$$\bar{P}(\omega) = \frac{1}{2\pi} Re \int_0^{2\pi} dt\, eE_{ext}(\omega, t)\dot{x}^*(\omega, t) = \epsilon_0 \omega Im\chi(\omega) E_0^2(\omega). \tag{2.26}$$

The reason that we go through the previous procedure is to show the energy dissipation due to out-of-phase motion of the oscillators by comparing Eq. (2.23) and (2.24) . In the following of this section, we will derive the quantum response function in the linear response theory, which gives a similar relation with exactly the same underlying physics.

In quantum mechanics, we consider a many-electron system described by *time independent* Hamitonian H_0. Starting from time t_0, this system is perturbed by a *time dependent* external field $V_{ext}(t)$. The total Hamiltonian can thus be written as

$$H(t) = H_0 + V(t)\Theta(t - t_0). \tag{2.27}$$

The linear response theory describes the response of a system to an external perturbation in linear regime. The response is quantified by measuring the change of the expectation value of a certain observable X,

$$\langle X(t)\rangle - \langle X\rangle_0 = \sum_a n_a \langle\psi_a(t)|X|\psi_a(t)\rangle - \sum_a n_a \langle\psi_a(0)|X|\psi_a(0)\rangle\,, \tag{2.28}$$

where the wavefunction $|\psi_a(t)\rangle$ is under the schrödinger picture following the relation

$$i\partial_t |\psi_a(t)\rangle = H(t)\,|\psi_a(t)\rangle\,. \tag{2.29}$$

Considering the wavefunction $\left|\bar{\psi}_a(t)\right\rangle$ within interaction picture we have

$$\left|\bar{\psi}_a(t)\right\rangle = e^{iH_0 t}\,|\psi_a(t)\rangle = e^{iH_0 t}e^{iH(t-t_0)}e^{-iH_0 t_0}\left|\bar{\psi}_a(t_0)\right\rangle = \bar{U}(t, t_0)\left|\bar{\psi}_a(t_0)\right\rangle, \tag{2.30}$$

where $\bar{U}$ is defined to describe the evaluation of $\left|\bar{\psi}_a(t)\right\rangle$ and we should notice that $\left|\bar{\psi}_a(t_0)\right\rangle = |\psi_a\rangle$. The reason to use the interaction picture is that both wavefunctions and $\bar{U}(t,t_0)$ can be explicitly determined by the perturbation $\bar{V}(t)$ as

$$i\partial_t \left|\bar{\psi}_a(t)\right\rangle = i\partial_t \left[e^{iH_0 t}\left|\psi(t)\right\rangle\right] = e^{iH_0 t}(-H_0 + H)\left|\psi(t)\right\rangle = \bar{V}\left|\bar{\psi}_a(t)\right\rangle, \tag{2.31}$$

and

$$i\partial_t \bar{U}(t,t_0) = i\partial_t \left[e^{iH_0 t}e^{-iH(t-t_0)}e^{-iH_0 t_0}\right] = e^{iH_0 t}Ve^{-iH(t-t_0)}e^{-iH_0 t_0} = \bar{V}(t)\bar{U}(t,t_0). \tag{2.32}$$

Integrating both sides from time t_0 to t, we get

$$\bar{U}(t,t_0) = 1 + \frac{1}{i}\int_{t_0}^{t} dt'\bar{V}(t')\bar{U}(t',t_0) \simeq 1 + \frac{1}{i}\int_{t_0}^{t} dt'\bar{V}(t'). \tag{2.33}$$

Now, inserting $|\psi_a(t)\rangle$, extracted from Eq. (2.30), into Eq. (2.28) yields

$$\begin{aligned}
\langle X(t)\rangle - \langle X\rangle_0 &= \sum_a n_a \left\langle \psi_a|\bar{U}(t_0,t)\bar{X}(t)\bar{U}(t,t_0)|\psi_a\right\rangle - \langle X\rangle_0 \\
&\simeq \frac{1}{i}\int_{t_0}^{t} dt' \sum_a n_a \left\langle \psi_a|\bar{X}(t)\bar{V}(t') - \bar{V}(t')\bar{X}(t)|\psi_a\right\rangle \\
&= \frac{1}{i}\int_{t_0}^{t} dt' \left\langle [\bar{X}(t),\bar{V}(t')]\right\rangle_0 .
\end{aligned} \tag{2.34}$$

We now try to divide this result into two parts, the intrinsic property of system and the external field. Suppose V depends on the quantity Y of the system and the external field F_{ext} as

$$V(t) = Y(t)F_{ext}(t)\Theta(t-t_0). \tag{2.35}$$

Then setting $\tau = t - t'$ in Eq. (2.34), we get

$$\begin{aligned}
\delta\langle X(t)\rangle &= \langle X(t)\rangle - \langle X\rangle_0 \\
&= \frac{1}{i}\int_0^{t-t_0} d\tau \left\langle [\bar{X}(\tau),\bar{Y}]\right\rangle_0 F_{ext}(t-\tau)\Theta(t-\tau-t_0).
\end{aligned} \tag{2.36}$$

If we assume $t_0 \to -\infty$ and insert another function $\Theta(\tau)$, we obtain

$$\delta \langle X(t) \rangle = \frac{1}{i} \int_{-\infty}^{\infty} d\tau \Theta(\tau) \left\langle [\bar{X}(\tau), \bar{Y}] \right\rangle_0 F_{ext}(t-\tau) = \chi_{XY} * F_{ext}(t), \tag{2.37}$$

where $*$ stands for the convolution of F_{ext} and the response function

$$\chi_{XY}(t) = \frac{1}{i} \Theta(t) \left\langle [\bar{X}(t), \bar{Y}] \right\rangle_0 . \tag{2.38}$$

The physics here is that $\chi_{XY}(t)$ indicates the intrinsic response property of the system as a device, and F_{ext} is the external perturbation as the input signal. Therefore, as shown in Eq. (2.37), their convolution gives the response of this system. Now, suppose $F_{ext}(t) = F_0(\omega) e^{-i\omega t}$, in frequency domain then we arrive at the same relation as in the classical example Eq. (2.21),

$$\delta X(\omega) = \chi_{XY}(\omega) F_0(\omega), \tag{2.39}$$

where $\chi_{XY}(\omega)$ can be readily derived as

$$\begin{aligned}
\chi_{XY}(\omega) &= -i \int_0^{\infty} dt' \left\langle [\bar{X}(t'), \bar{Y}] \right\rangle_0 e^{i(\omega + i\eta)t'} \\
&= -i \int_0^{\infty} dt' \sum_{a,b} f_a \Big[\left\langle a|\bar{X}(t')|b \right\rangle \left\langle b|\bar{Y}|a \right\rangle - \left\langle a|\bar{Y}|b \right\rangle \left\langle b|\bar{X}(t')|a \right\rangle \Big] e^{i(\omega + i\eta)t'} \\
&= -i \int_0^{\infty} dt' \sum_{a,b} f_a \Big[X_{ab} Y_{ba} e^{i(\epsilon_a - \epsilon_b + \omega + i\eta)t'} - Y_{ab} X_{ba} e^{i(\epsilon_b - \epsilon_a + \omega + i\eta)t'} \Big] \\
&= \sum_{a,b} f_a \left[\frac{X_{ab} Y_{ba}}{\epsilon_a - \epsilon_b + \omega + i\eta} + \frac{Y_{ab} X_{ba}}{\epsilon_a - \epsilon_b - \omega - i\eta} \right] \\
&= \sum_{a,b} \frac{f_a - f_b}{\epsilon_a - \epsilon_b + \omega + i\eta} X_{ab} Y_{ba},
\end{aligned} \tag{2.40}$$

where $f_{a,b}$ is the partition function for the states a and b, respectively, and η is an infinitesimal positive factor. We focus on the special case that the electron density

responses to the external electric field. The corresponding result can be directly used in the study of optical response. Both X and Y now are the electron density $n(r)$, and the external field is $F_0 = eV_0$. Based on Eq. (2.39), we have

$$\delta n(r,\omega,t) = \int dr' \chi_{nn}(r,r',\omega) e V_0(r',\omega) e^{-i\omega t}. \tag{2.41}$$

The absorption rate is then calculated as,

$$\begin{aligned} \bar{P}(\omega) &= Re\left[\frac{1}{2\pi}\int_0^{2\pi} dt \int dr e V_0^*(r,\omega) e^{i\omega t} \delta\dot{n}(r,\omega)\right] \\ &= \omega e^2 \int dr dr' V_0^*(r,\omega) Im\chi_{nn}(r,r',\omega) V_0(r',\omega). \end{aligned} \tag{2.42}$$

From Eq. (2.40), we can derive

$$Im\chi_{nn}(r,r',\omega) = \sum_{a,b} \pi\delta(\epsilon_a - \epsilon_b + \omega)(f_a - f_b) \langle a|n(r')|b\rangle \langle b|n(r)|a\rangle. \tag{2.43}$$

In the zero temperature limit, the above equation can be written as

$$Im\chi_{nn}(r,r',\omega) = \sum_{eh} \pi\delta(\epsilon_0 - \epsilon_{eh} + \omega) \langle 0|n(r')|eh\rangle \langle eh|n(r)|0\rangle, \tag{2.44}$$

where $|0\rangle$ and $|eh\rangle$, respectively, refer to the many-body ground state and the possible excited states, which correspond to possible transitions from a hole state $|a\rangle$ ($f_a = 1$) to an electron state $|b\rangle$ ($f_b = 0$).

2.3.3 Energy-weighted sum rule

Following the absorption result for certain ω, we show a simple sum rule by considering an external pulse

$$V_0(r)\delta(t) = \frac{1}{2\pi}\int_{-\infty}^{\infty} d\omega V(\omega) = \frac{V_0(r)}{2\pi}\int_{-\infty}^{\infty} d\omega e^{-i\omega t}. \tag{2.45}$$

Based on Eq. (2.42), the total absorption is

$$S = \frac{1}{2\pi}\int_{-\infty}^{\infty} d\omega \bar{P}(\omega) = \frac{1}{\pi}\int_{0}^{\infty} d\omega \bar{P}(\omega). \tag{2.46}$$

On the other hand, this external field essentially gives the equilibrium system an instant momentum $n(r)e\nabla V_0(r)$ at the time $t = 0$, and the energy gain can be calculated from

$$S = \int dr \frac{n(r)e^2|\nabla V_0(r)|^2}{2m_e}. \tag{2.47}$$

Comparing Eq. (2.46) and (2.47), we obtain the energy weight sum rule, which can be used to check the numerical results.

In addition, when we insert Eq. (2.42) and (2.44) into Eq. (2.46), we can reproduce the absorption strength Eq. (2.18) shown at the beginning of this section.

2.3.4 Random phase approximation

By now, we have seen how to obtain the absorption of systems for certain external fields. Essentially, as long as we have wavefunctions of ground state and excited states, the response functions can be evaluated from Eq. (2.40). However, for a many-body system, it is hard to get the wavefunctions of excited states. Although DFT offers a way to calculate the electron density of the ground state and the corresponding independent Kohn-Sham electronic states, we cannot obtain excited states by simply moving an electron from an occupied state to an unoccupied state. The reason is that the effective potential evaluated from ground state density will be changed due to the excitation, and then the original Kohn-Sham states cannot be used as the proper eigenstates of the new Hamiltonian, which should be composed by the ground state Hamiltonian and the additional effective potential due to the excitation.

Another way to understand the above argument is that the external field will induce the electron density change in the system, and conversely the density change will induce additional field acting back to the system. Again, we consider the response

of system to an external electric field V_{ext}, then the induced charge density is

$$\delta n(r,\omega) = \int dr' \chi^0(r,r',\omega) \left[V_{ext}(r',\omega) + V_{ind}(r',\omega) \right], \tag{2.48}$$

where χ^0 is the non-interacting density-density response function constructed from the Kohn-Sham state as

$$\begin{aligned} \chi^0(r,r',\omega) &= \sum_{a,b} \frac{f_a - f_b}{\omega^+ - (E_b - E_a)} \Psi_a^*(r)\Psi_b(r)\Psi_a(r')\Psi_b^*(r') \\ &= \sum_{a,b} f_a \left[\frac{\hat{\Psi}_{a,b}(r,r')}{\omega^+ - (E_b - E_a)} + \frac{\hat{\Psi}_{a,b}^*(r,r')}{-\omega^+ - (E_b - E_a)} \right], \end{aligned} \tag{2.49}$$

where E_i, Ψ_i and f_i are energy, wavefunction and occupation number of states $i = a, b$, respectively, $\omega^+ = \omega + i\eta$ is the energy of the excitation ω plus an infinitesimal imaginary part iη, and $\hat{\Psi}_{a,b}(r,r') = \Psi_a^*(r)\Psi_b(r)\Psi_a(r')\Psi_b^*(r')$ is for simplicity. The relation between the induced change density δn and the corresponding induced potential is

$$V_{ind}(r) = \int dr' K(r,r')\delta n(r'), \tag{2.50}$$

where and hereafter we ignore the argument ω in all functions for convenience. In the random phase approximation (RPA), $K(r,r')$ usually called residue interaction is the bare coulomb interaction. Combining Eq. (2.48) and (2.50), we have

$$\delta n = \chi^0 \left[V_{ext} + K\delta n \right], \tag{2.51}$$

where, for simplicity, we ignore the integrals by just considering them as matrix multiplications. We then can define the interacting density-density response function χ through

$$\delta n = \chi V_{ext} = \frac{\chi^0}{1 - \chi^0 K} V_{ext}. \tag{2.52}$$

Comparing this result with Dyson equation Eq. (2.17), we can see that the residue interaction K can be viewed as perturbation to the system described by χ^0.

Essentially, χ^0 is a two-body Green's function, which corresponds to a Hamiltonian of electron-hole pairs.

2.4 Recursive Green's Function Method

In this section, we introduce the concept of the recursive Green's function Method [31], which is an effective method to study the transport properties of mesoscopic systems.

We consider a simple mesoscopic system composed of the left lead side (L), the right lead side (R) and the middle conductive region (N). We slice the whole system into a series of principal layers, which only interact with nearest-neighbor. Then, the tight-binding Hamiltonian can be written as a block tridiagonal matrix,

$$H = \begin{pmatrix} H_L & H_{LN} & 0 \\ H_{LN}^\dagger & H_N & H_{NR} \\ 0 & H_{NR}^\dagger & H_R \end{pmatrix}, \tag{2.53}$$

where $H_L(H_R)$ is infinite size square matrix describing the semi-infinite left (right) lead side. Suppose there are m principle layers in N region, then H_N is a finite matrix with the size $mN_0 \times mN_0$, and N_0 is the number of atoms in one principle layer. All the other off-diagonal blocks describe the coupling between lead sides and N region. Now, suppose the Green's function of the system is

$$G = \begin{pmatrix} G_L & G_{LN} & G_{LR} \\ G_{NL} & G_N & G_{NR} \\ G_{RL} & G_{RN} & G_R \end{pmatrix}. \tag{2.54}$$

It is easy to get an equation for the element G_N of the complete Green's function G as

$$(E - H_N - H_{LN}^\dagger G_L^0 H_{LN} - H_{NR} G_R^0 H_{NR}^\dagger) G_N = I, \tag{2.55}$$

where $G^0_{L,R} = (E - H_{L,R})^{-1}$ is an isolate Green's function for left (right) lead side, which only describes the isolated lead side assumed to be decoupled with N region. Now one needs to find the inverse of an infinite large matrix and then the inverse of an mN_0 by mN_0 matrix, sometimes this matrix could be very large. To solve these difficulties, a so-called *surface* Green's function g is used. Here we use the surface Green's function $g^r_{x,x}$ to describe the xth layer block of the isolate Green's function when the interactions between $(x-1)$th and xth layers is set to be zero. Now since the interactions only exist between the nearest layers, we have

$$g^r_{i,i} = [E - H_{i,i} - H_1\, g^r_{i+1,i+1}\, H_1^\dagger]^{-1} \tag{2.56}$$

and

$$G_{1,1} = [E - H_{1,1} - H_1 g^r_{2,2} H_1^\dagger - H_1^\dagger g^l_R H_1], \tag{2.57}$$

where H_1 describes the interlayer coupling and $H_{i,i}$ is the intralayer Hamiltonian. $G_{1,1}$ is the first layer block of the Green's function G_N. So, as long as we have surface Green's function g^l_L and g^r_R for the left and right lead side, $G_{1,1}$ can be calculated through Eq. (2.56) and (2.57). To get g^l_L and g^r_R, we can still use Eq. (2.56) to calculate a long enough lead region to approach the semi-infinite results. However, since $H_{i,i}$ is a constant matrix in the lead region, a more efficient algorithm [32] can be used to evaluate surface Green's function for a 2^N-layer lead with only N recursive steps. With $G_{1,1}$, we can calculate the transmission rate as

$$T = Tr[\Gamma^L_{1,1}(A_{1,1} - G_{1,1}\Gamma^L_{1,1}G^\dagger_{1,1})], \tag{2.58}$$

where $\Gamma^L_{1,1} = -2\, Im(H_1^\dagger g^l_L H_1)$ and $A_{1,1} = -2Im(G_{1,1})$. In the end, for ballistic transport, the conductance is obtained by the Landauer formula [cite]

$$C = \frac{2e^2}{h} T. \tag{2.59}$$

Chapter 3

Plasmons in Metal Nanostructures

3.1 Introduction

A surface plasmon describes the collective excitation of the conduction electrons at a metal surface [33]. Recently, a rapidly expanding field [34, 35] is to exploit novel aspects of surface plasmons defined at the surfaces or interfaces of elegantly fabricated metal nanostructures to trap light with wavelengths much larger than the nanoscale for a wide range of applications. This development stems from the fact that the properties of surface plasmons sensitively depend on the size, shape, and dielectric environment of the metal nanostructures, rendering plasmonics immense application potentials in surface-enhanced spectroscopies [18, 19], biological and chemical sensing [36, 37], nanolithography [38, 39], solar cells [20], etc.. Traditionally, the surface plasmon is described within the classical picture, where the optical response of a system is obtained by solving electromagnetic Maxwell equations with bulk dielectric properties of the constituent materials. However, as the characteristic lengths of the plasmonic materials become smaller and smaller, intriguing phenomena may emerge beyond the expectations of classical picture [40, 41], demanding more accurate quantum mechanical treatments [42, 43].

To date, studies of surface plasmons have been predominately focused on their frequency tunability [44, 45]. In contrast, much less effort has been devoted to the plasmon lifetime[46], an equally important aspect of the surface plasmon. For practically every plasmonics application, it is highly desirable to have as long a lifetime as possible once the surface plasmons are excited. Competing lifetime broadening mechanisms considered previously include inhomogeneous broadening [47, 48], boundary scattering, radiation damping, and Landau damping. For example, for spherical particles with radius L, boundary scattering has been found within a semiclassical picture to result in a $\propto 1/L$ correction to the linewidth of surface plasmons [49]. As the fabrication techniques continue to improve and the system sizes continue to shrink into the quantum regime, both inhomogeneous broadening and radiation damping can be greatly suppressed, making Landau damping the dominant lifetime broadening mechanism. In this regime, the boundaries of the system are actually parts of the physical conditions defining the confined electron energy levels that contribute to Landau damping, via plasmon-electron interactions[50]. This dominant intrinsic damping channel is expected to exhibit significant tunability, because the quantized electronic states depend sensitively on the size and shape of the metal nanostructures.

In this chapter, we start with the classical studies in section 4.2 to present some basic concepts of plasmons. To gain a feeling about the microscopic description of plasmons, we introduce the hydrodynamic hybridization model [cite] in section 4.3. The detailed quantum mechanical procedures are presented in section 4.4. In section 4.5, using the quantum methods, we present the results of the energy and the linewidth of surface plasmon in metal nanostructures.

3.2 Classical Electromagnetic Studies

Using Eq. (2.19) and (2.25), many optical phenomena can be quantitatively understood. First, clearly, for different frequencies of light, materials will have different

responses due to the ω dependence. Then notice the role of ω_0, which essentially distinguishes between insulators and metals. For an insulator, due to the electronic energy gap at the Fermi surface, electrons are bounded with a large ω_0. For $\omega \ll \omega_0$, we expect $\epsilon > 1$ and the absorption $\bar{P} \propto \omega^2/\omega_0^2$ is small. This is the reason that an insulator is usually transparent.

On the other hand, for a metal, we can consider a free electron gas model, which means $\omega_0 = 0$. Then we arrive at the Drude model

$$\epsilon(\omega) = 1 + \chi(\omega) = 1 - \frac{\omega_p^2}{\omega^2 + i\gamma\omega}. \tag{3.1}$$

For a small γ, when $\omega \ll \omega_p$, $\epsilon < 0$ and the absorption $\bar{P} \propto \omega_p^2/\omega^2$ is very large. Thus a metal prefers to strongly absorb light at low frequencies and becomes transparent at high frequencies.

After getting the microscopic response packed into the dielectric function ϵ, many optical properties of material can be studied using the macroscopic Maxwell's equations. Now, at a metal-dielectric interface, we use these equations to derive the so called *surface plasmon polariton* (SPP), which is the quasiparticle resulting from the coupling between light and the surface plasmon.

Considering that the whole space is filled by the nonmagnetic materials with local dielectric functions $\epsilon_1(\omega)$ (metal) in the space $z < 0$ and ϵ_2 (dielectric) in the space $z > 0$, our purpose is to derive the condition for the existence of an electromagnetic wave propagating along the interface $z = 0$. The electric field $\mathbf{E_i}$ and magnetic field $\mathbf{H_i}$ in both sides can be described by the Maxwell's equations

$$\nabla \cdot \epsilon_i \mathbf{E_i} = 0, \tag{3.2}$$

$$\nabla \cdot \mathbf{H_i} = 0, \tag{3.3}$$

$$\nabla \times \mathbf{E_i} = -\partial_t \mathbf{H_i}, \tag{3.4}$$

and

$$\nabla \times \mathbf{H_i} = \epsilon \partial_t \mathbf{E_i}. \tag{3.5}$$

Using Eq. (3.4) and (3.5), we get the wavefunction of $\mathbf{E_i}$ as

$$\nabla \times (\nabla \times \mathbf{E_i}) = \nabla(\nabla \cdot \mathbf{E_i}) - \nabla^2 \mathbf{E_i} = -\epsilon \partial_t^2 \mathbf{E_i}. \tag{3.6}$$

Supposing the EM wave propagates in (x, z) plane, we obtain the relation

$$k_x^2 + k_{iz}^2 = \epsilon_i \omega^2. \tag{3.7}$$

Also, due to the symmetry in y direction $E_{iy} = 0$, and then H_{ix} and H_{iz} equal to zero too. From Eq. (3.5), we get an additional equation

$$-k_{iz} H_{iy} = \epsilon_i \omega E_{ix}. \tag{3.8}$$

At the interface, the continuity of E_{ix} and H_{iy} then imply

$$\frac{k_{1z}}{\epsilon_1} = \frac{k_{2z}}{\epsilon_2}. \tag{3.9}$$

Using Eq. (3.7) and (3.7), we obtain the SPP dispersion

$$k_x = \omega \sqrt{\frac{\epsilon_1 \epsilon_2}{\epsilon_1 + \epsilon_2}}. \tag{3.10}$$

For a large k_x, we require the $\epsilon_1 + \epsilon_2 = 0$. Then if we consider $\epsilon_1(\omega)$ described by Drude model and $\epsilon_2 = 1$, we can solve the surface plasmon frequency as

$$\omega_{sp} = \frac{\omega_p}{\sqrt{2}}. \tag{3.11}$$

Here, we derive this result based on a pure classical method. Later, with more accurate quantum calculation we are going to reproduce this value.

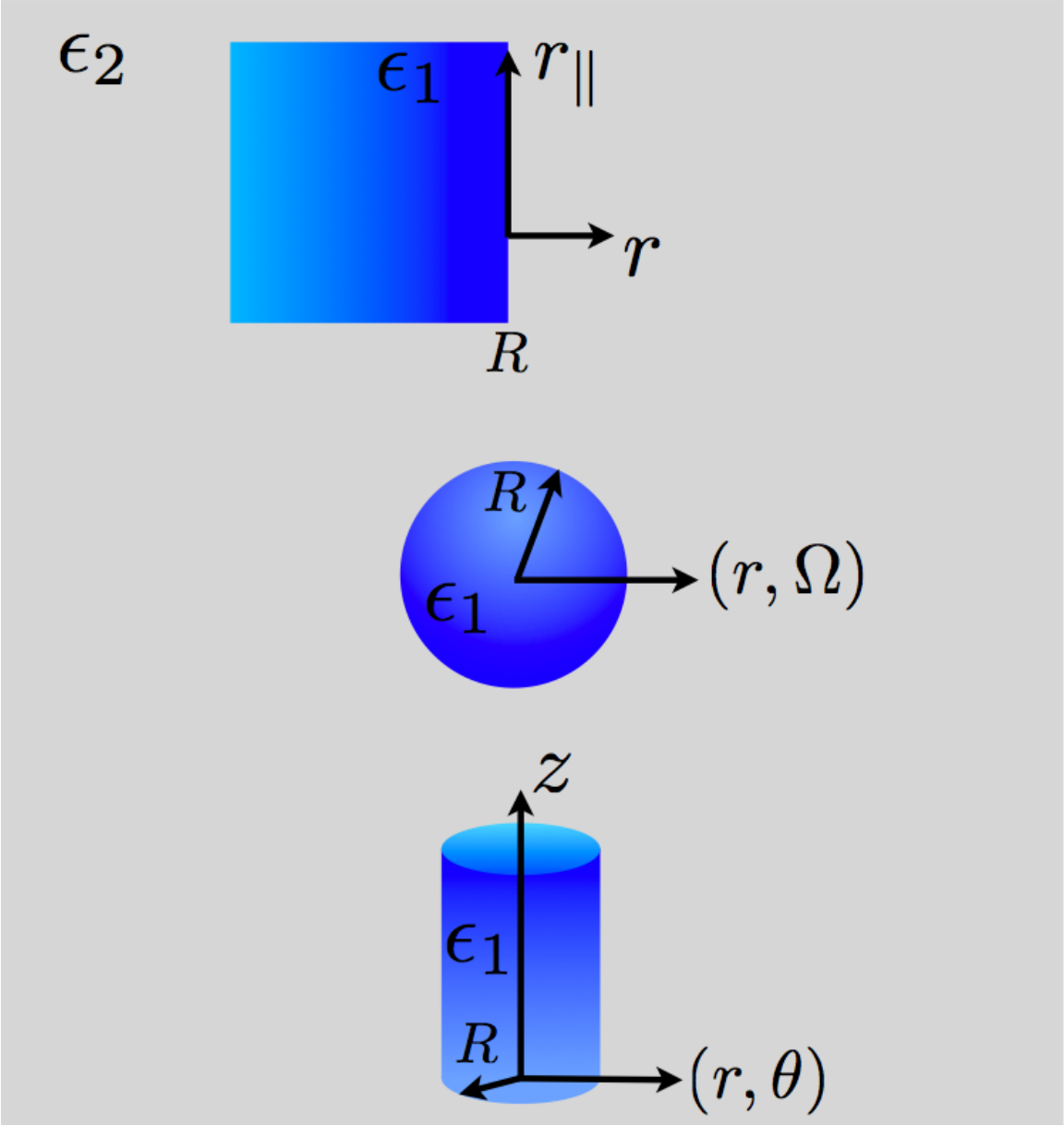

Figure 3.1: Three different interfaces and their corresponding coordinate systems. Each interface separates the two materials with different dielectric constants, ϵ_1 and ϵ_2.

Actually, the surface plasmon frequency can be more easily calculated by solving the electrostatic Laplace equation $\nabla^2\phi = 0$ with certain boundary condition, as long as the charge fluctuation or the size of the system is much smaller than the external driving field, which refers to the quasi-static approximation. As shown in Fig. 3.1, we consider three different interface geometries, i.e. sphere (S), cylinder (C) and plane (P), each of which separates two regions with the dielectric functions $\epsilon_1(\omega)$ (metal) and ϵ_2, respectively. Suppose that the charge oscillation exists only at the interface, then the potential can be solved in two regions as

$$\phi_s(r,\Omega) = \sum_{l,m} \left[A_{l,m} r^l + B_{l,m} r^{-(l+1)}\right] Y_{l,m}(\Omega), \tag{3.12}$$

$$\phi_c(r,\theta,z) = \sum_{k,m} \left[A_{k,m} I_m(kr) + B_{k,m} K_m(kr)\right] e^{ikz} e^{im\theta}, \tag{3.13}$$

$$\phi_p(r,r_\parallel) = \sum_k \left[A_k e^{kr} + B_k e^{-kr}\right] e^{ikx} = \sum_k \left[A_k e^{kr} + B_k e^{-kr}\right] e^{ikx}. \tag{3.14}$$

Due to the boundary condition $\phi(\infty) = 0$, we have $A = 0$ in region 2. Due to $\phi(-\infty) = 0$ for plane and $\phi(0) = 0$ for sphere and cylinder, we have $B = 0$ in region 1. Then considering the boundary condition at the interface

$$\phi_1(R) = \phi_2(R), \tag{3.15}$$

$$\epsilon_1 \left.\frac{\partial\phi_1}{\partial r}\right|_{r=R} = \epsilon_2 \left.\frac{\partial\phi_2}{\partial r}\right|_{r=R}, \tag{3.16}$$

we can solve the relation of dielectric functions as

$$\epsilon_1 = -\frac{l+1}{l}\epsilon_2, \tag{3.17}$$

$$\epsilon_1 = -\frac{I_m(kR)K_{m-1}(kR)}{I_{m-1}(kR)K_m(kR)}\epsilon_2, \tag{3.18}$$

$$\epsilon_1 = -\epsilon_2, \tag{3.19}$$

for sphere, cylinder and planar respectively. When the frequency satisfies those conditions, the charges at the interface can strongly oscillate with the corresponding eigenmodes, resulting in the surface plasmon modes. For example, when $\omega = \omega_p/\sqrt{3}$, the spherical dipole ($l = 1$) mode can strongly absorb the energy from the external field. Also as aforementioned, the frequency $\omega = \omega_p/\sqrt{2}$ corresponds to the eigenmode in the planar case.

By now, we have seen some simple examples showing the way to solve the plasmon mode with classical electromagnetic theory. With modern powerful computational tools, we can also directly calculate the dynamic response of materials by evaluating the evolution of spatially discretized electric and magnetic fields in small time intervals, which is the spirit of the finite-difference time-domain method (FDTD). However, we should notice that the classical calculation depends on the dielectric function, which is approximated with the Drude model. The actual dielectric function can, of course, be determined from experiments. But as we have shown in the Lorentz model, this function should depend on the detailed electronic structure of system, therefore, the computation becomes very complicated for nanostructures, where nonlocal effect and discretization of the electronic levels are expected to have significant effects.

3.3 Hydrodynamic Hybridization Model

In this section, we go one more step to introduce a hydrodynamic model. In this model, we do not consider the dielectric function, and instead of focusing on the response field, we turn our attention to a microscopic quantity, the surface charge density. The advantage of this model is that we can clearly understand the plasmon mode from microscopic point of view, and therefore elucidate the contribution from the interaction among different plasmon modes.

The plasmon is defined as an incompressible irrotational deformation of the conduction electron gas, which can be described by two equations,

$$\partial_t n + \nabla \cdot \mathbf{J} = 0 \tag{3.20}$$

and

$$\nabla \times \mathbf{J} = 0. \tag{3.21}$$

The irrotational property of $\mathbf{J}$ implies the existence of a scalar field η with the definition $\mathbf{J} = n_0 \nabla \eta$, which should also satisfy the Laplace equation $\nabla^2 n = 0$. Since we consider an incompressible electron gas, the density fluctuation only exist at the boundary. Suppose this deformation is very small, we can ignore its effect in the normal direction of the surface, and then define a surface charge density σ, which satisfies the equation

$$\sigma dS = (n - n_0) dV. \tag{3.22}$$

We then have

$$\partial_t \sigma dS = \partial_t n dV = -\nabla \cdot \mathbf{J} dV = -\mathbf{J} \cdot \hat{\mathbf{n}} dS = n_0 \nabla \eta dS. \tag{3.23}$$

Now we essentially build up a relation between the surface charge density and their velocity. Then the kinetic energy and electronic potential can be readily calculated as

$$T = \frac{1}{2} \int n_0 (\nabla \eta)^2 dV = \frac{1}{2} \int n_0 \nabla \cdot (\eta \nabla \eta) dV = \frac{1}{2} \int n_0 \eta \nabla \eta \cdot \hat{\mathbf{n}} dS \tag{3.24}$$

and

$$V = \frac{1}{2} \int \frac{(n(\mathbf{r}) - n_0)(n(\mathbf{r}') - n_0)}{|\mathbf{r} - \mathbf{r}'|} d\mathbf{r} d\mathbf{r}' = \frac{1}{2} \int \frac{\sigma(S)\sigma(S')}{|\mathbf{r} - \mathbf{r}'|} dS dS'. \tag{3.25}$$

Now, we choose the planar system shown in Fig. 3.1(a) as an example. Since $\nabla^2\eta = 0$, similar to the classical electric potential, we can expend η as

$$\eta(r, r_\parallel, t) = \sum_k \dot{C}_k(t)\sqrt{\frac{1}{k}}e^{-kR}e^{kr}e^{ikr_\parallel}, \tag{3.26}$$

and then we have

$$\sigma(r_\parallel, t) = n_0 \sum_k C_k(t)\sqrt{k}e^{ikr_\parallel}. \tag{3.27}$$

Then the kinetic energy and electrostatic potential can be expressed as the functions of $\dot{C}_k$ and C_k respectively,

$$T = \frac{1}{2}n_0 Re\left[\int dS\eta^*(R, r_\parallel, t)\nabla_r\eta(R, r_\parallel, t)\right] = \frac{1}{2}n_0\sum_k \dot{C}_k^2(t)\frac{S}{2} \tag{3.28}$$

and

$$\begin{aligned} V &= \frac{1}{2}Re\left[\int \sigma^*(r_\parallel, t)\sigma(r'_\parallel, t)\frac{2\pi}{k}e^{ik(r_\parallel - r'_\parallel)}dSdS'\right] \\ &= \pi n_0^2 \sum_{kk'}\int dSdS'C_k^2(t)\frac{1}{2}Re\left(e^{-ikr_\parallel}e^{ikr'_\parallel}e^{ik'(r_\parallel - r'_\parallel)}\right) = \frac{1}{2}n_0\frac{\omega_p^2}{2}\sum_k C_k^2(t)\frac{S}{2}, \end{aligned} \tag{3.29}$$

where coulomb interaction has been transformed into k-space in $r_\parallel$ direction. The Lagrange of the system is

$$L = T - V = \frac{n_0 S}{4}\sum_k\left[\dot{C}_k^2(t) - \frac{\omega_p^2}{2}C_k^2(t)\right]. \tag{3.30}$$

We finally get the oscilltary frequency of the system as

$$\omega = \frac{\omega_p}{\sqrt{2}}. \tag{3.31}$$

This is a semiclassical result, where the interactions among the electrons are considered. Now we can further derive the plasmon modes in a thin film structure by simply involving the coulomb interactions between two surfaces.

For a thin film with two surfaces at $r = a$ and b, the scalar potential η includes the contributions from both sides as

$$\eta(r, r_\parallel, t) = \sum_k \left(\dot{C}_k \sqrt{\frac{1}{k}} e^{-kb} e^{kr} e^{ikr_\parallel} + \dot{S}_k \sqrt{\frac{1}{k}} e^{ka} e^{-kr} e^{ikr_\parallel} \right). \tag{3.32}$$

The induced charge at a and b surfaces are thus written respectively as

$$\sigma_a(r_\parallel, t) = n_0 \sum_k \left(C_k \sqrt{k} e^{k(a-b)} e^{ikr_\parallel} - S_k \sqrt{k} e^{ikr_\parallel} \right) \tag{3.33}$$

and

$$\sigma_b(r_\parallel, t) = n_0 \sum_k \left(C_k \sqrt{k} e^{ikr_\parallel} - S_k \sqrt{k} e^{k(a-b)} e^{ikr_\parallel} \right). \tag{3.34}$$

Combining the kinetic energy

$$T = \frac{n_0 S}{4} \left(1 - e^{2k(a-b)}\right) \left(\dot{C}_k^2 + \dot{S}_k^2 \right) \tag{3.35}$$

and coulomb potential

$$V = \frac{n_0 S}{4} \frac{\omega_p^2}{2} \left[C_k^2 + S_k^2 - 2 C_k S_k e^{k(a-b)} \right] \left[1 - e^{2k(a-b)} \right], \tag{3.36}$$

We obtain the Lagrangian

$$L = \begin{pmatrix} C_k & S_k \end{pmatrix} \left[\omega^2 \begin{pmatrix} 1 & 0 \\ 0 & 1 \end{pmatrix} - \frac{\omega_p^2}{2} \begin{pmatrix} 1 & e^{k(a-b)} \\ e^{k(a-b)} & 1 \end{pmatrix} \right] \begin{pmatrix} C_k \\ S_k \end{pmatrix}, \tag{3.37}$$

where the hybridized oscillation frequency ω can be readily solved as

$$\omega = \omega_{ps} (1 \pm e^{2k(a-b)})^{\frac{1}{2}} = \frac{\omega_p}{\sqrt{2}} (1 \pm e^{2k(a-b)})^{\frac{1}{2}}. \tag{3.38}$$

This is a result we will use to compare with our quantum calculations. The hydrodynamic model can qualitatively explain the energy dispersions of plasmons in

many low-dimensional structures. The interactions among different plasmon modes are explicitly shown in the coulomb potential part, and therefore the underlying physics is very clear. However one cannot catch any linewidth information with this semiclassical model, since the dissipative mechanism does not exist in this mode.

3.4 Quantum Mechanical Studies

To catch the quantum size effect and linewidth information of plasmons, we show the quantum mechanical approach and detailed formalism for several prototype systems in this section.

3.4.1 Ground states

We first carry out the ground state calculation in three prototype systems, including zero-dimension($0D$) nanoshells, $1D$ coaxial nanotubes, and $2D$ thin films shown in Fig. 3.2. The 'nD' symbol assigned to them is based on different translational symmetries. Jellium mode is used to describe the ion background, which is then approximated by the following distribution of positive charges

$$n_b(r) = n_0[\Theta(r - r_1) - \Theta(r - r_2)], \tag{3.39}$$

where $\Theta(r)$ is the Heavyside step function, n_0 is the average electron density depending on Wigner-Seitz radius r_s of different materials as

$$n_0 = \frac{3}{4\pi r_s^3}, \tag{3.40}$$

and $r_{1,2}$ indicates the positions of two boundaries in the direction r perpendicular to the surfaces. Also we have $0 < r_1 < r_2$ (for $2D$ we do not have to involve 0, but it is more convenient to use this consistent relation.). Within jellium mode we have the exact translational or/and rotational symmetries in our prototype systems. The

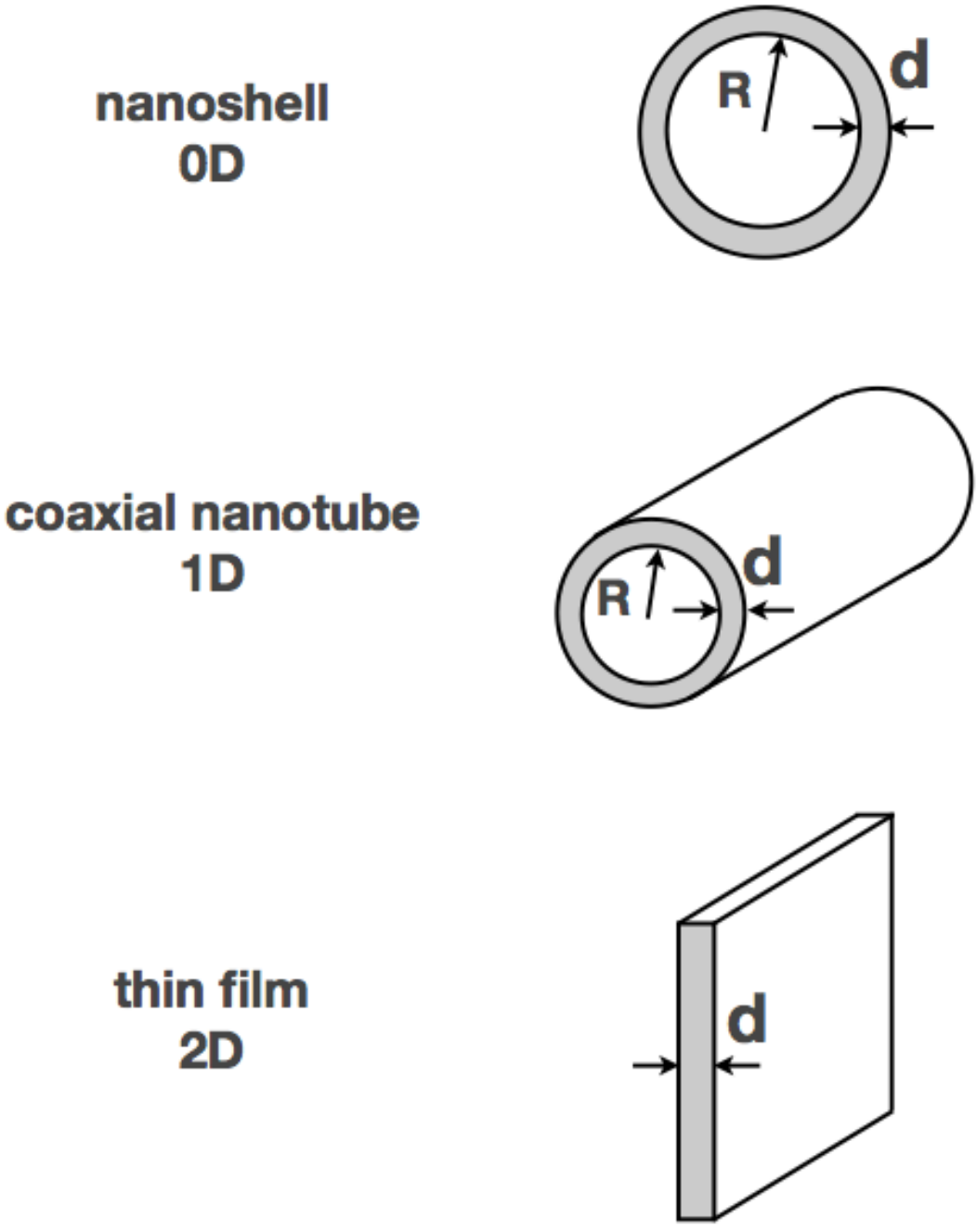

Figure 3.2: Schematic of the three prototype low-dimensional systems.

wavefunctions in three different systems can then be written as

$$\begin{cases} \psi_{0D}(\mathbf{r}) = \psi_{0D}(r,\Omega) = \phi_{n,l}(r)Y_{l,m}(\Omega) \\ \psi_{1D}(\mathbf{r}) = \psi_{1D}(r,\theta,z) = \dfrac{1}{\sqrt{L}}\phi_{n,l}(r)e^{il\theta}e^{ikz} \\ \psi_{2D}(\mathbf{r}) = \psi_{2D}(r,r_\perp) = \dfrac{1}{L}\phi_n(r)e^{ik_\perp \cdot r_\perp} \end{cases}. \tag{3.41}$$

Where, $Y_{l,m}(\Omega)$ is the spherical harmonics function, satisfying $\int d\Omega |Y_{l,m}(\Omega)|^2 = 4\pi$, n is the quantum number in the r direction, l is the angular momentum, m is the magnetic quantum number, and k is the momentum in the direction with translational symmetry.

In all of our nD systems, the KS equation can be reduced to a one-dimensional equation as

$$H_{KS}u(r) = \left(-\frac{1}{2}\frac{d^2}{dr^2} + V_{eff}[n(r)]\right)u(r) = Eu(r). \tag{3.42}$$

To obtain $\phi(r)$ in the confined direction, we solve the Kohn-Sham equation as

$$\left(-\frac{1}{2}\frac{d^2}{dr^2} + V_{eff}[n(r)]\right)u(r) = Eu(r), \tag{3.43}$$

where $u(r)$ is the modified radial wavefunction, which has different forms corresponding to different structures as

$$\begin{cases} u_{0D}(r) = \sqrt{4\pi r^2}\phi(r) \\ u_{1D}(r) = \sqrt{2\pi r}\phi(r) \\ u_{2D}(r) = \phi(r) \end{cases}, \tag{3.44}$$

and $u(r)$ satisfies the normalization relation $\int dr|u(r)|^2 = 1$. Due to reduction of dimensions in KS equation, the additional centrifugal potential $V_{geo}(r)$ is introduced into effective potential

$$V_{eff}[n(r)] = V_{geo}(r) + V_H[n(r)] + V_{xc}[n(r)], \tag{3.45}$$

where

$$\begin{cases} V_{geo,0D}(r) = \dfrac{l(l+1)}{2r^2} \\ V_{geo,1D}(r) = \dfrac{(l+\frac{1}{2})(l-\frac{1}{2})}{2r^2} \\ V_{geo,2D}(r) = 0 \end{cases} . \tag{3.46}$$

The Hartree potential V_H are

$$\begin{cases} V_{H,0D}[n(r)] = 4\pi \int dr' \left[r'^2 \rho(r')\right] \dfrac{1}{r_>} \\ V_{H,1D}[n(r)] = -4\pi \int dr' \left[r' \rho(r')\right] \ln r_> \\ V_{H,2D}[n(r)] = -4\pi \int dr' \left[\rho(r')\right] r_> \end{cases} , \tag{3.47}$$

where $r_> = \max(r, r')$, and $\rho(r) = n(r) - n_b(r)$ is the charge density, including contributions from both ions and electrons. For the exchange-correlation potential $V_{xc} = V_x + V_c$, we use the local density approximation with the exchange potential approximated by V_x and the Perdew-Zunger correlation V_c. More details are presented in Appendix C.

The next step is to calculate the electron density based on the wavefunction solved from KS equation, which is calculated by summing up the contribution from all electron states under the Fermi energy (we consider zero temperature) as

$$\begin{aligned} n(r) &= \sum_{E_\phi < E_F} D_s D_l D_k |\phi(r)|^2 \\ &= \sum_{E_\phi < E_F} \begin{cases} 2\,(2l+1)\,|\phi_{n,l}(r)|^2 & \text{0D} \\ 2\,(2-\delta_{l,0})\,\dfrac{2k_0}{2\pi}\,|\phi_{n,l}(r)|^2 & \text{1D} \\ 2\,\dfrac{\pi k_0^2}{(2\pi)^2}\,|\phi_{n,l}(r)|^2 & \text{2D} \end{cases} , \end{aligned} \tag{3.48}$$

where, $D_s = 2$ is the spin degeneracy, D_l is the magnetic degeneracy, D_k is the contribution of electrons with different k but same $\phi(r)$, and $k_0 = \sqrt{2(E_F - E_\phi)}$ is the maximum of momentum in the extend direction for a certain E_ϕ. Finally, the

ground state density can be self-consistently calculated by the closed loop through Eq. (3.43) and Eq. (3.48). We are then ready to start the calculation for the excited states.

3.4.2 Excited states and plasmon resonances

Due to the existing rotational and translational symmetries in our systems, the excitation of plasmon modes should satisfy the energy conservation and also the (angular) momentum conservation. We then expand all related quantities in our systems based on corresponding conserved quantum numbers. For Coulomb interactions, we have

$$\begin{cases} K(\mathbf{r}_1,\mathbf{r}_2) = \sum_{l,m} Y_{lm}(\Omega_1) Y^*_{lm}(\Omega_2) \frac{r^l_<}{r^{l+1}_>} \frac{4\pi}{2l+1} \\ K(\mathbf{r}_1,\mathbf{r}_2) = \frac{1}{2\pi} \sum_m \frac{1}{L} \sum_{k_z} e^{im(\theta_1-\theta_2)} e^{ik_z(z_1-z_2)} 4\pi I_m(k_z r_<) K_m(k_z r_>) \\ K(\mathbf{r}_1,\mathbf{r}_2) = \frac{1}{A} \sum_{k_\parallel} \frac{2\pi}{k_\parallel} e^{k_\parallel (r_< - r_>)} e^{i\mathbf{k}_\parallel \cdot (r_{1,\parallel} - r_{2,\parallel})} \end{cases} . \tag{3.49}$$

The reduced response functions are defined as

$$\begin{cases} \chi^0_{0D}(r,r';L) = \int d\Omega d\Omega' Y^*_{L,m}(\Omega) Y_{L,m}(\Omega') \chi^0_{0D}(\mathbf{r},\mathbf{r}') \\ \chi^0_{1D}(r,r';L,q) = \int dz dz' d\theta d\theta' e^{q(z-z')} e^{l(\theta-\theta')} \chi^0_{1D}(\mathbf{r},\mathbf{r}') \\ \chi^0_{2D}(r_1,r_2;q_\perp) = \int dr_\perp dr'_\perp e^{q_\perp (r_\perp - r'_\perp)} \chi^0_{2D}(\mathbf{r},\mathbf{r}') \end{cases} . \tag{3.50}$$

Their explicit forms are listed as follows:

$$\begin{aligned} \chi^0_{0D}(r,r';L) = \sum_{a,b} f_a \frac{(2l_a+1)(2l_b+1)}{4\pi} \begin{pmatrix} L & l_a & l_b \\ 0 & 0 & 0 \end{pmatrix}^2 \\ \left[\frac{1}{\omega^+ - (\epsilon_b - \epsilon_a)} + \frac{1}{-\omega^+ - (\epsilon_b - \epsilon_a)} \right] \Phi_{a,b}(r,r'), \end{aligned} \tag{3.51}$$

$$\chi^0_{1D}(r,r';L,q) = \sum_{a,b} f_a \Bigg[\frac{\delta(|l_a \pm L| - l_b)}{\omega^+ - (\epsilon_b - \epsilon_a) - (\frac{1}{2}q^2 - k_a q)} + \frac{\delta(|l_a \pm L| - l_b)}{-\omega^+ - (\epsilon_b - \epsilon_a) - (\frac{1}{2}q^2 + k_a q)} \Bigg] \Phi_{a,b}(r,r'), \tag{3.52}$$

$$\chi^0_{2D}(r,r';q_\parallel) = \sum_{a,b} f_a \Bigg[\frac{1}{\omega^+ - (\epsilon_b - \epsilon_a) - (\frac{1}{2}q_\parallel^2 - k_a \cdot q_\parallel)} + \frac{1}{-\omega^+ - (\epsilon_b - \epsilon_a) - (\frac{1}{2}q_\parallel^2 + k_a \cdot q_\parallel)} \Bigg] \Phi_{a,b}(r,r'), \tag{3.53}$$

where $\epsilon_{a,b}$ is the energy of states a, b in confined direction, $k_{a,b}$ is their momentum in extended direction, and $\Phi_{a,b}(r,r') = \phi_a(r)\phi_b(r)\phi_a(r')\phi_b(r')$.

To perform the summation of states a and b, a commonly used method is related to the Green's function. We know the relation

$$G(r,r',E) = \sum_b \frac{\phi_b(r)\phi_b(r')}{E - \epsilon_b}, \tag{3.54}$$

where the Green's function can be solved from

$$(H_{KS} - E)G = -\delta(r - r'). \tag{3.55}$$

Then we just need to do the finite-term summation $\sum_a f_a$ for χ^0. However, as the system size increases, the Hamiltonian matrix will become very large, making the inverse process become slow. More importantly, for the $1D$ and $2D$ systems, the summation $\sum_a f_a$ is actually an integration, an inevitable error will then be introduced by doing this integration numerically. So we can use the second method

to first integrate the momentum k in the formulas, which give

$$
\begin{aligned}
&\chi^0_{1D}(r,r',L,q) \\
&= \sum_{n,n'}\sum_{l,l'}\sum_{k,k'}(f_{n,m,k}-f_{n',m',k'})\frac{\delta(k-k'+q)\Phi_{n,n',l,l'}(r,r')}{\frac{1}{2}(k^2-k'^2)+(\epsilon_{n,l}-\epsilon_{n',l'})+\omega^+} \\
&= \sum_{n,n'}\sum_{l,l'=-\infty}^{\infty}(f_{n,l}-f_{n',l'})\frac{1}{2\pi}\int_{k_{min}}^{k_{max}}dk\frac{\delta(l-l'+L)\Phi_{n,n',l,l'}(r,r')}{(-kq-\frac{1}{2}q^2)+(\epsilon_{n,l}-\epsilon_{n',l'})+\omega^+} \\
&= \sum_{n,n'}\sum_{l,l'=0}^{\infty}(f_{n,l}-f_{n',l'})\frac{\delta(|l\pm L|-l')}{2\pi q} \\
&\ln\left[\frac{(-k_{min}q-\frac{1}{2}q^2)+(\epsilon_{n,l}-\epsilon_{n',l'})+\omega^+}{(-k_{max}q-\frac{1}{2}q^2)+(\epsilon_{n,l}-\epsilon_{n',l'})+\omega^+}\right]\Phi_{n,n',l,l'}(r,r')
\end{aligned}
\tag{3.56}
$$

and

$$
\begin{aligned}
&\chi^0_{2D}(r,r',q_\parallel) = -\frac{2\pi i}{(2\pi)^2}\sum_{n,n'}\int_0^\infty k_\parallel dk_\parallel f_{n,k_\parallel} \\
&\left[\frac{\Phi_{n,n'}(r,r')}{\sqrt{(k_\parallel K_\parallel)^2-(-\frac{1}{2}K_\parallel^2+\epsilon_{n,n'}+\omega^+)^2}}-\frac{\Phi_{n,n'}(r,r')}{\sqrt{(k_\parallel K_\parallel)^2-(-\frac{1}{2}K_\parallel^2+\epsilon_{n,n'}-\omega^+)^2}}\right] \\
&= -\frac{i}{2\pi}\sum_{n,n'}\int_0^{\sqrt{E_F-\epsilon_n}}2k_\parallel dk_\parallel \\
&\left[\frac{\Phi_{n,n'}(r,r')}{\sqrt{(k_\parallel K_\parallel)^2-(-\frac{1}{2}K_\parallel^2+\epsilon_{n,n'}+\omega^+)^2}}-\frac{\Phi_{n,n'}(r,r')}{\sqrt{(k_\parallel K_\parallel)^2-(-\frac{1}{2}K_\parallel^2+\epsilon_{n,n'}-\omega^+)^2}}\right] \\
&= -\frac{i}{\pi}\sum_{n,n'}\frac{\Phi_{n,n'}(r,r')}{K_\parallel^2}\left[\sqrt{2(E_F-\epsilon_n)K_\parallel^2-(-\frac{1}{2}K_\parallel^2+\epsilon_{n,n'}+\omega^+)^2}\right. \\
&-\sqrt{2(E_F-\epsilon_n)K_\parallel^2-(-\frac{1}{2}K_\parallel^2+\epsilon_{n,n'}-\omega^+)^2} \\
&\left.-\left(\sqrt{-(-\frac{1}{2}K_\parallel^2+\epsilon_{n,n'}+\omega^+)^2}-\sqrt{-(-\frac{1}{2}K_\parallel^2+\epsilon_{n,n'}-\omega^+)^2}\right)\right].
\end{aligned}
\tag{3.57}
$$

After getting the noninteracting response-response function χ^0, we can evaluate RPA response function χ^{RPA} following the Eq. (2.52) through

$$
\chi^{RPA} = \frac{\chi^0}{1-\chi^0 K}. \tag{3.58}
$$

The absorption is then calculated with χ^{RPA} as

$$S = \omega \int dr dr' V^*_{ext}(r,q) Im\chi^{RPA}(r,r',q) V_{ext}(r',q), \tag{3.59}$$

where V_{ext} has different forms for nD structures

$$\begin{cases} V_{ext,0D}(r,L) = r^L \\ V_{ext,1D}(r,L,q) = I_m(kr) \\ V_{ext,1D}(r,q) = e^{kr} \end{cases}. \tag{3.60}$$

In the end, we can check the numerical absorption results by using energy-weighted sum rule introduced in Section 2.3.3.

An alternative way to calculate the absorption is to use the e-h pair basis set. The strategy is presented as following.

When we use e-h pairs as basis, the noninteracting response function has a simple diagonal form

$$\chi^0(ab,a'b') = \frac{f_a - f_b}{\omega + (E_a - E_b)} \delta(ab,a'b'), \tag{3.61}$$

where $a \equiv \{n_a, k_a\}$ indicates the electronic state; E_a and f_a are the energy and occupation number of a given state; ω and k are the energy and momentum of the external excitation. Clearly, the configuration ab has to be electron-hole eh or hole-electron he to ensure the $f_a - f_b \neq 0$. The residue interaction under this basis set is

$$K(ab,a'b') = \int dr dr' \phi_a(r)\phi_b(r) K(r,r') \phi'_a(r')\phi'_b(r'). \tag{3.62}$$

Our purpose is to find the singularities of χ^{RPA}. This is equivalent to solve

$$\Phi(z) - \sum_z \frac{f_z}{\omega - E_z} K(z,z')\Phi(z') = 0, \tag{3.63}$$

where $z = ab$ corresponds to the configuration, $E_z = E_b - E_a$ is the energy for configuration ab excitation, and $f_z = f_a - f_b$ is the change of the e-h pair number??.

We define $\Phi(he) = x$ for $f_z = 1$ and $\Phi(eh) = y$ for $f_z = -1$, which essentially corresponds to create and annihilate an e-h pair in the system. Equation (3.63) can be expanded as

$$\begin{cases} (\omega - E_x)\, x - \sum_x K(x,x')x' - \sum_y K(x,y')y' = 0 \\ (\omega - E_y)\, y + \sum_x K(y,x')x' + \sum_y K(y,y')y' = 0 \end{cases}, \tag{3.64}$$

which give

$$H^{RPA} \begin{pmatrix} X \\ Y \end{pmatrix} = \begin{pmatrix} A & B \\ -B & -A \end{pmatrix} \begin{pmatrix} X \\ Y \end{pmatrix} = \omega \begin{pmatrix} X \\ Y \end{pmatrix}, \tag{3.65}$$

where we have

$$\begin{aligned} A &= K_{XX} + E_{XX} = K_{YY} - E_{YY} \\ B &= K_{XY} = K_{YX}, \end{aligned} \tag{3.66}$$

where K_{XX} is the interaction matrix between he configurations, E_{XX} is the diagonal matrix $E_x\delta(x,x')$, and similar definitions stand for the other matrices. The normalization condition is

$$X^2 - Y^2 = 1, \tag{3.67}$$

which corresponds to excite one e-h pair in the system. To calculate the absorption, we simply add up contribution from all different pairs by

$$S = \sum_x |\, \langle x|V_{ext}|0\rangle\, x|^2 + \sum_y |\, \langle y|V_{ext}|0\rangle\, y|^2. \tag{3.68}$$

The underlying physics here is presented as follows: χ^0 is the Green's function of the non-interacting e-h pair Hamiltonian $H_0 = (f_b - f_a)(E_a - E_b)\delta_{ab,a'b'}$. The interaction K (bare coulomb interaction in RPA) between different e-h pairs is then treated as a perturbation to the noninteracting e-h pair system. By solving the effective

Hamiltonian H_{RPA} *, combined (ing) with? H_0 and K, we can obtain a new set of "quasi" e-h pair states, and each of such quasi e-h pair states is a superposition of the non-interacting e-h pairs. In particular, among these eigenstates of H_{RPA} are one or more special states, namely, the plasmon modes, that encompass maximal numbers of the noninteracting e-h pairs in a constructive way. These are also the modes interacting most strongly with the external field.

3.5 Energy of Surface Plasmons: a Simple Quantum Derivation

In this section, we derive the surface plasmon frequency using quantum mechanics. This frequency has been evaluated by Feibelman [24]. Here we use a little different procedure. We consider a semi-infinite bulk filling the space $z > 0$. From Eq. (3.49), we can clearly see that when $q \to 0$, the interaction between e-h pairs has the form $2\pi/q$ without any z dependence. Therefore, the amplitude of any interband transition is vanished due to the orthogonality of wavefunctions. In this case, only the intraband e-h pairs contribute to the response function, which has the noninteracting form,

$$\begin{aligned}\chi_0 &= \sum_{\kappa,k} \psi_\kappa^2(z)\psi_\kappa^2(z') D_{\kappa,k} \left[\frac{1}{\omega - \epsilon_{eh}} + \frac{1}{-\omega - \epsilon_{eh}}\right] \\ &= \sum_{\kappa,k} \psi_\kappa^2(z)\psi_\kappa^2(z') D_{\kappa,k} \frac{2\epsilon_{eh}}{\omega^2 - \epsilon_{eh}^2}.\end{aligned} \tag{3.69}$$

The coulomb interaction is

$$K(z, z') = \frac{2\pi}{q} e^{-q|z-z'|}. \tag{3.70}$$

*The non-Hermitian nature of the effective Hamiltonian is due to the quasiboson approximation, which means that we use the Kohn-Sham ground state instead of the real RPA ground state. In this case the annihilation of an e-h pair will always decrease the energy of system, giving the negative eigenvalues for Hamiltonian.

To find the plasmon frequency, it is necessary to solve

$$\psi(z) - \int dz' dz'' K(z, z'') \chi_0(z'', z') \psi(z') = 0. \tag{3.71}$$

For each band κ, we define its maximum transverse momentum $k_\kappa = \sqrt{2(E_F - E_\kappa)}$. Then for small q, the energy of e-h pair is

$$\epsilon_{eh} = q \cdot k + \frac{q^2}{2}. \tag{3.72}$$

We then have

$$\begin{aligned}
&\int dz'' K(z, z'') \chi_0(z'', z') \\
&= \frac{2\pi q}{\omega^2} \int dz'' e^{-q|z-z''|} \sum_\kappa \rho_\kappa(z'') D_\kappa \\
&= \frac{2\pi q}{\omega^2} \left[\int_{-\infty}^{z} dz'' e^{-q(z-z'')} n(z'') + \int_z^{\infty} dz'' e^{q(z-z'')} n(z'') \right] \\
&= \frac{2\pi}{\omega^2} \Bigg[\left(n(z'') e^{-q(z-z'')} \right) \Big|_{-\infty}^{z} - \int_{-\infty}^{z} dz'' e^{-q(z-z'')} \frac{dn(z'')}{dz''} \\
&- \left(n(z'') e^{q(z-z'')} \right) \Big|_{z}^{\infty} + \int_z^{\infty} dz'' e^{q(z-z'')} \frac{dn(z'')}{dz''} \Bigg] \\
&= \frac{2\pi}{\omega^2} \left[n(z) - (n(z) - n(-\infty)) + n(z) + (n(\infty) - n(z)) \right] \\
&= \frac{2\pi}{\omega^2} \left[n(\infty) + n(-\infty) \right] = 1,
\end{aligned} \tag{3.73}$$

which implies

$$\omega = \sqrt{2\pi n_0} = \frac{\omega_p}{\sqrt{2}}. \tag{3.74}$$

This shows a pure quantum mechanical derivation of surface plasmon frequency.

3.6 Energy and Lifetime of Plasmons

In this section, we present a comprehensive study of the plasmon lifetime in a series of highly confined geometries, including zero-dimensional ($0D$) nanoshells, $1D$ coaxial

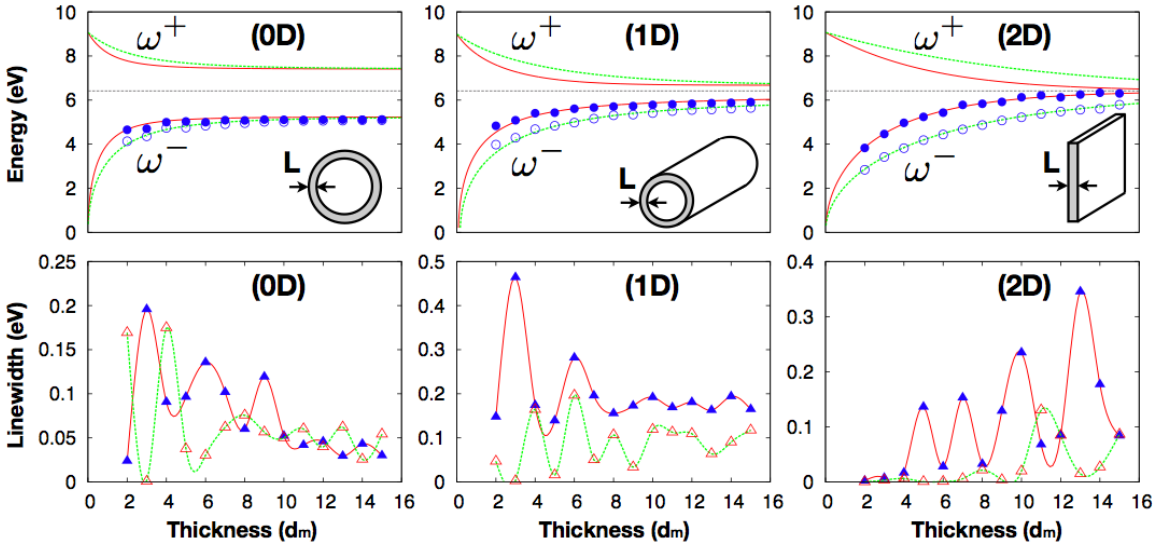

Figure 3.3: Thickness dependence of the plasmon energy and linewidth in different confined geometries. The top panels are the energy spectra, including both the hydrodynamic (lines) and RPA (circles) results. The bottom panels are the linewidths from the RPA calculations. For all the geometries, external field is modeled within the dipole scattering regime. For $0D$ and $1D$, we have the fixed inner radius $2d_m$ (solid triangle) and $4d_m$ (open triangle), respectively. For $1D$ and $2D$, the momentum transferred to an e-h pair is given by $k = 0.025\,a.u.$ (open triangle) and $k = 0.05\,a.u.$ (solid triangle).

nanotubes, and $2D$ ultrathin films, using the random phase approximation (RPA) combined with both the traditional real space and a distinctive electron-hole (e-h) pair basis sets. These prototype structures can exhibit wide frequency tunability [45, 51], a salient feature highly desirable in developing plasmonics technology. Furthermore, our present study shows that the linewidth of the plasmons can also be sensitively tuned, as represented by their strong oscillations as a function of the system size in the quantum regime. Such oscillatory behavior deviates qualitatively from the expectations of the classical surface scattering picture, and can be rationalized by the size dependence of the quantized e-h pairs contributing to the Landau damping. Our approach also reveals the underlying physical origin for the hybridization broadening mechanism of near degenerate plasmon modes. These findings amount to an improved understanding of the underlying physical mechanisms for intrinsic lifetime broadening of surface plasmons, and may prove to be instrumental in future design of plasmonic devices.

In our studies, we first use the traditional RPA approach to evaluate electron density-density responses in real space [51–55]. More importantly, we also use the e-h pair basis set to evaluate the state-state responses in order to reveal the underlying composition of the plasmon resonance. As shown later, in this basis both the Hamiltonian describing non-interacting e-h pair excitations and the corresponding response function are in simple diagonal forms. In paticular, when interactions among the e-h pairs are included, the energy of the plasmons can be obtained directly from the effective interacting Hamiltonian, exhibiting clear advantages of the e-h pair basis. For electron levels in the ground state, we use the jellium model with the Wigner-Seitz radius $r_s = 3.0$ and work function $W = 4.6\,eV$, representing silver. The interlayer spacing $d_m = 0.236\,nm$ along the Ag (111) direction is used as the unit of length.

Figure 3.3 displays the thickness dependence of the plasmon energy and linewidth in the three different confined geometries, each case with two structure examples. For each geometry, when the thickness is large, each surface supports a plasmon mode independently. As the thickness decreases, an antisymmetric ω^+ and a symmetric

ω^- modes will be formed due to the coupling between the two surface modes. The frequency dispersions of these two plasmon modes can be first estimated using the hydrodynamic model [56, 57], as shown by the solid lines in Fig. 3.3. Our real-space RPA results (dots) for the ω^- mode are very close to the hydrodynamic results, suggesting that for the plasmon energy dispersions, one can ignore the detailed electronic structures. However, they are crucial for the linewidth broadening. Here, we also note that we have focused on the ω^- mode in our RPA study, because the ω^+ mode is usually strongly damped, playing a much less significant role in plasmonics.

Some intriguing features can be observed in the Landau damping of the ω^- modes [†]. First, the pronounced oscillations exist in all confined structures. Here we note that similar oscillations have been reported for other geometries [55, 58], but the underlying physical origin remains elusive, and will be fully revealed later using the e-h pair basis set. Secondly, the trends in the linewidth deviate drastically from the $1/L$ dependence expected from the semiclassical surface scattering picture. These observations imply that one cannot describe those systems using simple phenomenological dielectric functions.

Now we start from the detailed electronic structure to elucidate the origin of the oscillations in the plasmon linewidth, using thin films as representative systems. Because of the strong confinement, the energy levels of thin films consist of a series of subbands and each electronic state is labelled by the subband index n and the momentum parallel to the film plane. Consequently, an e-h pair can be labeled by the band index difference $|\Delta n|$ and momentum difference k between the electron and hole states. In addition, because of the mirror symmetry in thin films, we can divide the e-h pairs into two decoupled groups, $|\Delta n|$ odd or even, which contribute to the ω^+ and ω^- plasmon modes, respectively.

[†]In the real-space RPA approach, a numerical broadening procedure must be applied to extract the linewidth of the plasmon mode. This amounts to introduce a finite η in the unperturbed response function χ_0 in Eq. (3.61). In the linewidth plots of Fig. 3.3, we have subtracted this initial broadening used in our calculations, $0.1\,eV$ for $0D$ and $0.04\,eV$ for $1D$ and $2D$, to highlight the intrinsic linewidths due to Landau damping.

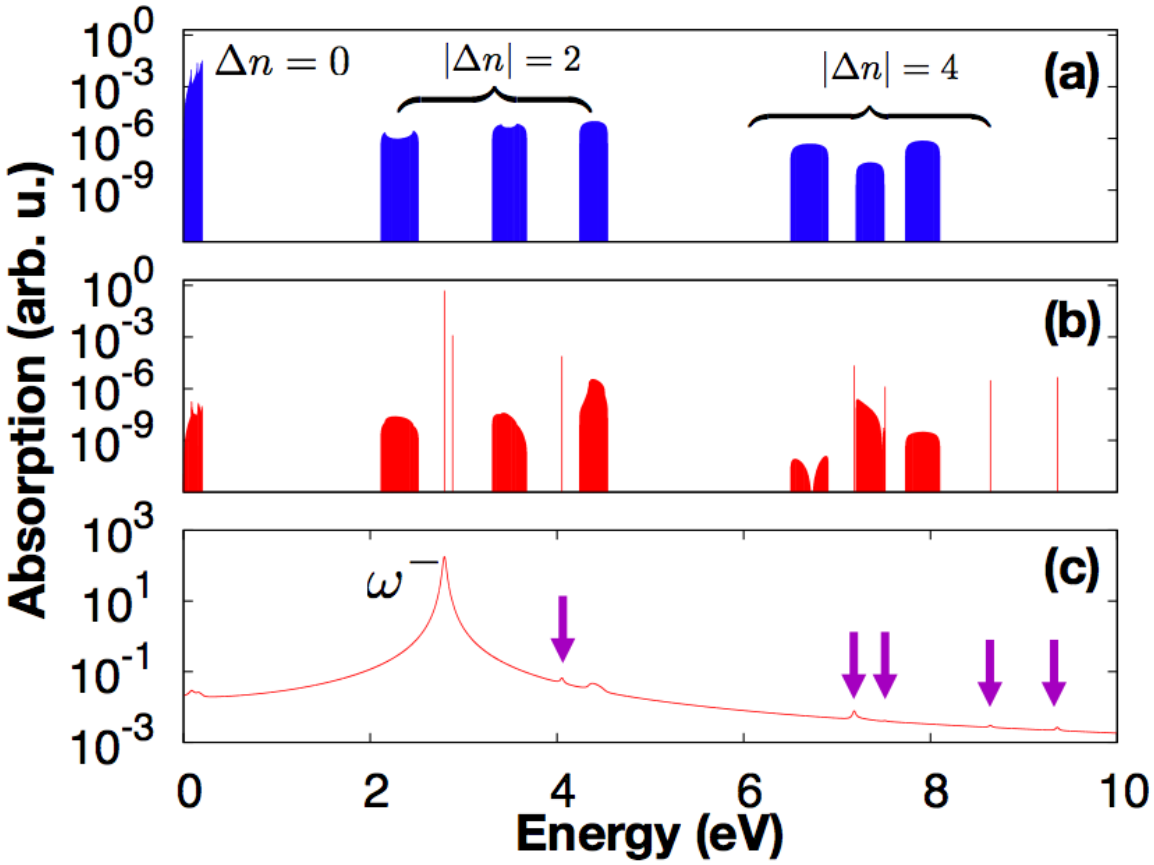

Figure 3.4: The absorption spectra (a) without and (b) with e-h pairs interactions, for a thin film of thickness $4d_m$ and $k = 0.012\,a.u.$. (c) is the result of (b) broadened by a Lorentzian with full width at half maximum $\gamma = 0.04eV$.

Figure 3.4 contrasts the absorption spectra calculated without or with the e-h pair interactions, focusing on the ω^- mode with even $|\Delta n|$, where the e-h pairs with transitions from the confined states to the vacuum continuum have very minimal effects on the plasmon energy and linewidth, and can therefore be ignored. In the noninteraction case (Fig. 3.4(a)), we can clearly see that the absorption spectra is made of disconnected bands due to the discretization of the individual electron levels, where the width of each band comes from the variation in kinetic energy $(\frac{1}{2}k_a^2 - \frac{1}{2}k_b^2)$ for a fixed $k = k_a - k_b$. As k increases, the disconnected bands will expand in width and eventually will fill up the gaps among them (see Fig. 3.5(a) and later discussions for more details). In contrast, for a semi-infinite metal, the corresponding absorption spectrum for the noninteracting case would produce only one continuum. Here, when the interactions between the e-h pairs are switched on, we obtain Fig. 3.4(b), which exhibits absorptions due to both disconnected bands and the isolated plasmon modes. Because of the presence of a sum rule in the spectral weights, the plasmon modes gain their absorption strength from the noninteracting absorption bands, and therefore can be classified by their main contributors. For example, the one with the strongest absorption around $2\,eV$, corresponding to the ω^- mode, inherits its high absorption strength from the intra-subband e-h pairs ($\Delta n = 0$). For $|\Delta n| = 2$, each absorption band contributes a plasmon mode, with the first two modes confined in the gap regions, and the third one far way from the originated band. As k increases, all the low lying plasmon modes will disappear by merging into absorption bands, leaving the one with the highest energy the only surviving plasmon mode of the resultant single e-h pair continuum; this surviving mode eventually evolves into the bulk plasmon mode [53]. The above discussions vividly depict the evolution of the plasmons from the quantum to the classical regime.

An advantage of using the e-h pair basis set is that the collective modes are obtained naturally as eigenstates of the Hamiltonian matrix H_{RPA}, which allows us to easily identify multiple plasmon modes originating from the intra- and inter-band transitions. This is in sharp contrast to the traditional real-space RPA approaches,

where initial numerical broadening must be introduced. To further demonstrate the power of our approach, we compare the absorption spectra obtained using the e-h pair basis set (Fig. 3.4(b)) with its counterpart obtained via numerical broadening in Fig. 3.4(c). We can clearly see that in the latter case the inter-band plasmon modes (arrows) with weak absorption strengths are "washed out" by such a numerical broadening and become indistinguishable, leaving only the ω^- mode as the clearly observable mode.

We now return to the oscillatory nature of the ω^- mode linewidths shown in Fig. 3.3. Instead of showing the thickness dependence, we study the momentum dependence of the linewidth, where the e-h pair spectra show continuous variations. The underlying reason can be elucidated by comparing the dispersions of the plasmon and the *noninteracting* e-h pairs in Fig. 3.5(a). When the plasmon energy (solid line) passes through the gap regions of the e-h pair spectra, Landau damping should be strongly suppressed due to the lack of decay channels. In Fig. 3.5(b), following the plasmon trajectory, we plot the corresponding e-h pair density and linewidth. Indeed, for the momentum $k \geq 0.03\, a.u.$, the magnitude of the plasmon linewidth correlates well with the e-h pair density. However, deviations from this trend are clearly visible for smaller momenta. First, no peaked values in the linewidth are observed at the locations where the interband e-h pairs are highly peaked. This can be understood by the fact that the ω^- mode is dominantly contributed by the intraband transitions, and the coupling between the intraband and interband e-h pairs are very weak. More intriguing in Fig. 3.5(b) is the peak in the linewidth at momenta where the e-h pair density shows a minima. To resolve this counter-intuitive observation, we go back to Fig. 3.4, where we have compared the absorption spectra with and without numerical broadening for $k = 0.012\, a.u.$ (indicated by the vertical dashed line passing through Fig. 3.5). By comparing Figs. 3.4(b) and 3.5(c), we can clearly see that the unexpected linewidth peak is due to the numerical broadening of two near degenerate plasmon modes, which cannot be resolved if the traditional real-space RPA approach was used. This broadening mechanism due to plasmon hybridization is different from the

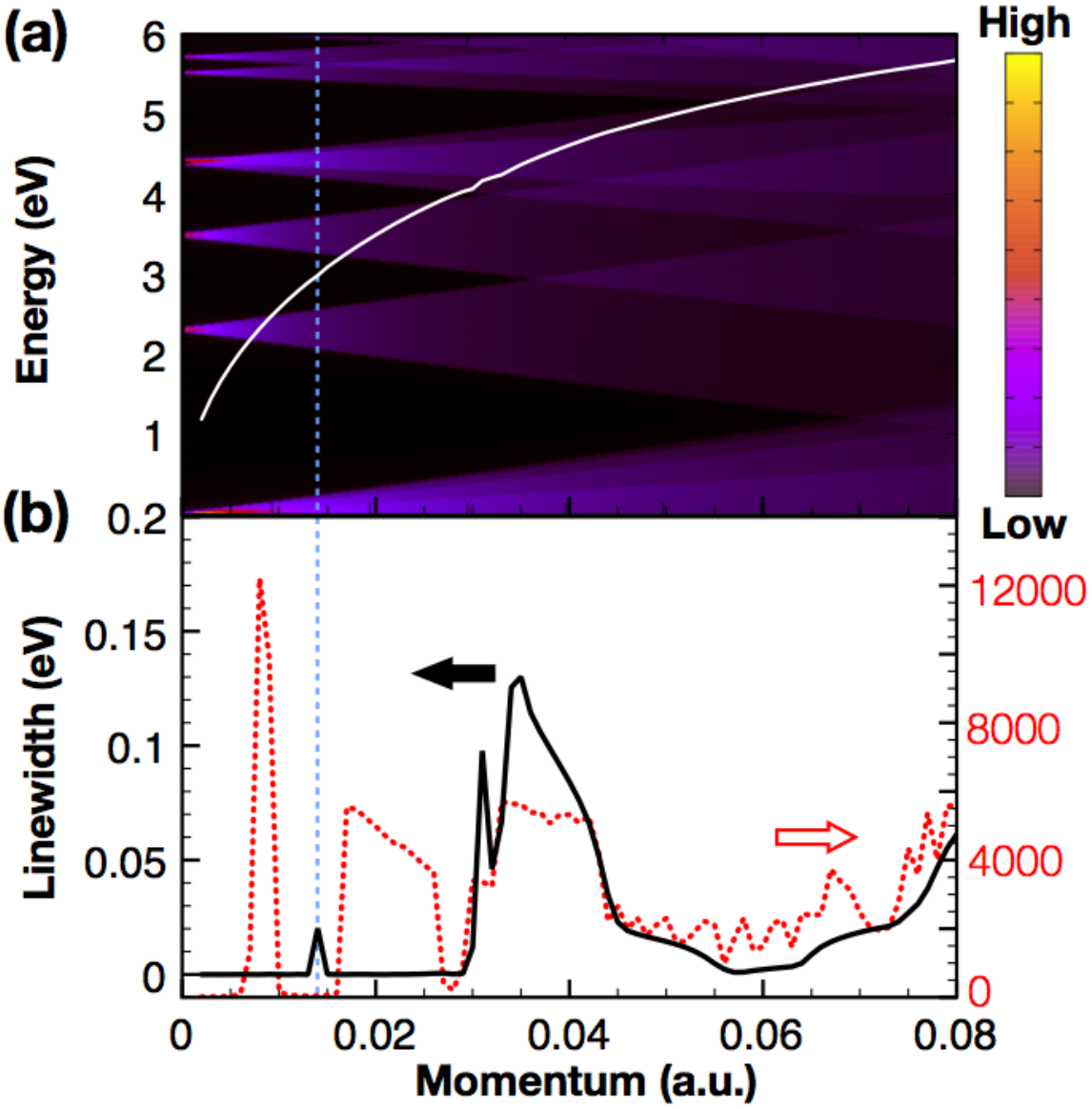

Figure 3.5: (a) dispersion relations of the ω^- plasmon (solid line) and the non-interacting e-h pairs (color) for a thin film of thickness $4d_m$. (b) linewidth of the plasmon (solid line) and density of the e-h pairs (dashed line) along the plasmon trajectory shown in (a).

traditional Landau damping mechanism of plasmon/e-h pair coupling. Furthermore, such a hybridization broadening of near degenerate plasmon modes can also take place inside an e-h pair continuum, as indicated by the plasmon linewidth peak around $k = 0.03$ in Fig. 3.5(b).

In summary, we have performed a comprehensive study of the energy and linewidth of plasmons in various quantum metal structures. We found that Landau damping, as the main dissipation channel in this regime, can be drastically tuned due to energy quantization of the individual electron levels and e-h pairs. The generic oscillatory nature of the tunability is in stark contrast with the expectations of a semiclassical surface scattering picture. The use of an e-h pair basis also allows us to reveal the underlying physical origin for strong hybridization broadening of near degenerate plasmon modes. These findings are expected to guide future designs of plasmonic nanostructures of wide applicability.

Chapter 4

Plasmons of Metal Thin Films in Dielectric Environment

In previous chapter, we have studied the plasmon excitation in free-standing metal structures. However, in experiments the metal structure is always placed on some substrate, therefore it is important to understand the substrate effect on plasmonic properties of a metal-substrate structure, which is the subject of this chapter. Our results qualitatively reproduce the experimentally observed plasmon spectra of the Mg/Si systems. The underlying physics of the formation of various absorption peaks can be understood using the simple hybridization concept. Based on this concept, the coexistence of surface and bulk plasmons in the experimental observation turns out to be a clear evidence for the existence of multiple-multipole surface plasmons due to the quantum confinement in thin films.

4.1 Introduction

Metal surfaces are attractive playgrounds for various physical and chemical processes, including surface growth, chemical catalysis, etc. In particular, the collective electronic excitations at a metal surface have received tremendous attention regarding

their interaction with electric fields. In thick metal films, which can be modeled as a semi-infinite system, the various collective modes are well understood and excellent agreement between experimental and theoretical results has been reached [59–62]. On the other hand, for metal thin films, the situation is much more complicated due to contributions from different channels, such as quantum size effect and substrate.

The best-known collective mode on metal surfaces is the surface plasmon discovered by Ritchie in 1957, which has a monopole nature perpendicular to the surface. Later on, the multipole surface plasmon, which has a dipole characteristic, was predicted by hydrodynamic approach [63] and identified at alkali metal surface [59]. Based on the quantum study by Feibelman [24], the dispersion of surface plasmons of a semi-infinite metal can be simply described by the relation

$$\omega_{sp}(q) = \frac{\omega_p}{\sqrt{2}} \left(1 - \frac{q}{2} d_\perp(\omega)\right). \tag{4.1}$$

Here $d_\perp(\omega)$ is the centroid of the induced charge distribution $\delta n(r, \omega)$,

$$d_\perp(\omega) = \frac{\int dr\, r\, \delta n(r,\omega)}{\int dr\, \delta n(r,\omega)}, \tag{4.2}$$

where r is the direction perpendicular to the surface and is measured from the surface. This result shows that the surface plasmon has the energy exactly equal to $\omega_p/\sqrt{2}$ at $q = 0$. More importantly, it indicates that when $d_\perp(\omega) > 0$ is outside the jellium edge of metal, the surface plasmon shows a negative dispersion, which agrees with experimental observations [64, 65].

In many early studies of plasmon modes, the thin film was usually placed on metal substrates [66–68]. In order to take into account the substrate effect, Liebsch introduced a hybridization concept to explain the observed experimental results for the thickness and momentum dependence [69, 70].

Here, we consider the metal-dielectric structures. We expect that the dielectric substrate is more helpful to elucidate the quantum size effect of the thin film than

a metal substrate. This is because the electrons in a metal substrate will strongly permeate into the thin film and therefore may wash out the contribution from confined electrons, while dielectric substrates will not provide any other free electrons. Our calculation clearly produces the experimentally observed monopole and multipole surface plasmon, and bulk plasmon. The numerical results can be well understood using the hybridization concept. The coexistence of three different modes clearly indicates the multiple plasmon modes due to quantum confinement.

In the following, we will first present the modeling of the dielectric environment in our system, and discuss more details about the multipole plasmon and bulk plasmon in thin film structure. In the last section, a comprehensive study for the metal-dielectric structure is presented.

4.2 Effects of Dielectric Environment

We consider a general case by dividing the space into three regions with different dielectric constants

$$\epsilon(r) = \begin{cases} \epsilon_1 & r < r_1 \\ \epsilon_2 & r_1 \leq r \leq r_2 \\ \epsilon_3 & r_2 < r \end{cases}, \tag{4.3}$$

where the region with $\epsilon_{1,3} > 1$ is the dielectric environment, and ϵ_2 is the dielectric contribution from the localized electron bands in metals, for example, the d-band contribution in noble metals.

In this system, we need to solve the Poisson equation for potential $\phi(r)$ with the dielectric function $\epsilon(r)$ given in Eq. (4.3)

$$\nabla^2\phi(\mathbf{r}) = \frac{4\pi}{\epsilon(\mathbf{r})} n(\mathbf{r}), \tag{4.4}$$

where $n(r)$ is the free charge density. This equation tells us that, due to the dielectric environment, the bounded charges will screen the free charges with the factor ϵ^{-1}. To

solve this equation, we calculate its Green's function, which essentially is the screened effective coulomb interaction $W(\mathbf{r}, \mathbf{r}')$. Again, due to the translational symmetry of system along the interface, we have the reduced form $W(r, r', q)$ through Fourier transform, where q is the quantum number corresponding to the symmetric direction,

$$\nabla^2 W(r, r', q) = \frac{4\pi}{\epsilon(r')}\delta(r - r'), \tag{4.5}$$

and the boundary conditions

$$\epsilon_i \frac{\partial W(r, r', q)}{\partial r}\bigg|_{r=r_i^-} = \epsilon_{i+1} \frac{\partial W(r, r', q)}{\partial r}\bigg|_{r=r_i^-}. \tag{4.6}$$

$W(\mathbf{r}, \mathbf{r}')$ has two contributions from both screened free charge $\delta(r - r')/\epsilon(r')$ and the bounded charge σ_i at the interface of different dielectric environment. So we can write it as

$$W(r, r', q) = \frac{1}{\epsilon(r')} \left[V(r, r', q) + \sigma_1 V(r, r_1, q) + \sigma_2 V(r, r_2, q) \right], \tag{4.7}$$

where $V(r, r', q)$ is the bare coulomb interaction as shown in Eq. (3.49). Then the boundary conditions can be written as

$$\begin{aligned} &\epsilon_i \left[V'(r, r') + \sigma_1 V'(r, r_1) + \sigma_2 V'(r, r_2) \right]_{r=r_i^-} \\ &= \epsilon_{i+1} \left[V'(r, r') + \sigma_1 V'(r, r_1) + \sigma_2 V'(r, r_2) \right]_{r=r_i^+}. \end{aligned} \tag{4.8}$$

Finally, the interface bounded charge is

$$\sigma_1 = \frac{A_2 \epsilon_{12} V'(r_1, r') + \epsilon_{12}\epsilon_{23} V'(r_2, r') V'(r_1, r_2)}{A_1 A_2 - \epsilon_{12}\epsilon_{23} V'(r_1, r_2) V'(r_2, r_1)}, \tag{4.9}$$

and

$$\sigma_2 = \frac{A_1 \epsilon_{23} V'(r_2, r') + \epsilon_{12}\epsilon_{23} V'(r_1, r') V'(r_2, r_1)}{A_1 A_2 - \epsilon_{12}\epsilon_{23} V'(r_1, r_2) V'(r_2, r_1)}, \tag{4.10}$$

where

$$A_i = \epsilon_{i+1} V'(r, r_i)|_{r=r_i^+} - \epsilon_i V'(r, r_i)|_{r=r_i^-}. \tag{4.11}$$

Now, the Hartree potential can be readily calculated by using the screened interaction shown in Eq. (4.7). Then the rest of the calculation can be carried out as outlined in the previous chapter. To compare with existing experimental results, we have studied the Mg ($r_s = 2.66\, a.u.$) thin film on a silicon substrate, which is assumed to have non-dispersive dielectric value $\epsilon = 11.68$ for simplicity.

In Fig. 4.1, we compare the ground state electron density and total potential distribution of a free-standing thin film and a thin film on substrate structure. We can clearly see that although the change of electron density is very small, the potential difference is obvious. The spill-out effect of electrons in the metal-substrate interface is stronger due to the screening of surface charges from substrate polarization. These charges also cause the reduced total potential on the substrate side and the discontinuity of electric field, implied by the kink of potential at the metal-substrate interface.

Now we use several examples to show the change of plasmon excitations in the presence of different dielectric environment. In Fig. 4.2(a), we compare the results of $\epsilon_1 = \epsilon_3 = 1$ (blue) and $\epsilon_1 = \epsilon_3 = 11.68$ (red). The difference can be easily understood by combining the semi-infinite surface plasmon condition Eq. (3.19) and the hydrodynamic hybridization result Eq. (3.38). The surface plasmon frequency in Eq. (3.38) now equals $\omega_p/\sqrt{12.68}$, therefore both split peaks ω^+ and ω^- shift to lower energy. In the asymmetric case, using $\epsilon_1 = 11.68$ and $\epsilon_3 = 1$, we compare the results of $k = 0.02$ and $k = 0.05$. In the large k-sector, the effective interaction between the surface modes on two interfaces is weak, so they both approach their unperturbed frequencies $\omega_p/\sqrt{12.68}$ and $\omega_p/\sqrt{2}$. The $\omega_p/\sqrt{12.68}$ peak is hard to see, since it has very small weight, which will be discussed later. On the other hand, when the interaction is stronger in the small k-sector, two peaks will be pushed to move far away from each other due to hybridization. Clearly, there are two possible reasons that one may miss the lower energy peak in experiment. First, due to its small energy, it may merge into the huge zero-energy-loss peak of EELS spectrum.

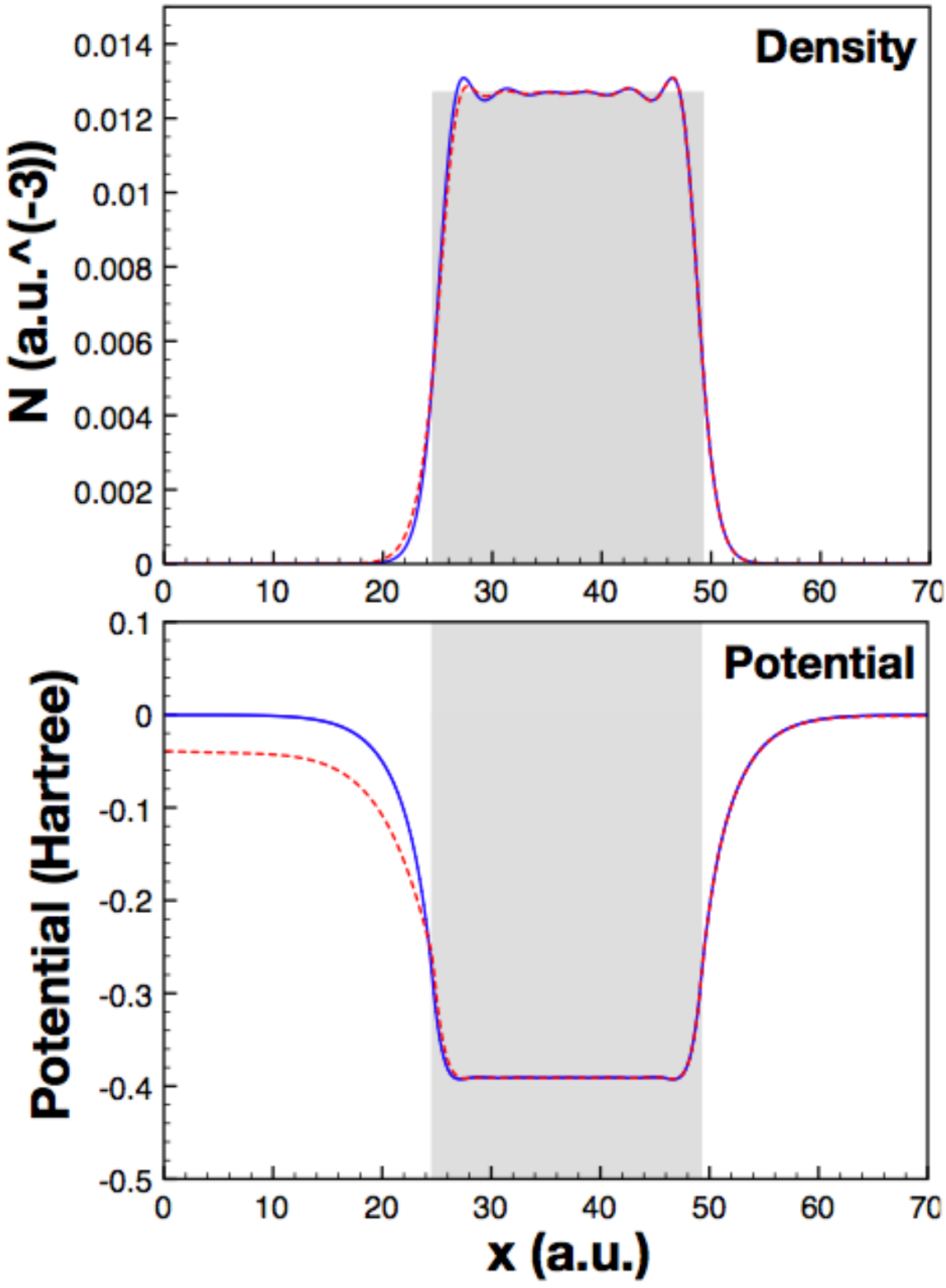

Figure 4.1: The electron density (a) and the total effective potential(b) in free-standing Mg thin film (blue solid) and the metal(Mg)-substrate(Si) structures (red dashed). The thickness of both thin films is five monolayers.

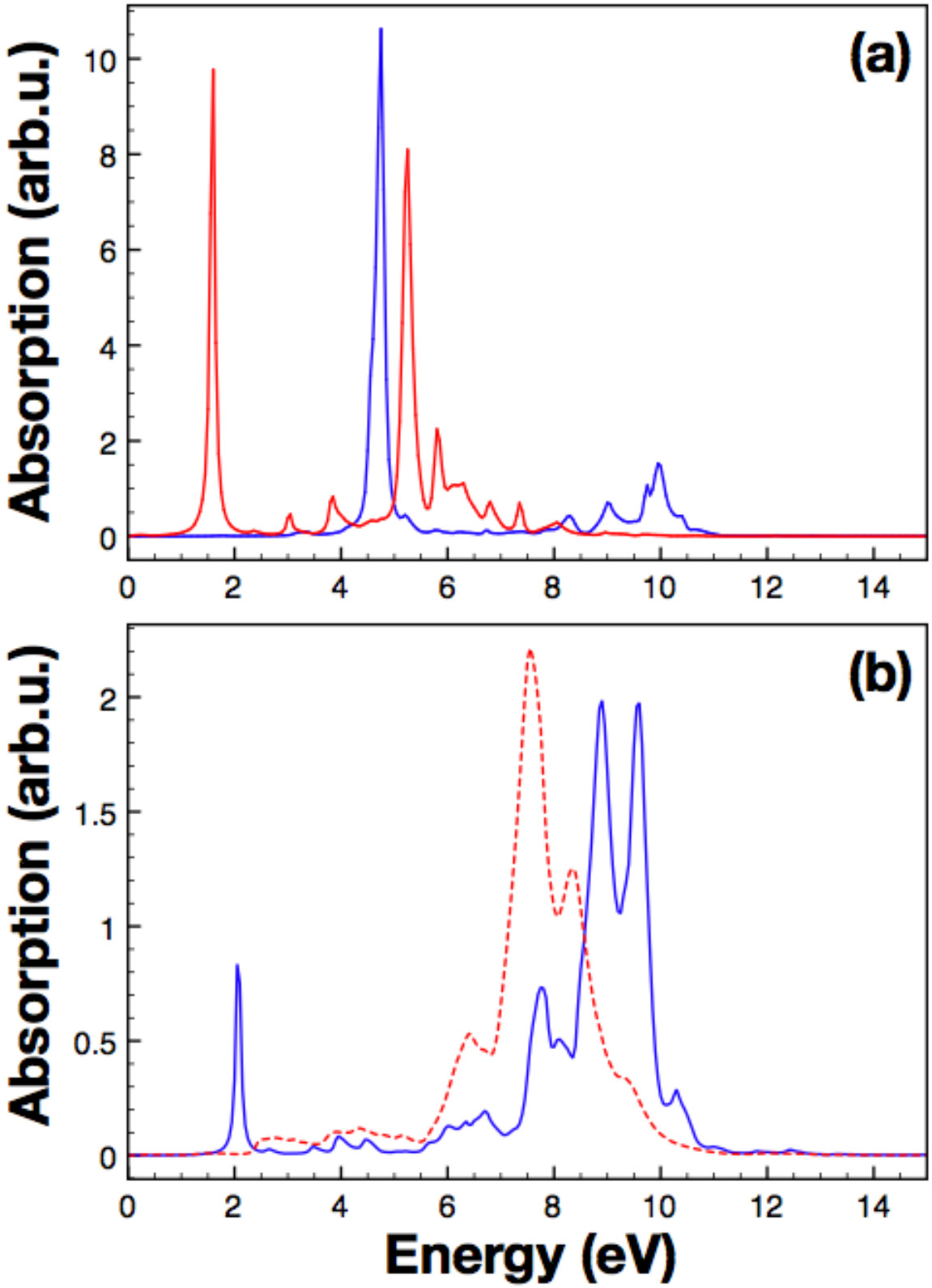

Figure 4.2: The absorption peaks in symmetric ($\epsilon_1 = \epsilon_3$) (a) and asymmetric ($\epsilon_1 \neq \epsilon_3$) structures (b). The solid (dashed) line stands for the momentum $k = 0.02$ ($k = 0.05$).

Second, the very small weight makes it hard to be observed even at higher energy as k is relatively large.

4.3 Mg (0001) Thin Films on a Si (111) Substrate

In this section, we further compare the symmetric and asymmetric results to explicitly show the reason that lower energy ω^- peak is missing. In Fig. 4.3, we can see that in the symmetric case, since the ω^+ and ω^- peaks have the same weight, the lower energy peak is huge. On the other hand, in the asymmetric plots, the energy weight is much smaller for the lower energy peak. Therefore as its energy increases, this peak disappears at large k. Interestingly, the effect of the substrate for the ω^+ seems very small except for the energy weight redistribution. It implies that the observed properties of ω^+ mainly reflect the electronic structures of thin film itself.

Focusing on the ω^+ branch, we now try to explain the detailed structures using the hybridization concept developed by Liebsch for the alkali-metal overlayers. In Fig. 4.4, we simplify our calculation by using a lower energy cut-off $7\,eV$ for the electron-hole pairs. This change will have a large effect on the linewidth of a plasmon, but very limited influence for the dispersion. Based on the Liebsch's arguments, the original ω^+ should change from bulk plasmon energy ω_p to surface plasmon energy $\sim 0.7\omega_p$ as k increases. When the multipole plasmon is considered, which appears at energy $\sim 0.8\omega_p$ and with slightly positive dispersion, two dispersion lines will cross with each other. Due to the interaction between the ω^+ and multipole plasmon modes, the ω^+ mode starts from ω_p will end up with multipole plasmon dispersion, and the multipole plasmon will follow the dispersion of ω^+ at large k. It is generally believed that only one multipole plasmon mode exists, therefore, the conclusion is that one should see energy peaks at ω_p and $0.8\omega_p$ at lower k and $0.7\omega_p$ and $0.8\omega_p$ peaks at larger k. This agrees with the experimental observation in alkali-metal overlayers. However, in our calculation, we can clearly see more than one band crossing in Fig. 4.4, which is the sign for the existence of multiple-multipole plasmons.

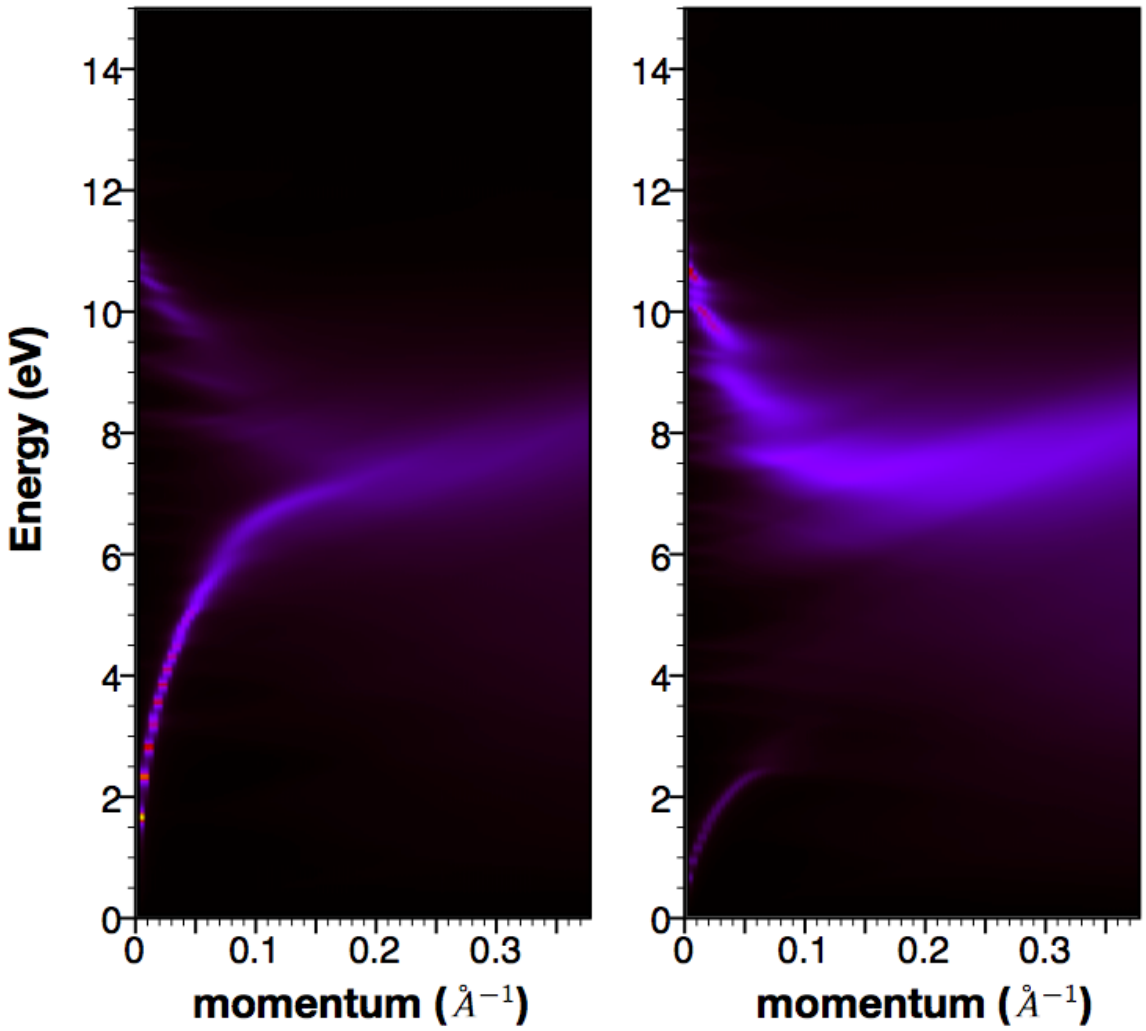

Figure 4.3: Momentum dependence of plasmon dispersion in free-standing (left) and substrate supported (right) Mg thin films with thickness five monolayers.

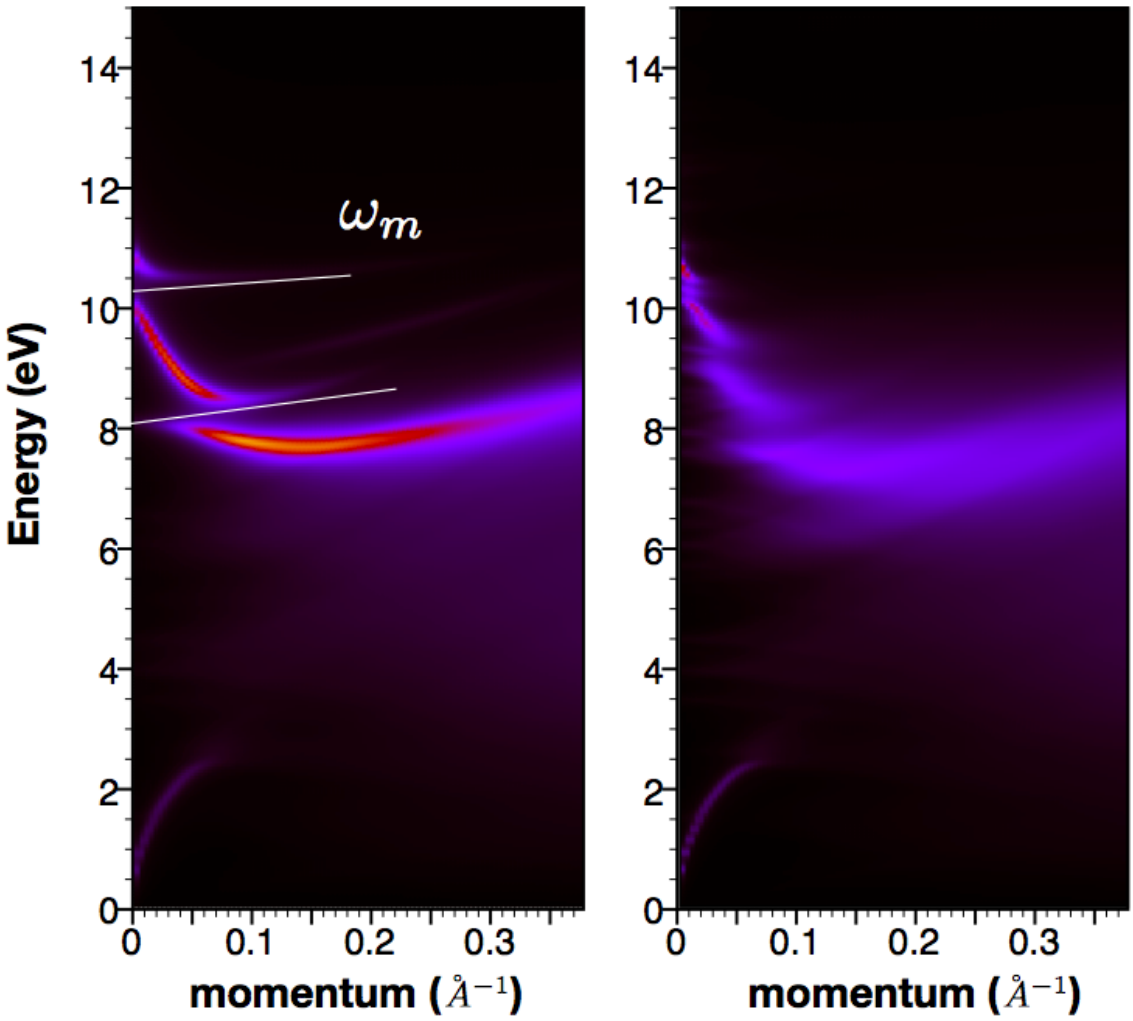

Figure 4.4: Plasmon dispersion calculated with electron-hole pair energy cut-off 7 eV (left) and $\sim$ 27 eV (right).

Since the decay of the relatively high energy multipole plasmon modes also involves the interband damping, in experiments the multiple plasmon will be hard to observe. However, the coexistence of monopole and multipole surface plasmon, and bulk plasmon can serve as an indirect evidence.

Finally, we compare our results with the experimental measurements. In Fig. 4.5, the $k = 0$ line corresponds to the measurement around $12 \sim 14$ degree. We can see that the bulk plasmon has relatively larger energy weight for smaller k, which agrees with our calculation. Also the negative dispersion of surface plasmon mode is observed in both experimental * and theoretical studies.

*Ao Teng and Hanno Weitering, private communication, April, (2010)

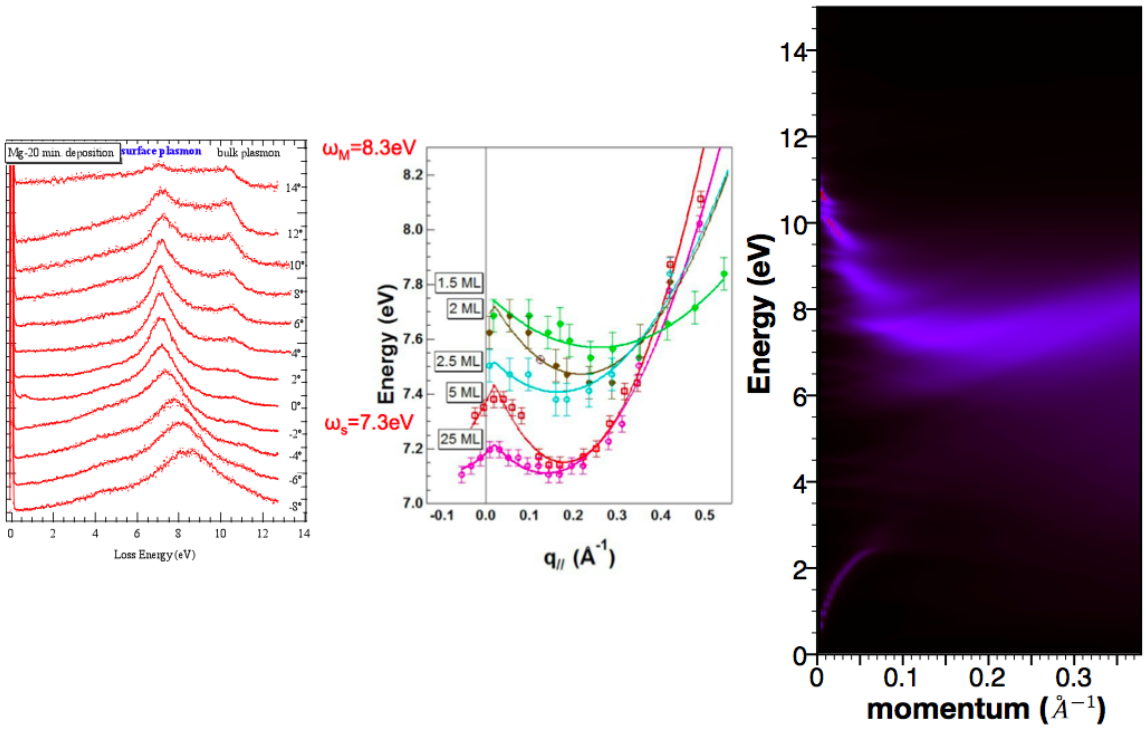

Figure 4.5: Plasmon dispersion compared with experimental results (left two figures).

Chapter 5

Transport Properties of Graphene Nanoribbons

5.1 Introduction

Recent years have seen a surge of interest in graphene materials [71–73], motivated by their potential application as a building block in future nanoelectronics [74]. Unlike conventional semiconductors, the charge carriers in graphene are described by a two-dimensional Dirac-like equation [75, 76] and display gigantic intrinsic mobility even at room temperature [77–79]. These unique properties are responsible for a slew of spectacular phenomena such as the half-integer quantum Hall effect [80–83] and Klein tunneling [76]. However, they also make it extremely difficult to manipulate the current-conducting state in graphene-based circuits. Among various schemes proposed to deal with this problem, a common solution is to induce a band gap in the energy spectrum by, for example, chemical doping in the bulk [84], or quantum size effect in nanoribbons [85].

More recently, there has been an increasing interest in bilayer graphene [86–102] because they allow easy tuning of the band structure via gate electrodes [103–107],

which in turn provides a promising avenue towards controlled transport in graphene-based circuits. The honeycomb lattice of a monolayer graphene consists of two atoms in a unit cell, conventionally labeled by A and B atoms. In bilayer graphene, the two layers are typically stacked in the so-called Bernard form in which an A atom of the top layer sits right above a B atom of the bottom layer (Fig. 5.1). Therefore, applying an electric field perpendicular to the layers will break the sublattice symmetry of the system and open a band gap. Experimentally, it has been demonstrated that the band gap can be tuned up to 250 meV [107], well into the midinfrared frequency range.

In addition, bilayer graphene also possess a pseudospin degree of freedom associated with the electron density difference between the two layers [108–110]. The aforementioned perpendicular electric field plays the role as a "Zeeman" field that couples to the pseudospin. Based on this analogy, San-Jose *et al.* [110] proposed a pseudospin valve (PSV) device that consists of a bilayer graphene with a pair of adjacent gate electrodes. This device operates in a similar way as the spin-valve [8], i.e. by changing the polarity of the gate voltage, parallel and antiparallel pesudospin configurations can be realized and the device can be switched between the on and off states. It has been shown that a large on-off ratio of the conductance can be achieved when the Fermi energy lies just outside the bulk band gap.

The issue to be addressed in this chapter is the effect of confined geometry, particularly the appearance of the edge states, on the PSV. Graphene materials are known to have edge states on zigzag edges [111, 112], which can significantly affect the transport properties of the system [113, 114]. Here we demonstrate by numerical simulations that a "midgap" PSV effect exists in bilayer graphene nanoribbons, in which the device can operate with a large on-off ratio even when the Fermi energy is inside the bulk band gap. This effect is possible because in addition to the flat-band edge states typically found in monolayer graphene, bilayer graphene also has edge states that are dispersive and extend well into the bulk band gap [115]. It is these states that carry currents when the bulk states are not available. Moreover, due

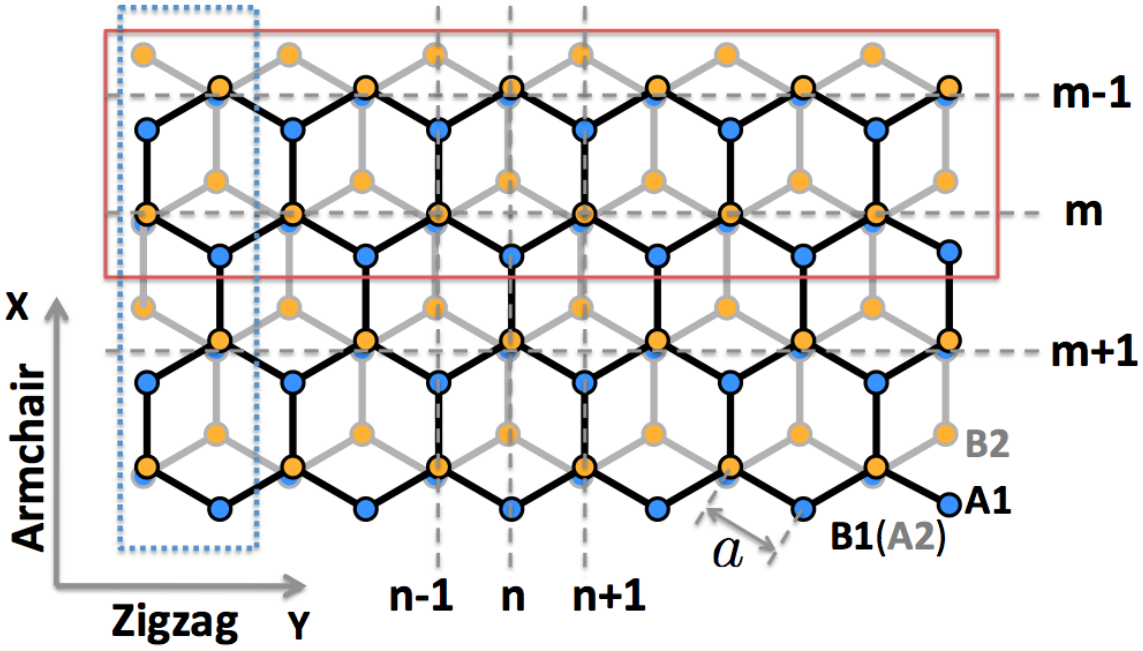

Figure 5.1: Geometry of a bilayer graphene nanoribbon. Black bonds connect atoms in the top layer, and grey bonds connect atoms in the bottom layer. The line in the armchair direction is labeled with n and the zigzag direction is labeled with m. An armchair nanoribbon with width Nw_a, where $w_a \simeq 2.46\,\mathring{A}$ is the width of a single armchair chain, has $4N$ atoms in a principal layer (in red frame), and a zigzag nanoribbon with width Mw_z, where $w_z \simeq 2.13\,\mathring{A}$ is the width of a single zigzag chain, has $4M$ atoms in a principal layer (in blue frame).

to the non-localized property of these edge states, the midgap PSV effect is robust against edge defects. Our result also shows that a smooth gate potential, as one is likely to encounter in real experiments, will have limited influence on the operation of this device. These features make PSV a highly desired method to control electric currents in graphene-based circuits with confined geometry.

This chapter is organized as follows. Section 5.2 describes electronic properties of graphene and bilayer graphene. In Sec. 5.3, conductance of both armchair and zigzag bilayer graphene nanoribbons is studied in detail by recursive Greens function method. We close this chapter with a summary in Sec. 5.4.

5.2 Graphene

Graphene is a two-dimensional (2D) material composed of monolayer carbon atoms with sp^2 orbital hybridization and the honeycomb lattice structure. Before it was successfully fabricated and observed in 2004 [71], no one expected the existence of monolayer free standing materials, since theoretically it was shown that those systems are unstable due to thermal fluctuations [116–119]. Therefore, the unexpected discovery of graphene stimulated enormous interests in properties of 2D systems over these years.

The lattice and electronic structures of a monolayer graphene are shown in Fig. 5.2(a). The honeycomb lattice consists of two equivalent atoms in a unit cell, conventionally labeled by A and B atoms. The wavefunction of its quasiparticles can then be represented by a vector $(\phi_A, \phi_B)^T$ with two components ϕ_A and ϕ_B corresponding to A and B sites, respectively. This two-folders form?? of wavefunctions implies the existence of a *pseudospin* degree of freedom. In addition, the electronic structures of graphene show linear dispersions near two inequivalent points K and K' at the corners of the Brillouin zone, where the quasiparticles are governed by the Dirac-like equation [120] rather than the Schrödinger equation. Also, we can see another useful "valley" degree of freedom corresponding to the

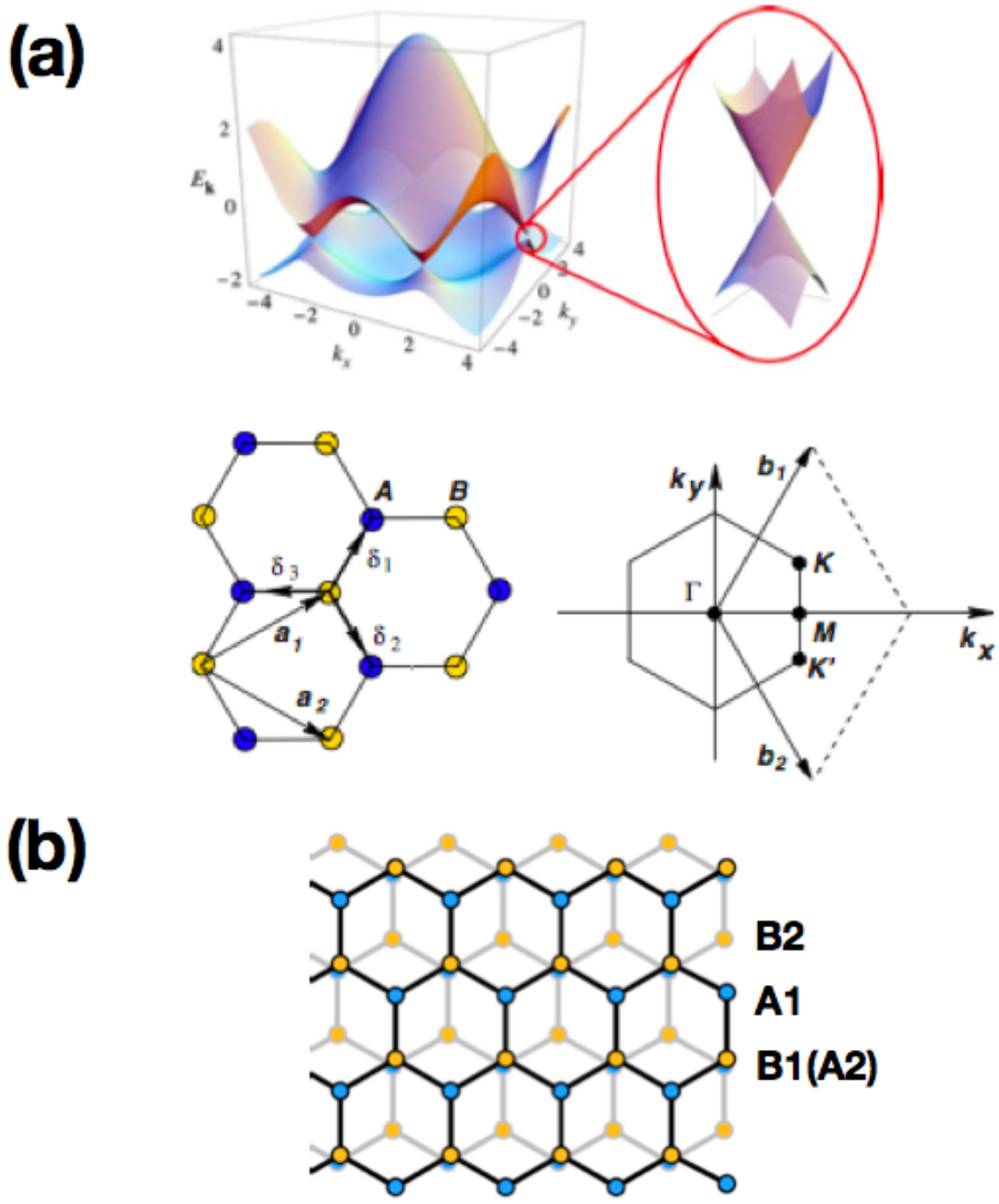

Figure 5.2: (a) Electronic dispersion in the honeycomb lattice. Upper: energy spectrum and zoom in of Dirac points. Lower: honeycomb lattice and its Brillouin zone. The lattice structure of graphene is made out of two interpenetrating triangular lattices A and B (a_1 and a_2 are the lattice unit vectors, and δ_i, $i = 1, 2, 3$ are the nearest-neighbor vectors.). The Dirac cones are located at the K and K' points [72]. (b) Lattice structure of bilayer graphene. The A_i (B_i) are A atoms in the layer i.

quasiparticles at the two well separated points K and K' in reciprocal space. The additional degrees of freedom and the special linear energy-momentum dispersion provide graphene many interesting transport properties.

5.2.1 Monolayer graphene

A single layer graphene sheet can be described by the tight-binding Hamiltonian

$$H = -t \sum_{<i,j>} (a_i^\dagger b_j + h.c.). \tag{5.1}$$

In single layer graphene, the low-energy effective Hamiltonian has a form

$$H = v_F \begin{pmatrix} V_A & p_x - ip_y \\ p_x + ip_y & V_B \end{pmatrix}, \tag{5.2}$$

where $p = (p_x, p_y)$ is the 2D momentum expanded around K point of the Brillouin zone, $v_F \simeq 10^6$ m/s is the Fermi velocity (Henceforth, we will set $v_F = 1$ for convenience), and $V_A(V_B)$ is the on-site energy of A(B) atoms. Now, supposing $V_A = -V_B = \Delta$, one can write the wavefunction as a two-component spinor,

$$\Psi = \begin{pmatrix} \psi_A \\ \psi_B \end{pmatrix} = \frac{1}{\sqrt{2}} \begin{pmatrix} \sqrt{1 - \frac{\Delta}{E}} e^{-i\theta_p/2} \\ \sqrt{1 + \frac{\Delta}{E}} e^{i\theta_p/2} \end{pmatrix}, \tag{5.3}$$

where $\theta = \arctan(p_y/p_x)$. Then the pseudospin is defined as

$$\langle \Psi | \boldsymbol{\sigma} | \Psi \rangle = \sqrt{1 - (\Delta/E)^2} (\cos\theta_p \hat{x} + \sin\theta_p \hat{y}) + (\Delta/E)\hat{z}. \tag{5.4}$$

Now, we can see that, when $\Delta = 0$, the pseudospin points into the same direction as the momentum. So the backscattering on a potential barrier tends to be suppressed due to the pseudospin conservation. This explains the Klein tunneling effect [76] in single layer graphene.

5.2.2 Bilayer graphene

The bilayer graphene with a biased voltage between the two layers can be described by the tight-binding Hamiltonian [72, 101],

$$\begin{aligned} H = & \sum_{l=1,2;<i,j>} \left(V_{l,i}^{A} a_{l,i}^{\dagger} a_{l,i} + V_{l,j}^{B} b_{l,j}^{\dagger} b_{l,j} \right) \\ & - t \sum_{l=1,2;<i,j>} \left(a_{l,i}^{\dagger} b_{l,j} + h.c. \right) \\ & - t_{\perp} \sum_{i} \left(a_{1,i}^{\dagger} b_{2,i} + h.c. \right), \end{aligned} \tag{5.5}$$

where l is the layer index and i, j label the unit cell within one layer. The operator $a_{l,i}(b_{l,j})$ annihilates an electron at the A(B) site in the ith unit cell of layer l. $V_{l,i}^{A,B}$ is the site energy, which can be controlled by the biased voltage, t is the intralayer nearest-neighbor hopping ($\simeq 2.9$ eV), and $t_{\perp}$ is the interlayer hopping ($\simeq 0.39$ eV) between A_1 and B_2, as shown in Fig. 5.1.

In the presence of a uniform perpendicular electric field, the site energy $V_{l,i}^{A,B}$ is constant within one layer, i.e., $V_{l,i}^{A,B} = V_l$. We introduce the potential average $V_{\mu} = (V_1 + V_2)/2$ and the potential difference $V_0 = (V_1 - V_2)/2$. The energy spectrum of the system has a direct band gap of the size $2|V_0|$ at the two inequivalent corners, K and K', of the Brillouin zone. In experiments, one can change both the Fermi energy (through V_{μ}) and the band gap (through V_0) at the same time by adjusting the gate voltages [107].

The pseudospin degree of freedom is defined as the electron population difference between the two layers. To find its explicit dependence on the bias voltage, we recast the Hamiltonian (5.5) in the momentum space and focus on the low-energy sector that governs the quasiparticle dynamics. The effective Hamiltonian around the K

point reads:

$$H = \begin{pmatrix} V_0 & v_F\pi^\dagger & 0 & 0 \\ v_F\pi & V_0 & t_\perp & 0 \\ 0 & t_\perp & -V_0 & v_F\pi^\dagger \\ 0 & 0 & v_F\pi & -V_0 \end{pmatrix}, \tag{5.6}$$

where $v_F = \frac{3}{2}at/\hbar$ with a being the lattice constant (we use units such that $\hbar = 1 = v_F$ from now on), and $\pi = p_x + ip_y$ is the momentum measured from the K point in the Brillouin zone. The Hamiltonian around the K' point can be obtained by replacing π with $p_x - ip_y$. We have dropped the V_μ term because it corresponds to a constant shift of all energy levels, or equivalently, a shift of the relative position of the Fermi energy E_F. For $|V_0| \ll t_\perp$, the Hamiltonian can be further reduced to [83],

$$H \simeq \begin{pmatrix} V_0 & (\pi^\dagger)^2/t_\perp \\ (\pi)^2/t_\perp & -V_0 \end{pmatrix}. \tag{5.7}$$

The resulting two-component wavefunctions describe the electronic amplitudes on A_1 and B_2 sites. For a given eigenstate Ψ with energy E, the pseudopsin is defined as

$$\langle\Psi|\boldsymbol{\sigma}|\Psi\rangle = \sqrt{1 - \left(\frac{V_0}{E}\right)^2}(\cos 2\theta_p\hat{x} + \sin 2\theta_p\hat{y}) + \frac{V_0}{E}\hat{z}, \tag{5.8}$$

where $\theta_p = \arctan(p_y/p_x)$. We can clearly see that the pseudospin can be tuned by the potential difference V_0.

5.3 Pseudospin Valve in Bilayer Graphene

The bulk pseudospin valve (PSV) proposed by San-Jose *et al.* [110] consists of a pair of adjacent gate electrodes with tunable bias voltage. When the two gates have the same (opposite) potential difference, the electrons in two gated region have parallel (antiparallel) pseudospins. In the antiparallel configuration the transmission rate

will be strongly suppressed because of the interface pseudospin flipping, while in the parallel configuration the pseudospin does not play a role. As a result, the system can be changed between the on and off states.

5.3.1 Edge effects

Next we consider the energy spectrum of the bilayer graphene system described by the Hamiltonian (5.5) in a confined geometry. In addition to the energy quantization, the most visible difference between the bulk and nanoribbon graphene systems is the appearance of the edge states [72, 115]. Shown in the inset of Fig. 5.3 is the energy spectrum of the bilayer graphene with zigzag edges. We can see that in addition to the two flat-band edge states, as usually seen in monolayer graphene, there are two more edge states with dispersive energy bands. In bilayer grapene, there are four different edges terminated by atoms of the type $A1$, $B1$, $A2$ and $B2$, respectively (Fig. 5.1). The two flat-band edge states are strictly localized on the edge atoms $A1$ and $B2$, separated by an energy gap of $2|V_0|$. On the other hand, due to the coupling $t_\perp$ between the two layers, the other two edge states (residing on the edges formed by atoms $B1$ and $A2$) are dispersive and can penetrate into the bulk [115]. Remarkably, the band structure of these edge states extend well into the bulk band gap ("midgap" region). Figure 5.3 shows the behavior of the small gap $2V_g$ between the dispersive edge states as a function of the nanoribbon width. It is clear that as the nanoribbon width increases, the dispersive edge states tend to extend to the whole midgap region and the energy spectrum becomes essentially gapless. This opens up the possibility of transport phenomena at an arbitrary Fermi energy.

The setup of the PSV is shown in Fig. 5.4, with a interface of length D connecting two semi-infinite gated regions. The transmission rate of electrons through the whole system is calculated using the standard recursive Green's function method [31], which is a widely used technic in the study of transport properties [101, 110, 121–131]. Within this approach, the system is sliced into a series of principal layers (Fig. 5.1),

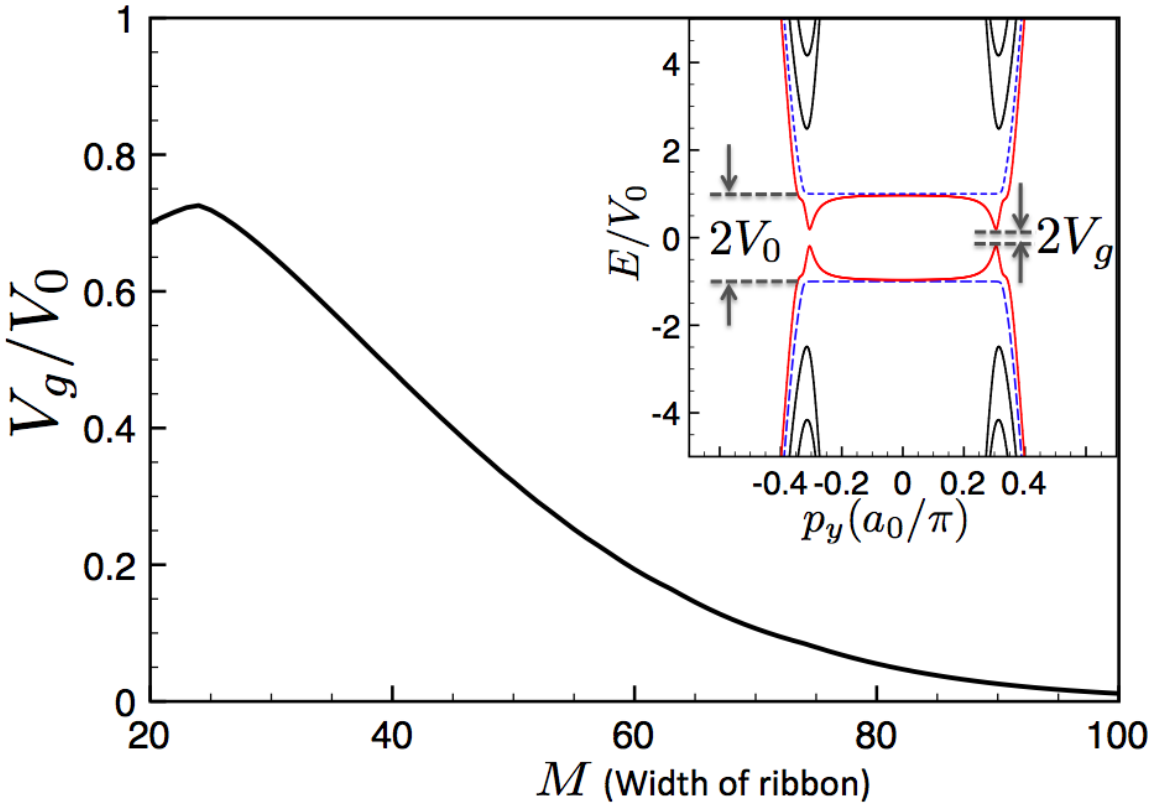

Figure 5.3: Energy gap between the dispersive edge states (red in the inset) in zigzag nanoribbons as a function of the nanoribbon width. Inset: spectrum of a zigzag nanoribbon with width $M = 60\, w_z$.

and then the Green function is calculated by propagating an initial function layer by layer from one end to the other. We use the algorithm developed by M. P. L. Sancho *et al.* [32] to mimic the semi-infinite leads by a finite region with a large number of principle layers. Finally, the conductance is calculated by the Landauer formula

$$G = \frac{2e^2}{h} T \ , \tag{5.9}$$

where T is the transmission rate obtained from the Green function. The factor of 2 comes from the electron spin degeneracy.

5.3.2 Conductance of bilayer nanoribbons

We first consider a bilayer graphene nanoribbon with an abrupt interface between the two gated regions. For antiparallel configuration, we have

$$V_0(x) = V_0[1 - 2\theta(x)] \ , \tag{5.10}$$

and for parallel configuration, $V_0(x)$ is a constant. The interface length $D = 0$.

The conductance of nanoribbons with armchair and zigzag edges is shown in Fig. 5.5. We immediately notice that, in sharp contrast to armchair edges, nanoribbons with zigzag edges have a finite conductance even when the Fermi energy is in the midgap region. Moreover, the conductance of the parallel and antiparallel configurations shows a sizable difference in this region, giving rise to a "midgap" PSV effect. To quantify the PSV effect, we define the pseudospin magnetoresistance (PMR) following Ref. [110]:

$$\text{PMR} = \frac{G_P - G_{AP}}{G_P}, \tag{5.11}$$

where $G_P(G_{AP})$ is the conductance for parallel (antiparallel) configuration. The PMR for both edges is shown in Fig. 5.6.

To understand the behavior of the PMR we have also plotted the corresponding band structure in Fig. 5.5. For the antiparallel configuration the translational symmetry along the nanoribbon direction is broken because of the interface. Nonetheless we can still consider the *local* band structure inside the semi-infinite leads far way from the interface. The band structures with opposite V_0 are exactly the same. For zigzag edges we only show one of the valleys because the intervalley scattering involves large momentum transfer and contributes little to the total conductance. By comparing the band structure of the zigzag and armchair nanoribbons, we can clearly see that the midgap PSV effect originates from the dispersive edge states discussed earlier. The efficiency of the midgap PSV is comparable to its bulk counterpart, with a fairly large PMR in the bulk band gap($>= 60\%$).

Several remarks are in order. (i) For parallel configurations, the conductance shows a steplike behavior as a function of the Fermi energy, typical for finite size system. On the other hand, for antiparallel configurations, the conductance varies much smoother, increasing gradually when the Fermi energy is between two subbands. This can be attributed to the fact that for a given energy band, the z-component of the pseudospin has its largest value at the band bottom then decreases as the energy increases [see Eq.(5.8)]. (ii) The largest difference between G_P and G_{AP} is $2G_0$ at the subband bottom. As both G_P and G_{AP} increases with Fermi energy, the peak value of PMR decreases. (iii) We note that for zigzag nanoribbons, there exists a region [the Δ region [113, 132] in Fig. 5.5(b)], where the PMR vanishes with equal G_P and G_{AP}. In this region, if the electrons are limited to one of the valleys then the backscattering is completely eliminated. The perfect transmission of the antiparallel configuration therefore indicates that the pseudospin flipping process happens at a much faster rate than the intervalley scattering. In other words, the electrons will experience a sudden pseudospin flipping without being scattered to the other valley.

Finally, to obtain a comprehensive picture of the conductance of edge states in the midgap region, we plot in Fig. 5.7 the Fermi energy dependence of PMR for a zigzag nanoribbon with its width varying from 20 to 100. We can see that compared to the

bulk PSV effect, in which the PMR is appreciable only in a small window of E_F, there is a wide parameter range where a large PMR can be archived for the midgap PSV effect.

5.3.3 Conductance with finite interface

Having demonstrated the midgap PSV effect for an ideal abrupt interface, next we discuss more realistic interface conditions. In a real experiment, the two external gates are usually separated by a certain distance and $V_0(x)$ should vary smoothly in space. Here, we consider a PSV with interface of length D. The origin of the x-axis is chosen at the middle. The on-site potential is constant in the lead region and modeled by the following function in the central region

$$V_1 = -V_2 = -V_0 \sin\left(\frac{\pi}{D}x\right) \tag{5.12}$$

for antiparallel configuration, and

$$V_1 = -V_2 = \frac{V_0 + V_m}{2} - \frac{V_0 - V_m}{2}\cos\left(\frac{2\pi}{D}x\right) \tag{5.13}$$

for parallel configuration, where V_1 (V_2) is on-site potential of top (bottom) layer, and $2V_m$ is the band gap minimum in the central region for the parallel configuration. Both potential profiles are shown in Fig. 5.4. Here the parameter V_m is included to account for the fact that there may be a region in the middle uncovered by both gate electrodes (Fig. 5.4). When $V_m = V_0$, we recover the ideal situation discussed by San-Jose *et al.* in bulk PSV [110]. However, as we will show later, a nonzero V_m can have a strong effect on the PMR.

In Fig. 5.8, we compare the conductance of the PSV with a smooth interface to an abrupt interface for both armchair and zigzag nanoribbons. We can see that the conductance with finite interface tends to surpress the PSV effect for both armchair and zigzag nanoribbons. The general cause has been discussed by San-Jose *et al.* [110]

in their bulk PSV study – with a large interface length D, electrons will have a long distance to adjust its pseudospin according to the profile of $V_0(x)$, and are able to pass through the interface by gradually accommodate the change instead of being reflected. Following this argument, we can see that the potential dip in the central region characterized by V_m can affect the conductance of parallel configuration. To understand this effect, let us consider an extreme case where $V_m = 0$. Then even in parallel configuration the pseudospin need to be quickly rotated to in-plane once the electrons are in the central region, because the pseudospin has no $\hat{z}$ component there. As a result, G_P is reduced and so does the PMR. There are, however, several additional features specific to the nanoribbon geometry. (i) The zero PMR region of the zigzag nanoribbons is unaffected at all, thanks to the absence of backscattering. (ii) The V_m term can significantly alter the edge state dispersion, therefore creating a large momentum mismatch at the interface. This cause the large drop of G_P in the midgap region, as seen in Fig. 5.8(b).

Due to the crucial role of V_m for parallel configuration, it is much desired to make the interface length D small enough to ensure that V_m is close to V_0.

5.3.4 Edge disorder

In this section, we study the influence of edge disorder on the midgap PSV effect. Previous studies have shown that in both monolayer and bilayer graphene the edge disorder will strongly affect the conductance of both zigzag and armchair nanoribbon [101, 126, 133]. In our calculation, we again consider an abrupt interface. The system consists of two clean, semi-infinite leads on the two sides and a central region of 40 principle layers where the disorder occurs. The interface is placed in the middle of the central region. In one principle layer, vacancies can appear at 4 available positions for zigzag nanoribbons and 8 available positions for armchair nanoribbons. In our tight-binding calculation the vacancy is simulated by setting the on-site energy to infinity.[124, 126, 134]

In Fig. 5.9, we show the comparison between a clean nanoribbon and one with edge disorder. For armchair nanoribbons, even a tiny amount of edge impurity (the impurity concentration $p = 2.5\%$) makes the PSV highly unreliable. This can be seen in Fig. 5.9(c); the PMR can drop to below 20% when the Fermi energy is in the first subband. On the other hand, for zigzag nanoribbons, even with a higher impurity concentration ($p = 10\%$) the PSV effect is pretty robust with PMR around or above 60% in a wide range when the Fermi energy is in the bulk band gap. This is due to the fact that the dispersive edge states in bilayer nanoribbon are non-localized and penetrates into the bulk, therefore it is less sensitive to the edge disorder. Experimentally, it has been found that [131] zigzag nanoribbons are more stable and easier to produce than armchair nanoribbons. All these evidences imply that the zigzag nanoribbon is a much better candidate than armchair nanoribbon for PSV application.

5.4 Summary

In summary, we have investigated the pseudospin valve (PSV) effect in bilayer graphene nanoribbons. We found the midgap PSV effect exists for nanoribbons with zigzag edges, in which the PSV can operate even when the Fermi energy is in the bulk band gap. Compared to its bulk counterpart, the midgap PSV has the advantage that it can be realized with a modest shifting of the Fermi energy while in the bulk PSV the Fermi energy must be shifted out of the band gap. In addition, the midgap PSV also has a wider operational range of the bias potential where a large on-off ratio can be consistently obtained. This effect is robust against edge disorder and the details of the interface potential, making it a promising method to control the current-conducting state in graphene-based circuits at the nanoscale.

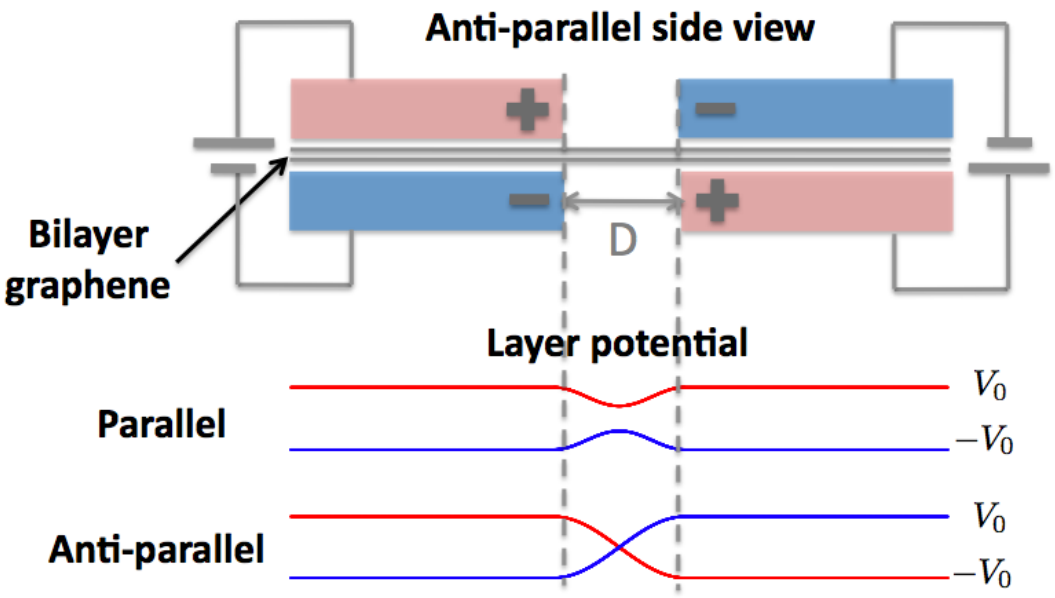

Figure 5.4: Electrode setup for antiparallel configuration and potential function of different configurations. The red (blue) line refers to top (bottom) layer potential.

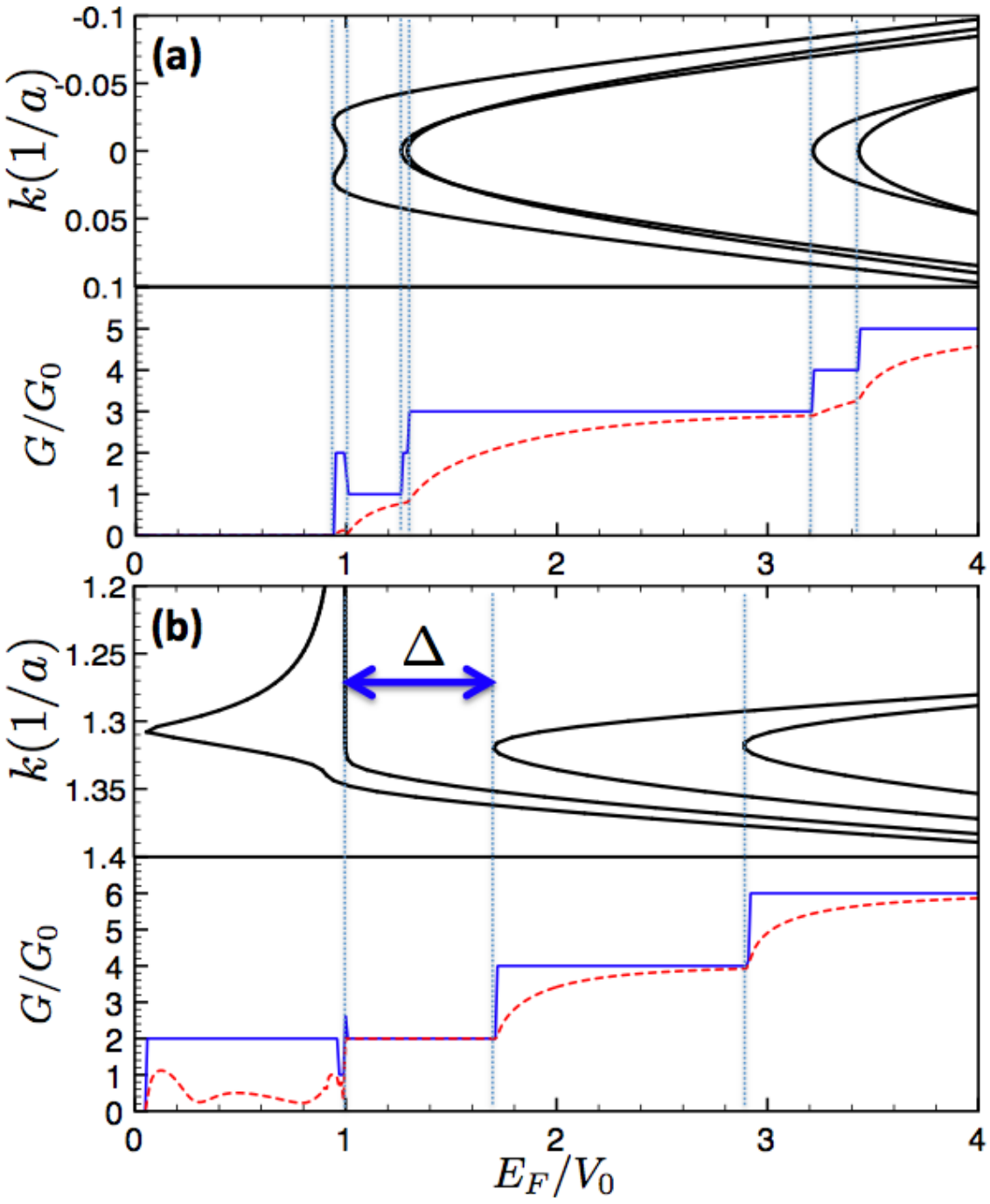

Figure 5.5: Band structures and conductance for bilayer graphene nanoribbons with (a) zigzag and (b) armchair edges. The width of both nanoribbons is $80\, w_{z/a}$. The blue solid line refers to parallel configuration, and the red dashed line refers to antiparallel configuration. $V_0 = 70$ meV is the potential difference between the layers. $G_0 = 2e^2/\hbar$ is the unit conductance.

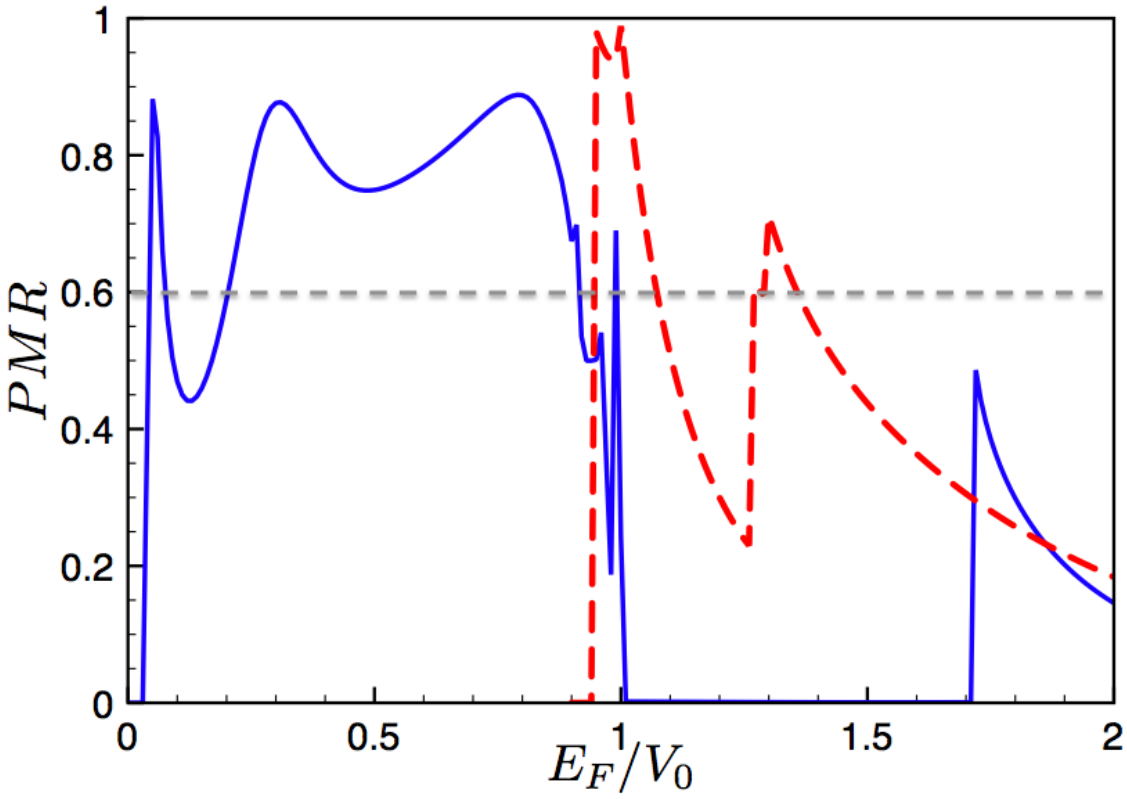

Figure 5.6: PMR for bilayer graphene nanoribbons with zigzag (blue solid) and armchair (red dashed) edges. The width of both nanoribbons is $80\, w_{z/a}$.

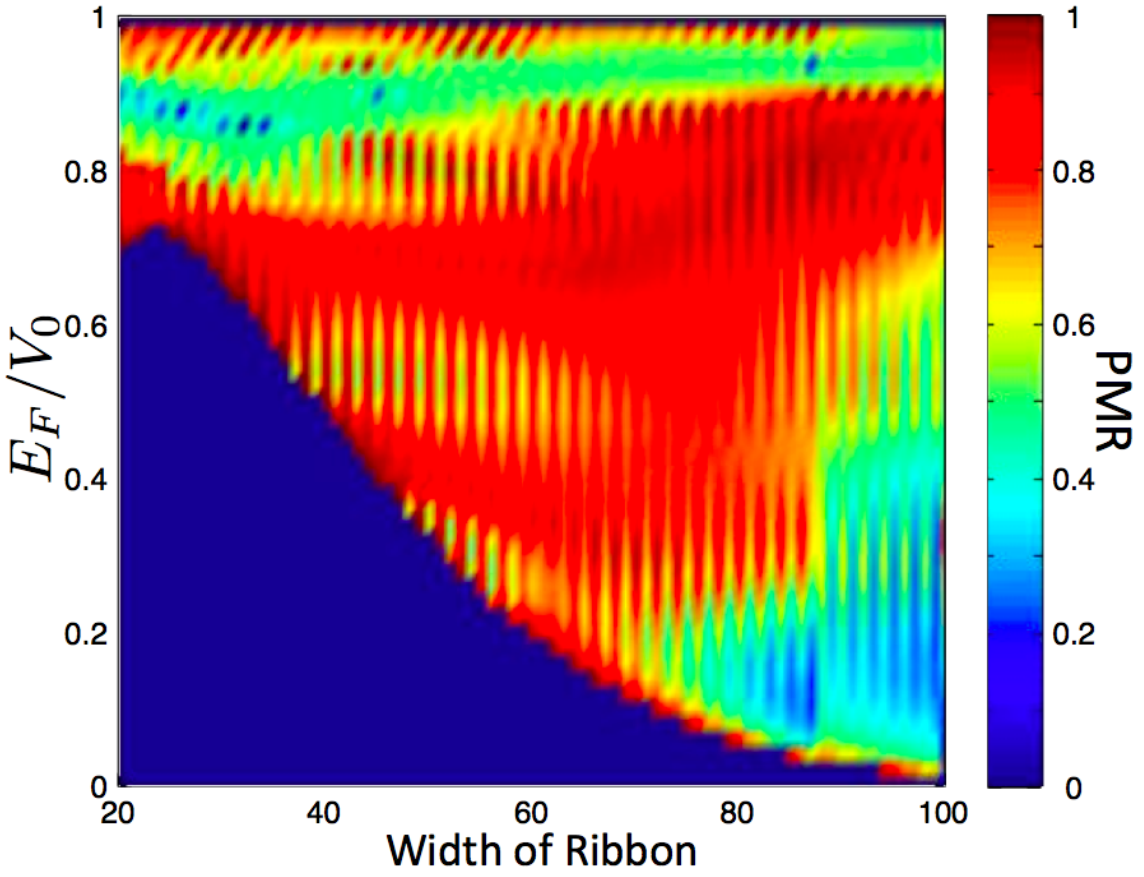

Figure 5.7: Fermi energy and width dependence of the PMR in zigzag nanoribbons.

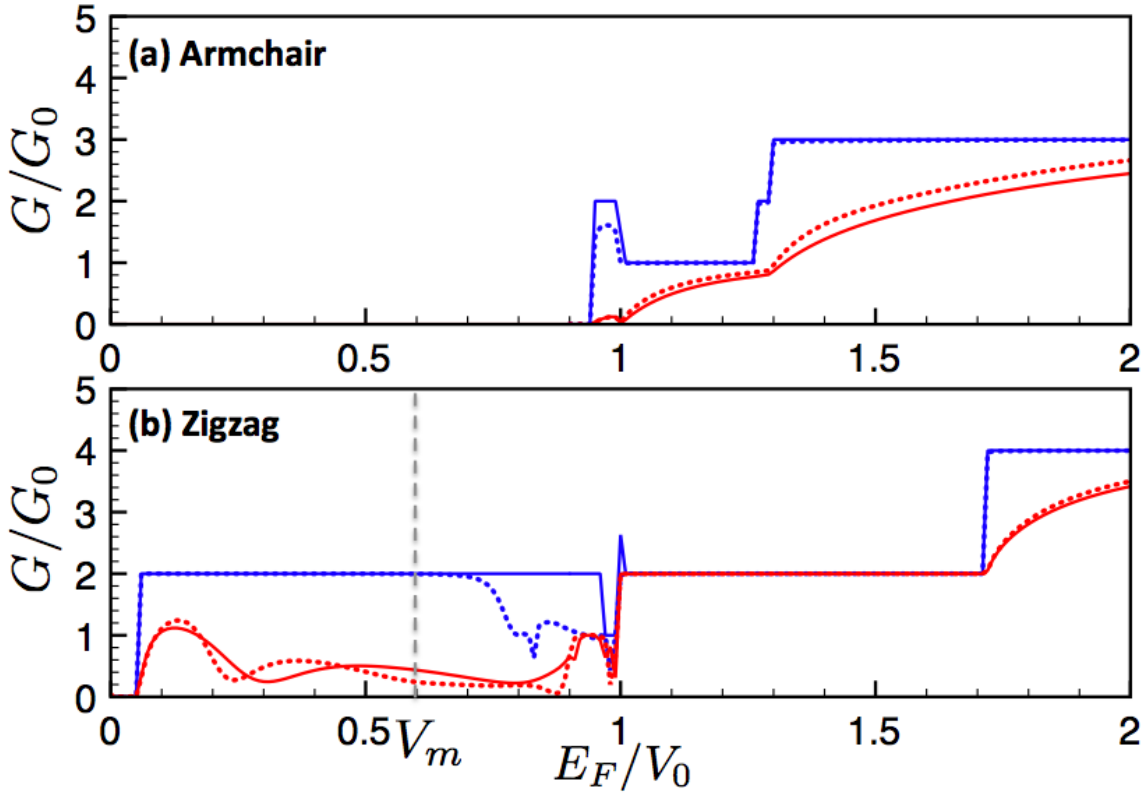

Figure 5.8: Conductance of (a) armchair ($N = 80\, w_a$) and (b) zigzag ($M = 80\, w_z$) nanoribbons. The solid lines refer to the ideal abrupt potential change on the interface. The dashed lines refer to the smooth potential change with interface length of $D = 5$ and $V_m = 0.6V_0$ for parallel configuration. Red (blue) lines refer to parallel (anti-parallel) configuration.

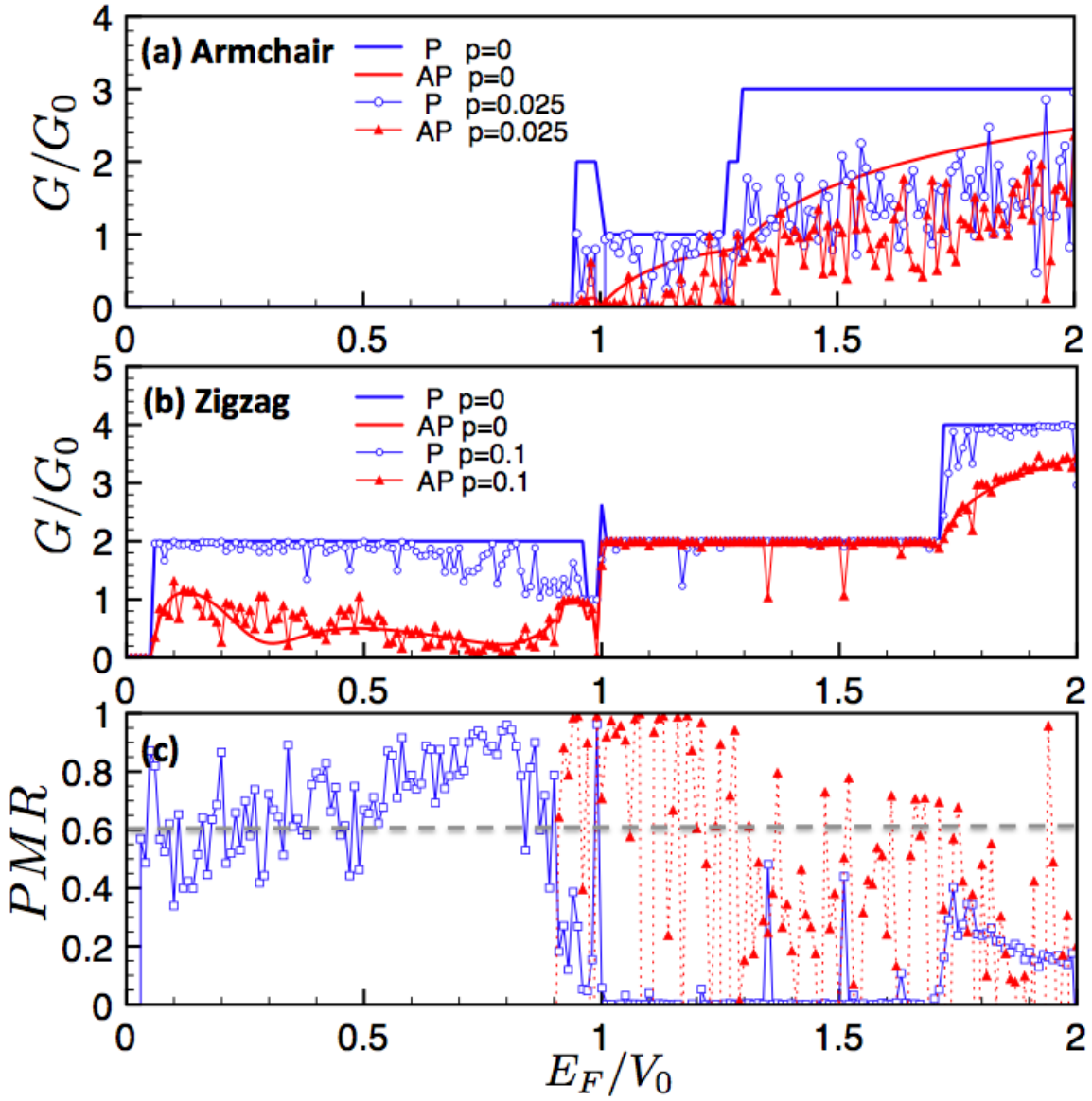

Figure 5.9: Conductance of (a) armchair ($N = 80\,w_a$) and (b) zigzag ($M = 80\,w_z$) nanoribbons with vacancies on the edge. The solid lines refer to conductance of perfect nanoribbons. The blue (red) line with hollow circle (filled triangle) refers to nanoribbons with vacancy density $p = 0.1$ in zigzag or $p = 0.025$ in armchair nanoribbons. In (c), the blue solid (red dashed) line with hollow square (filled triangle) refers to PMR result for zigzag (armchair) nanoribbons.

Chapter 6

Prospectives

Graphene is considered to be a very promising building block for future electronic devices [74]. To realize this potential, large-scale and high-quality graphene domains are required. One promising approach to achieve this requirement is the epitaxial growth [135–149] of graphene on metal substrates by chemical vapor deposition of hydrocarbons or surface segregation of carbon atoms from the bulk metal. However, in the end, to use the graphene as electronic devices, we have to transfer the epitaxially grown graphene from metal to other insulator substrates. Currently the only way to do that is to etch away the metal by some chemical solutions. The shortcomings are obvious: substrates can be used only once, unrecoverable and uncontrollable damage to graphene in the wet etching process, etc. Therefore, it is imperative to find sustainable alternative ways to detach graphene from metal substrates.

In connection with our previous studies of both metal nanostructures and graphene, our ongoing effort is to deal with the graphene-metal combined system. A natural prospective is to use the external electric field to fulfill the detachment of graphene and metal substrates. The interactions between graphene and metal substrates involve either Van der Waals force [150, 151] or chemical bonding [147]. The possibility to overcome the Van der Waals interaction has been shown in the graphite with electrostatic gates [152] or femtosecond laser pulses [153]. Using an

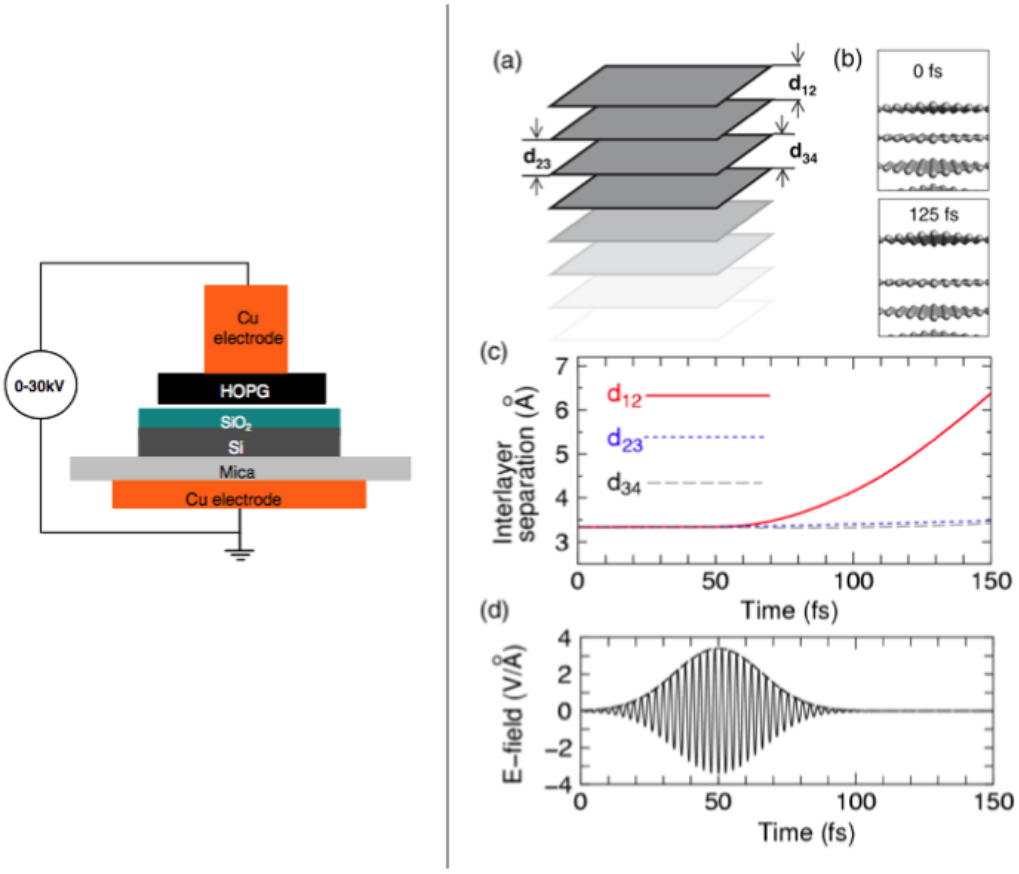

Figure 6.1: Left [152]: schematic of the experimental set-up for electrostatic deposition of graphene sheets, where HOPG stands for highly oriented pyrolytic graphite. Right [153]: schematic layer stacking (a) and structural snapshots (b) of the surface of AB-stacked graphite during exposure to a laser pulse with the full width at half maximum of 45 fs and a wavelength $\lambda = 800$ nm. (c) Time evolution of the interlayer distances. (d) Time-dependence of the optical electric field E characterizing the laser pulse.

experimental set-up as shown in Fig. 6.1, the authors can detach the graphene sheet with selective thickness from HOPG and transfer it to the silicon oxide substrate by tuning the strength of external voltage [152]. Figure 6.1 shows the process of the topmost graphene layer gradually moving away from graphite bulk under femtosecond laser pulse. However, this theoretical work shows that the thickness of the detached graphene depends on the full width at half maximum of laser pulse, i.e., the acting time of oscillating fields, rather than the strength of the external field in static case. This dissimilarity implies a quite different underlying physics between the static and dynamic responses of graphite systems.

The effect of external electric fields on a chemical bonding has also been studied for many systems. For example, Shea and Compton have shown that Ag^+ ions can be ejected from a roughened silver surface by laser light irradiation [154]. In this process, the surface plasmon excitation plays an important role, which can be seen from the kinetic-energy distribution of ejected ions shown in Fig. 6.2. The peak around 3.6 eV is due to the energy transfer from the excited surface plasmon to thermally liberated ions, which contribute to the low energy peak (< 0.5 eV). Ritchie *et al.* [155] have considered this surface plasmon assisted ions ejection as an inverse bremsstrahlung-type process (shown in Fig. 6.2), where an ion gains kinetic energy from the surface plasmon and momentum through a collision with the surface. Moreover, there is experimental work showing the effect of photoinduced nano-restructure [156–158], where the surface plasmon sometimes plays a crucial role [158].

The feasibility of our graphene detachment proposal can be clearly seen by noticing the similarity between graphene-metal systems and the previous studied systems. Comparing with graphite systems, it is desirable to use external fields to overcome the Van der Waals interaction in a weakly combining graphene-metal system, where the dynamic response of the system is expected to be more interesting due to the potential surface plasmon excitation at a metal substrate. Based on our studies shown in chapter 3 & 4, metal thin films would be the ideal substrates for the detaching purpose, since both the lifetime and frequency of their surface plasmons can be effectively tuned

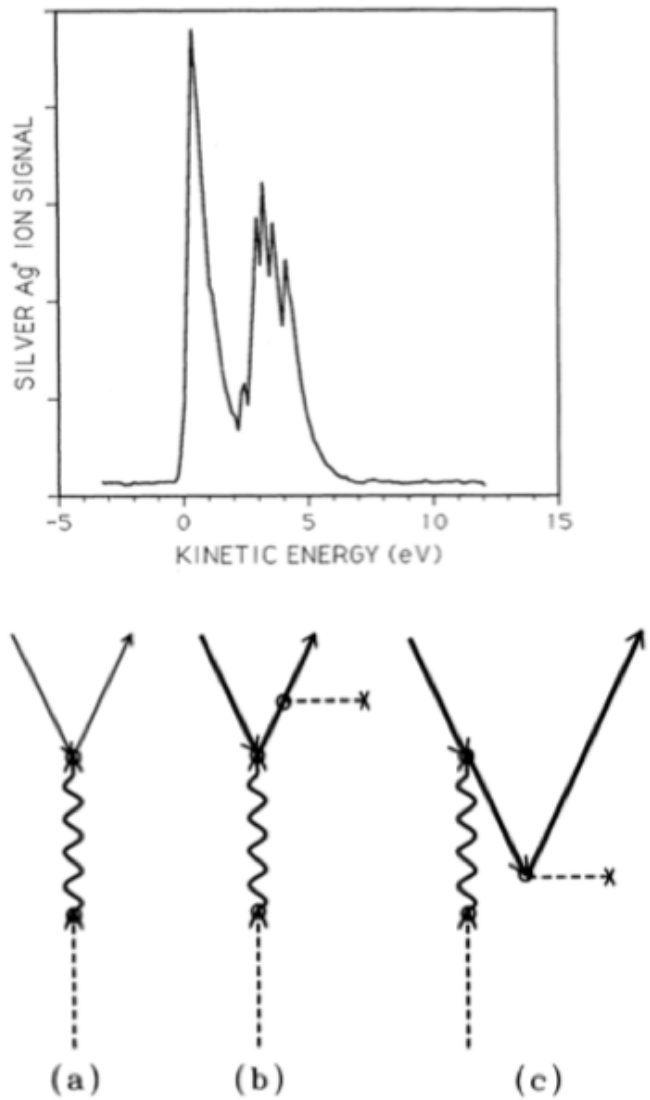

Figure 6.2: Upper [154]: the kinetic energy distribution of ejected Ag^+ ions. Lower [155]: the various surface plasmon decaying processes, where the surface plasmon (wavy line) is created from a photon (vertical dashed line). (a) The surface plasmon decays into a single electron-hole pair. (b) The surface plasmon decays through generation of an ion, which then collides with surface (horizontal dashed line) to obtain momentum. (c) The same final state but with time-reversed ordering of the plasmon-ion and the ion-surface interaction.

to meet different requirements. For more robust chemical bondings, the potential role of surface plasmons has been demonstrated for the single molecule detachment. The main issue for the graphene detachment is thus the multiple-bonding breaking of the whole flake. In the detaching process, one need to carefully deal with the energy cumulation at the graphene-metal interface without breaking the graphene intralayer carbon-carbon bonds.

Chapter 7

Conclusions

In this thesis, we investigated the transport and optical properties of a series of low-dimensional systems, which includes freestanding metal nanostructures, metal-semiconductor overlayers, semi-metal graphene nanoribbons, and graphene-metal systems.

Using the time dependent local density approximation, we have performed a comprehensive study of the energy and linewidth of plasmons in various quantum metal structures. We found that Landau damping, as the main dissipation channel in this regime, can be drastically tuned due to energy quantization of individual electron levels and e-h pairs. The generic oscillatory nature of the tunability is in stark contrast with the expectations of a semiclassical surface scattering picture. The use of an e-h pair basis also allows us to reveal the underlying physical origin for strong hybridization broadening of near degenerate plasmon modes. These findings are expected to guide future designs of plasmonic nanostructures of wide applicability.

Beyond the freestanding assumption of metal nanostructures, we have studied the various plasmon excitations in more realistic metal-semiconductor overlayers, where Mg thin films are grown on Si substrates with different thickness. We found that the observed plasmon peaks can be explained as the hybridization between multipole plasmon modes and the antisymmetric surface plasmon mode in thin films.

The symmetric surface plasmon mode missing in experiments can be theoretically observed at low energy region (< 3 eV) with very small energy weight. Both the experimental and theoretical studies indicate the coexistence of monopole surface plasmons, multipole surface plasmons and bulk plasmons, which is a clear signal for the existence of multi-plasmon modes.

In bilayer graphene nanoribbons, we have studied its transport properties in the mesoscopic regime. We found a midgap PSV effect exists for nanoribbons with zigzag edges, in which the PSV can operate even when the Fermi energy is in the bulk band gap. Compared to its bulk counterpart, the midgap PSV has the advantage that it can be realized with modest shifting of the Fermi energy while in the bulk PSV the Fermi energy must be shifted out of the band gap. In addition, the midgap PSV also has a wider operational range where a large on-off ratio can be consistently obtained. This effect is robust against edge disorder and the details of interface potential, making it a promising method to control the current-conducting state in graphene-based circuits at the nanoscale.

The study of graphene-metal systems is a natural perspective based on our efforts in both metal thin films and graphene systems. We expect to use a metal thin film as the substrate to grow graphene sheets, and then excite surface plasmons in the substrate to detach the graphene. The existing experimental and theoretical studies have shown that the surface plasmon can change both Van der Waals interactions and chemical bondings with proper setups, which reveals the feasibility of our proposal.

Appendixes

Appendix A

Units

A.1 Useful Constants

m_e	$9.1093826 \times 10^{-31}$ kg	
e	$1.60217653 \times 10^{19}$ C	
$1/(4\pi\epsilon_0)$	$8.9875517873681 \times 10^{9}$ kg $\cdot$ m$^3\cdot$ s$^{-2}\cdot$ C^{-2}	
c	2.99792458×10^{8} m $\cdot$ s^{-1}	
$\hbar$	$6.58211899 \times 10^{-16}$ eV $\cdot$ s	0.658 eV $\cdot$ fs
hc	$1.23984188 \times 10^{-6}$ eV $\cdot$ m	1240 eV $\cdot$ nm
$\hbar c$	$1.97326963 \times 10^{-7}$ eV $\cdot$ m	197 eV $\cdot$ nm
a_0	$5.2917720859 \times 10^{-11}$ m	0.0529 nm

A.2 Atomic Units

In atomic units, we have $m_e = \hbar = e = \dfrac{1}{4\pi\epsilon_0} = 1$

Energy	$Hartree$	27.211 eV
Time	$\hbar/Hartree$	0.02428884326505 fs
Momentum	$1/a_0$	1.88972613 Å^{-1}
Speed of light	137.036	

Appendix B

Density of States in Low-Dimensional Systems

The quantum size effect in low-dimensional systems can be visualized within a simple particle-in-box model. We consider that the free electron gas in a box is defined in the space region $0 \leq i \leq L_i$ with $i = x, y, z$ and the potential outside of the box is infinity. The discretized energy levels can then be written as

$$E_{l,m,n} = \frac{1}{2}\left(\frac{\pi l}{L_x}\right)^2 + \frac{1}{2}\left(\frac{\pi m}{L_y}\right)^2 + \frac{1}{2}\left(\frac{\pi n}{L_z}\right)^2, \tag{B.1}$$

where $l, m, n = 0, \pm 1, \pm 2, \ldots$. Now, supposing $L_x = L_y = L_z \gg 0$, the energy level can be viewed as continuous and the number of states with energy smaller than E in the unit volume is

$$n(E) = \frac{D_s}{L^3}\frac{4\pi}{3}(2E)^{3/2} / \left(\frac{\pi}{L}\right)^3 = \frac{(2E)^{3/2}}{6\pi^2} D_s, \tag{B.2}$$

where D_s is the spin degeneracy. The density of states at E is

$$\frac{dn(E)}{dE} = \frac{(2E)^{1/2}}{2\pi^2} D_s. \tag{B.3}$$

If we have the confinement in z direction, which means $L_x = L_y \gg L_z > 0$, the energy levels become discretized. The number of states and density of states now, respectively, are

$$n(E) = \sum_n \Theta(E - E_n) \frac{E - E_n}{2\pi} D_s \tag{B.4}$$

and

$$\frac{dn(E)}{dE} = \sum_n \frac{\Theta(E - E_n)}{2\pi} D_s, \tag{B.5}$$

where Θ is the Heavyside function. With additional confinement in y and x directions, we get the corresponding $1D$ and $0D$ results as

$$n(E) = \sum_{m,n} \Theta(E - E_{m,n}) \frac{\sqrt{2(E - E_{m,n})}}{\pi} D_s, \quad dn(E) = \sum_{m,n} \frac{\Theta(E - E_{m,n})}{\pi\sqrt{2(E - E_{m,n})}} D_s, \tag{B.6}$$

and

$$n(E) = \sum_{l,m,n} \Theta(E - E_{l,m,n}) D_s, \quad dn(E) = \sum_{l,m,n} \delta(E - E_{l,m,n}) D_s, \tag{B.7}$$

respectively.

Appendix C

Effective Potential in LDA Calculations

C.1 Hartree Potential

For the Hartree potential, we have the charge neutralization,

$$\int dr\rho(r) = \int dr\,[n(r) - n_b(r)] = 0. \tag{C.1}$$

For a nD structure with thickness dr' at r', the electric field E_{el} has the form

$$E_{el}(r) = \begin{cases} 0 & \text{if } r \leq r' \\ 4\pi\rho(r')dr'(\dfrac{r'}{r})^n & \text{if } r > r' \end{cases}, \tag{C.2}$$

and the potential induced at r is

$$V(r) = \int_{r_0}^{r} dr E_{el}(r) = 4\pi\rho(r')r'^n \int \frac{dr}{r^n}\,|_{r_0}^{r_>}, \tag{C.3}$$

where r_0 ($\gg r_2$) is the reference point. For $n = 0$, this is valid as long as we assume that there is another slab at $-r'$, and due to the charge neutralization of the system,

the total effect of the other slab will be cancelled. Finally, by applying the charge neutralization condition again, we integrate r' of Eq.(C.3) to get Eq.(3.47).

C.2 Exchange-Correlation Potential

The exchange correlation V_{xc} is expressed as,

$$V_{xc}(\mathbf{r}) = \frac{\delta E_{xc}[\rho]}{\delta \rho(\mathbf{r})}, \tag{C.4}$$

where

$$E_{xc} = E_x + E_c. \tag{C.5}$$

For Perdew-Zunger (PW correlation) LDA exchange-correlation, we have

$$\frac{\delta E_x[\rho]}{\delta \rho(\mathbf{r})} = A_x \frac{4}{3}\rho(\mathbf{r})^{1/3} = -\frac{3}{4\pi}(3\pi^2)^{1/3}\frac{4}{3}(\frac{3}{4\pi r_s^3})^{1/3} = -\frac{0.611}{r_s} \tag{C.6}$$

and

$$\frac{\delta E_c[\rho]}{\delta \rho(\mathbf{r})} = \frac{\delta(\rho(\mathbf{r})\epsilon_c[\rho])}{\delta \rho(\mathbf{r})} = \epsilon_c[\rho] + \rho(\mathbf{r})\frac{\delta \epsilon_c[\rho]}{\delta \mathbf{r}}\frac{\delta \mathbf{r}}{\delta \rho(\mathbf{r})} = \epsilon_c[\rho] - \frac{r_s}{3}\frac{\delta \epsilon_c[\rho]}{\delta \mathbf{r}}, \tag{C.7}$$

where

$$\epsilon_c[\rho] = -2c_0(1+\alpha_1 r_s)\ln\left[1 + \frac{1}{2c_0(\beta_1 r_s^{1/2} + \beta_2 r_s + \beta_3 r_s^{3/2} + \beta_4 r_s^2)}\right]. \tag{C.8}$$

The parameters are $c_0 = 0.031091$, $c_1 = 0.046644$, $\alpha_1 = 0.21370$, $\beta_1 = \frac{1}{2c_0}\exp(-\frac{c_1}{2c_0}) = 7.5957$, $\beta_2 = 2c_0\beta_1^2 = 3.5876$, $\beta_3 = 1.6382$, $\beta_4 = 0.49294$. In the end, we calculate the density derivative of the exchange-correlation potential as

$$\frac{\delta V_{xc}(\mathbf{r})}{\delta \rho(\mathbf{r})} = \frac{\delta V_{xc}(\mathbf{r})}{\delta \mathbf{r}}\frac{\delta \mathbf{r}}{\delta \rho(\mathbf{r})} = \left(\frac{0.611}{r_s^2} + \frac{2}{3}\frac{\delta \epsilon_c[\rho]}{\delta \mathbf{r}} - \frac{r_s}{3}\frac{\delta^2 \epsilon_c[\rho]}{\delta \mathbf{r}^2}\right)\left(-\frac{r_s}{3\rho(\mathbf{r})}\right). \tag{C.9}$$

Appendix D

Publications in High Energy Physics

In this appendix, I have attached my publications in high energy physics, which include:

[160] Ted Barnes, Xiaoguang Li, and Winston Robert, "*Meson emission model of* $\Psi \to N\bar{N}m$ *charmonium strong decays*", Phys. Rev. D 81, 034025 (2010). Copyright © American Physical Society, 2010

[161] Ted Barnes, Xiaoguang Li, and Winston Robert, "*Evidence for a* $J/\psi p\bar{p}$ *Pauli strong coupling?*", Phys. Rev. D 77, 056001 (2008). Copyright © American Physical Society, 2008

[162] Ted Barnes and Xiaoguang Li, "*Associated Charmonium Production in Low Energy* $p\bar{p}$ *Annihilation*", Phys. Rev. D 75, 054018 (2007). Copyright © American Physical Society, 2007

Associated charmonium production in low energy $p\bar{p}$ annihilation

T. Barnes[1,2,*] and X. Li[2,†]

[1]*Physics Division, Oak Ridge National Laboratory, Oak Ridge, Tennessee 37831, USA*
[2]*Department of Physics and Astronomy, University of Tennessee, Knoxville, Tennessee 37996, USA*
(Received 12 December 2006; published 15 March 2007)

The QCD mechanisms underlying the exclusive strong decays and hadronic production amplitudes of charmonium remain poorly understood, despite decades of study and an increasingly detailed body of experimental information. One set of hadronic channels of special interest are those that include baryon-antibaryon states. These are being investigated experimentally at BES and CLEO-c in terms of their baryon resonance content, and are also of interest for the future PANDA experiment, in which charmonium and charmonium hybrids will be produced in $p\bar{p}$ annihilation in association with light mesons. In this paper we develop a simple initial-state light meson emission model of the near-threshold associated charmonium production processes $p\bar{p} \to \pi^0\Psi$, and evaluate the differential and total cross sections for these reactions in this model. (Here we consider the states $\Psi = \eta_c, J/\psi, \psi', \chi_0$ and χ_1.) The predicted near-threshold cross section for $p\bar{p} \to \pi^0 J/\psi$ is found to be numerically similar to two previous theoretical estimates, and is roughly comparable to the (sparse) existing data for this process. The theoretical charmonium angular distributions predicted by this model are far from isotropic, which may be of interest for PANDA detector design studies.

DOI: 10.1103/PhysRevD.75.054018 PACS numbers: 11.80.−m, 13.60.Le, 13.75.Cs, 14.40.Gx

I. INTRODUCTION

Strong decays of charmonia through annihilation of the $c\bar{c}$ pair to light hadrons dominate the total widths of the lighter charmonium states [1]. In contrast to the faster open-charm decays, which appear to be reasonably well described by both the $^3P_0$ model [2] and the Cornell time-like vector decay model [3] (given the current state of the data), the $c\bar{c}$ annihilation decays are much less well understood. There are several general rules that appear to be respected by these decays; in particular, the number of QCD vertices in the leading-order Feynman diagram for annihilation into light quarks and gluons is a useful guide. For example, the $C = (+)$ charmonia that can annihilate at $O(g^2)$ (into gg for η_c, χ_0, χ_2, and gg for the χ_1) have strong annihilation widths of ~1–25 MeV, often much larger than the ~0.1–0.3 MeV widths of the $C = (-)$ states J/ψ and ψ', which must annihilate at $O(g^3)$ into ggg. Since $c\bar{c}$ annihilation is a short-ranged process (the charm quark propagator implies a range of $r \sim 1/m_c$), a strong suppression of annihilation widths with increasing orbital angular momentum $L_{c\bar{c}}$ is also anticipated; this suggests, for example, that the D-wave $c\bar{c}$ states $^1D_2$ and $^3D_2$, if below their DD^* open-charm threshold, will have strong widths of <1 MeV [3,4].

Although the inclusive annihilation decays are qualitatively understood in terms of $c\bar{c}$ annihilation into gluons, exclusive $c\bar{c}$ annihilation decays remain a mystery, despite the existence of considerable experimental information on the branching fractions of some $c\bar{c}$ states into specific exclusive modes. In particular, much is known about the exclusive two-body annihilation decays of the J/ψ and ψ', and a "12% rule" for the relative branching fractions of the ψ' and J/ψ into many of these modes is part of charmonium folklore. The recent increase in the number of modes studied, for example, by CLEO-c [5], has made it clear however that this rule is not generally applicable.

In this paper we note that there may be a simple relation between some two-body and three-body annihilation decays of charmonia, specifically in decays to the final states $p\bar{p}$ and $p\bar{p}\pi^0$. These decays are of interest both as a novel technique for studying N^* spectroscopy, for example, at BES [6–9] and because they can be used to estimate the cross sections for associated charmonium production in $p\bar{p}$ annihilation, as in $p\bar{p} \to \pi^0 + \Psi$ [10]. (We use Ψ to represent a generic charmonium state.) These cross sections are of particular interest in that they will be exploited by the PANDA project at GSI [11] to search for excited charmonia and charmonium hybrids. The scales of these cross sections are at present largely unknown; a better understanding of these associated charmonium production processes near threshold is obviously crucial for planning various aspects of this experiment, such as detector design and data acquisition.

II. THE MODEL

A. Motivation

Since strong decays to three-body final states are typically dominated by quasi-two-body transitions, one might anticipate that decays of the type $\Psi \to p\bar{p}\pi^0$ could be described as two-step processes, $\Psi \to (N^{*+}\bar{p} + \text{H.c.}) \to p\bar{p}\pi^0$, where the important N^* baryon isobars are those with large $N\pi$ couplings. Specifically we might expect the nucleon itself to make a large or perhaps dominant con-

*Electronic address: tbarnes@utk.edu
†Electronic address: xli22@utk.edu

tribution, in view of the large NNπ coupling. This in turn suggests that the associated production of a Ψ state and a pion in $p\bar{p}$ annihilation may take place through initial emission of a pion from the incoming p or $\bar{p}$ line, followed by direct annihilation of the $p\bar{p}$ state into $c\bar{c}$. At tree level this process is described by the two Feynman diagrams of Fig. 1.

The use of these simple hadron-level "pole" diagrams to describe these processes was previously suggested by Gaillard, Maiani and Petronzio [12], who considered the production of charmonium from $p\bar{p}$ states with specified initial quantum numbers in a PCAC model. Their work was subsequently extended analytically by Lundborg, Barnes and Wiedner [10] (much of Ref. [12] was numerical). Lundborg *et al.* also showed that a constant amplitude approximation could be used to estimate the cross section for $p\bar{p} \to \pi^0\Psi$ from the corresponding three-body decay $\Psi \to p\bar{p}\pi^0$; numerical results for $\sigma(p\bar{p} \to \pi^0 J/\psi)$ using both approaches are given in that reference.

The work presented here gives extensive analytic results for differential and total cross sections derived from the pole model, assuming plane wave initial $p\bar{p}$ states. If the partial width of a charmonium state Ψ to $p\bar{p}$ is known experimentally, one can use this to estimate the corresponding $\Psi - p\bar{p}$ coupling constant $g_{p\bar{p}\Psi}$. Since the NNπ coupling constant is known, one may then evaluate the differential and total cross sections for $p\bar{p} \to \pi^0\Psi$ both analytically and numerically in this model. Here we carry out this exercise for the cases of five low-lying Ψ states with known $p\bar{p}$ partial widths, specifically the η_c, J/ψ, ψ', χ_0 and χ_1.

B. Amplitudes

We describe the reactions $p\bar{p} \to \pi^0\Psi$ as two-step processes, initial pion emission from an incident proton or antiproton followed by direct annihilation of the proton-antiproton pair, $p\bar{p} \to \Psi$. This process at tree level is described by the two Feynman diagrams of Fig. 1. The $pp\pi^0$ and $\bar{p}\,\bar{p}\,\pi^0$ vertices are taken to be the usual $g_{pp\pi}\gamma_5$, and the $p\bar{p}\Psi$ vertex is generically $g_{p\bar{p}\Psi}\Gamma$, where the Dirac matrix Γ specifies the quantum numbers of the state Ψ. We use $\Gamma = \gamma_5$ for the η_c, $-i$ for the χ_0, $-i\gamma_\mu$ for the J/ψ and ψ', and $-i\gamma_\mu\gamma_5$ for the χ_1. For the vector and axial-vector cases J/ψ, ψ' and χ_1, Γ is implicitly contracted into the final Ψ polarization four-vector ϵ^*_μ. Of course in general one will have hadronic form factors at all these vertices, and more complicated Lorentz structures (such as $\sigma_{\mu\nu}q_\nu$ for the J/ψ) can be formed if one allows derivative couplings. As data from PANDA becomes available it will be of interest to consider these more general forms; for this first estimate we assume the simplest possible vertices, which are the minimal Dirac matrices times fixed coupling constants.

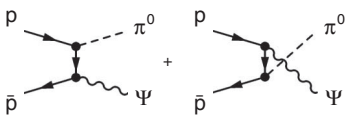

FIG. 1. Feynman diagrams assumed in this model of the generic reaction $p\bar{p} \to \pi^0\Psi$.

The invariant amplitude for $p\bar{p} \to \pi^0\Psi$ in this model is

$$\mathcal{M} = ig_\pi g_\Psi \bar{v}_{\bar{p}\bar{s}}\left[\Gamma\frac{(\not{p} - \not{k} + m)}{(t - m^2)}\gamma_5 + \gamma_5\frac{(\not{k} - \bar{\not{p}} + m)}{(u - m^2)}\Gamma\right]u_{ps}. \quad (1)$$

Here and in the following expressions m is the proton mass, m_π is the pion mass, M is the mass of the charmonium state Ψ, and $r_\pi = m_\pi/m$ and $r_\Psi = M/m$ are dimensionless mass ratios relative to the proton. The pion-nucleon coupling constant is $g_\pi \equiv g_{pp\pi}$, and the (state-dependent) charmonium-$p\bar{p}$ coupling constant is $g_\Psi \equiv g_{p\bar{p}\Psi}$. We also define squared strong coupling constants $\alpha_\pi \equiv g^2_{pp\pi}/4\pi$ and $\alpha_\Psi \equiv g^2_{p\bar{p}\Psi}/4\pi$.

It is sometimes useful to rewrite this invariant amplitude in an equivalent form that makes the overall $t \leftrightarrow u$ crossing symmetry more evident;

$$\mathcal{M} = -\frac{ig_\pi g_\Psi/2}{(t - m^2)(u - m^2)}\cdot[(s - M^2 - m_\pi^2)\bar{v}_{\bar{p}\bar{s}}\{\gamma_5\not{k}, \Gamma\}u_{ps} - (t - u)\bar{v}_{\bar{p}\bar{s}}[\gamma_5\not{k}, \Gamma]u_{ps}]. \quad (2)$$

Since the commutator (anticommutator) of $\gamma_5\not{k}$ with Γ vanishes for scalar (pseudoscalar) Ψ, this rearrangement simplifies the calculation considerably in these cases.

C. Massless pions

1. Differential cross sections

The differential and total cross sections we find given this invariant amplitude are rather simple in the massless pion limit, and only involve two independent functions. For this reason we first give results for massless pions, and then treat each set of charmonium quantum numbers separately for nonzero pion mass. Our results for the unpolarized differential cross sections in the massless pion limit are

$$\left\langle\frac{d\sigma}{dt}\right\rangle\Bigg|_{p\bar{p}\to\pi^0\eta_c} = \frac{\pi}{2}\frac{\alpha_\pi\alpha_\Psi}{s(s - 4m^2)}\frac{(x - y)^2}{xy}, \quad (3)$$

$$\left\langle\frac{d\sigma}{dt}\right\rangle\Bigg|_{p\bar{p}\to\pi^0\chi_0} = \frac{1}{2}\left\langle\frac{d\sigma}{dt}\right\rangle\Bigg|_{p\bar{p}\to\pi^0(J/\psi,\psi')} = \frac{\pi}{2}\frac{\alpha_\pi\alpha_\Psi}{s(s - 4m^2)}\frac{f^2}{xy}, \quad (4)$$

$$\left\langle \frac{d\sigma}{dt} \right\rangle \Big|_{p\bar{p}\to\pi^0\chi_1} = \pi \frac{\alpha_\pi \alpha_\Psi}{s(s-4m^2)} \cdot \left[(1 - 2/r_\Psi^2) \frac{f^2}{xy} + 2(r_\Psi^2 f - 1) \right]. \quad (5)$$

Here x and y are dimensionless, shifted Mandelstam variables $x \equiv t/m^2 - 1$ and $y \equiv u/m^2 - 1$, and f is a dimensionless energy variable, which for general masses is given by $f = (s - m_\pi^2 - M^2)/m^2 = -(x + y)$.

There are several interesting features in these angular distributions which are relevant to PANDA. Note that the differential cross sections in Eqs. (3)–(5) are $t \leftrightarrow u$ ($x \leftrightarrow y$) crossing symmetric, and that there are maxima in the forward and backwards directions, which give the largest values for the proton propagator functions $1/|t - m^2| = 1/m^2|x|$ and $1/|u - m^2| = 1/m^2|y|$. A more striking effect is the zero in the angular distribution of the final state $\pi^0\eta_c$, which follows from the odd $t \leftrightarrow u$ spatial symmetry of this amplitude; this implies a node at $t = u$, corresponding to $\theta = \pi/2$ in the *c.m.* frame. In comparison the angular distributions of the other final states we consider also have minima at $t = u$, but are nonzero there. These rapidly varying angular distribution could be used to test for the presence of this signal over the presumably more slowly varying backgrounds.

2. Total cross sections

In the massless pion limit the unpolarized total cross sections follow from integrating the results in Eqs. (3)–(5) over t. They may conveniently be written as functions of s and $\beta = \sqrt{1 - 4m^2/s}$ (the p or $\bar{p}$ velocity in the *c.m.* frame), and are given by

$$\langle\sigma\rangle|_{p\bar{p}\to\pi^0\eta_c} = 2\pi\alpha_\pi\alpha_\Psi \frac{(s - M^2)}{s^2\beta^2}[\tanh^{-1}\beta - \beta] \quad (6)$$

$$\langle\sigma\rangle|_{p\bar{p}\to\pi^0\chi_0} = 2\pi\alpha_\pi\alpha_\Psi \frac{(s - M^2)}{s^2\beta^2}\tanh^{-1}\beta \quad (7)$$

$$\langle\sigma\rangle|_{p\bar{p}\to\pi^0\chi_1} = 2\pi\alpha_\pi\alpha_\Psi \frac{(s - M^2)}{s^2\beta^2} \cdot [2(1 - 2/r_\Psi^2)\tanh^{-1}\beta + (s/M^2 - 2)\beta]. \quad (8)$$

The massless pion total cross section formulas for the final states $\pi^0 J/\psi$ and $\pi^0\psi'$ are proportional to the $\pi^0\chi_0$ result, as implied by Eq. (4); $\sigma(J/\psi) = \sigma(\psi') = 2\sigma(\chi_0)$. We stress that these simple ratios only apply to the algebraic expressions; the actual numerical cross sections are not simply related, due to a) different kinematics, and b) the strongly state-dependent $g_{p\bar{p}\Psi}$ couplings, which are given in Table I.

TABLE I. Charmonium-$p\bar{p}$ coupling constants, estimated from the measured branching fractions and total widths [1] and the $\Gamma_{\Psi\to p\bar{p}}$ width formulas of Eqs. (26)–(29) (see text).

State Ψ	$B_{\Psi\to p\bar{p}}$	$\Gamma_\Psi^{\text{tot.}}$ [MeV]	$10^3 \cdot g_{p\bar{p}\Psi}$
η_c	$(1.3 \pm 0.4) \cdot 10^{-3}$	25.5 ± 3.4	19.0 ± 3.2
J/ψ	$(2.17 \pm 0.08) \cdot 10^{-3}$	0.0934 ± 0.0021	1.62 ± 0.03
ψ'	$(2.65 \pm 0.22) \cdot 10^{-4}$	0.337 ± 0.013	0.97 ± 0.04
χ_0	$(2.24 \pm 0.27) \cdot 10^{-4}$	10.4 ± 0.7	5.42 ± 0.37
χ_1	$(6.7 \pm 0.5) \cdot 10^{-5}$	0.89 ± 0.05	1.03 ± 0.07
χ_2	$(6.6 \pm 0.5) \cdot 10^{-5}$	2.06 ± 0.12	...

D. Massive pions

1. Kinematics

The results given in the previous section for massless pions are attractive in their simplicity, and are useful for numerical estimates well above threshold. However we find that the angular distributions near threshold are strongly dependent on the pion mass (the massless case is a singular limit), and the difference in the location of the threshold for massless versus massive pions leads to numerically important differences in the predicted cross sections at energies relevant to PANDA. For these reasons we give detailed predictions for the differential and total cross sections for these charmonium production processes in the case of general pion mass.

Since we will discuss some angular distributions in the *c.m.* frame, it is useful to have the relation between Mandelstam variables and proton (p) and pion (k) variables in this frame for general masses. These relations are

$$E_p = \frac{s^{1/2}}{2} \quad (9)$$

$$p = \frac{s^{1/2}}{2}\left(1 - \frac{4m^2}{s}\right)^{1/2} \quad (10)$$

$$E_k = \frac{s^{1/2}}{2}\left(1 - \frac{(M^2 - m_\pi^2)}{s}\right) \quad (11)$$

$$k = \frac{s^{1/2}}{2}\left(1 - \frac{2(M^2 + m_\pi^2)}{s} + \frac{(M^2 - m_\pi^2)^2}{s^2}\right)^{1/2} \quad (12)$$

2. Differential cross sections

For general pion mass the differential cross sections $\{\langle d\sigma/dt\rangle\}$ may be written as multiplier functions $\{F_\Psi\}$ times the massless pion formulas of Eqs. (3)–(5). These functions, expressed as power series in $r_\pi = m_\pi/m$, are

$$F_{\eta_c} = 1 - \frac{r_\Psi^2}{xy} r_\pi^2 \quad (13)$$

$$F_{\chi_0} = 1 - \frac{(r_\Psi^2 - 4)}{xy} r_\pi^2 \tag{14}$$

$$F_{J/\psi,\psi'} = 1 + \left(\frac{2(r_\Psi^2 + f)}{f^2} - \frac{(r_\Psi^2 + 2)}{xy}\right) r_\pi^2 + \frac{2}{f^2} r_\pi^4. \tag{15}$$

In the χ_1 case it is simpler to give the full differential cross section with nonzero pion mass directly. This result is

$$\left\langle \frac{d\sigma}{dt} \right\rangle \Big|_{p\bar{p}\to\pi^0\chi_1} = \pi \frac{\alpha_\pi \alpha_\Psi}{s(s-4m^2)} \cdot \left\{ \left[2(f/r_\Psi^2 - 1) + \frac{(1 - 2/r_\Psi^2) f^2}{xy} \right] + \left[\frac{2}{r_\Psi^2} + \frac{2(r_\Psi^2 - f - 4)}{xy} - \frac{(r_\Psi^2 - 4) f^2}{(xy)^2} \right] r_\pi^2 - \frac{2}{xy} r_\pi^4 \right\}. \tag{16}$$

Examples of these angular distributions will be shown in the section on numerical results.

3. Total cross sections

In the case of general masses, inspection of the differential cross sections implied by Eqs. (3)–(5) and Eqs. (13)–(15) shows that the total cross sections may all be evaluated analytically in terms of integrals over x, which are generically of the form

$$\mathcal{I}_m = \int_{x_0}^{x_1} \frac{dx}{(xy)^m} \tag{17}$$

where $y = -x - f$. The limits of integration are implied by the definition $x = t/m^2 - 1$, and in terms of proton (p) and pion (k) *c.m.* frame energies and three-momenta are

$$x_{\substack{1\\0}} = (m_\pi^2 - 2E_p E_k \pm 2pk)/m^2. \tag{18}$$

These limits may also be written in terms of masses and the Mandelstam variable s, using the relations given in Eqs. (9)–(12). The explicit indefinite integrals required for our cross section calculations are

$$\mathcal{I}_0(x) = x \tag{19}$$

$$\mathcal{I}_1(x) = \frac{1}{f} \ln\left(\frac{x+f}{x}\right) \tag{20}$$

$$\mathcal{I}_2(x) = \frac{2}{f^3} \ln\left(\frac{x+f}{x}\right) - \frac{1}{f^2}\left(\frac{1}{x+f} + \frac{1}{x}\right). \tag{21}$$

In terms of these integrals, evaluated between the limits x_0 and x_1 (so that $\mathcal{I}_m \equiv \mathcal{I}_m(x_1) - \mathcal{I}_m(x_0)$), the total cross sections are

$$\langle\sigma\rangle_{p\bar{p}\to\pi^0\eta_c} = \frac{\pi\alpha_\pi\alpha_\Psi}{2} \frac{m^2}{s(s-4m^2)} \cdot [-(4\mathcal{I}_0 - f^2\mathcal{I}_1) + r_\pi^2 r_\Psi^2 (4\mathcal{I}_1 - f^2\mathcal{I}_2)] \tag{22}$$

$$\langle\sigma\rangle_{p\bar{p}\to\pi^0(J/\psi,\psi')} = \pi\alpha_\pi\alpha_\Psi \frac{m^2}{s(s-4m^2)} \cdot [f^2\mathcal{I}_1 + r_\pi^2(2(r_\Psi^2 + f)\mathcal{I}_1 - (r_\Psi^2 + 2)f^2\mathcal{I}_2) + r_\pi^4 2\mathcal{I}_1] \tag{23}$$

$$\langle\sigma\rangle_{p\bar{p}\to\pi^0\chi_0} = \frac{\pi\alpha_\pi\alpha_\Psi}{2} \frac{m^2 f^2}{s(s-4m^2)} [\mathcal{I}_1 - r_\pi^2(r_\Psi^2 - 4)\mathcal{I}_2] \tag{24}$$

$$\langle\sigma\rangle_{p\bar{p}\to\pi^0\chi_1} = \pi\alpha_\pi\alpha_\Psi \frac{m^2}{s(s-4m^2)} \cdot [(2(f/r_\Psi^2 - 1)\mathcal{I}_0 + f^2(1 - 2/r_\Psi^2)\mathcal{I}_1) + r_\pi^2(2/r_\Psi^2\mathcal{I}_0 + 2(r_\Psi^2 - f - 4)\mathcal{I}_1 - f^2(r_\Psi^2 - 4)\mathcal{I}_2) - r_\pi^4 2\mathcal{I}_1]. \tag{25}$$

These cross sections will be evaluated numerically in the next section.

III. NUMERICAL RESULTS

A. Estimating the $p\bar{p}\Psi$ coupling constants

Numerical evaluation of our predictions for cross sections and related quantities requires values for the model parameters. The hadron masses are of course well known, as is the NNπ coupling constant $g_\pi \equiv g_{pp\pi}$, which we take to be 13.5. The coupling strengths of the various charmonium resonances to $p\bar{p}$ however are not well established; this is a crucial issue for the PANDA project, which assumes that these couplings are sufficiently large to allow the accumulation of large charmonium event samples in $p\bar{p}$ annihilation.

Since the partial widths of several charmonium states to $p\bar{p}$ are now known experimentally, one may estimate these state-dependent charmonium-$p\bar{p}$ coupling constants $\{g_\Psi\}$ by equating the measured partial widths to the $O(g_\Psi^2)$ theoretical partial widths we calculate in our model, assuming the same pointlike $p\bar{p}\Psi$ vertices that we used to calculate the $p\bar{p} \to \pi^0\Psi$ cross sections. In terms of the $\alpha_\Psi = g_{p\bar{p}\Psi}^2/4\pi$ and the final p velocity $\beta = \sqrt{1 - 4m^2/M^2}$, these partial widths are

$$\Gamma(\eta_c \to p\bar{p}) = \alpha_{\eta_c}\beta M/2 \tag{26}$$

$$\Gamma(J/\psi \to p\bar{p}) = \alpha_{J/\psi}\beta(1 + 2/r_\Psi^2)M/3 \tag{27}$$

$$\Gamma(\chi_0 \to p\bar{p}) = \alpha_{\chi_0}\beta^3 M/2 \tag{28}$$

$$\Gamma(\chi_1 \to p\bar{p}) = \alpha_{\chi_1}\beta^3 M/3. \quad (29)$$

We use these relations and the measured branching fractions and total widths to estimate values for the various charmonium-$p\bar{p}$ coupling constants; these results are shown in Table I. Note that the couplings of the pseudoscalar and scalar states η_c and χ_0 to $p\bar{p}$ are an order of magnitude larger than the couplings of the vector and axial-vector states.

B. Total cross sections

We will now evaluate the total unpolarized cross sections $\langle\sigma\rangle(p\bar{p} \to \pi^0\Psi)$ for the five cases $\Psi = \eta_c, J/\psi, \chi_0, \chi_1$ and ψ', using the formulas given in Eqs. (22)–(25). The masses assumed are 2006 PDG values [1] rounded to 0.1 MeV; $m_{\pi^0} = 0.1350$ GeV, $m_p = 0.9383$ GeV, $M_{\eta_c} = 2.9804$ GeV, $M_{J/\psi} = 3.0969$ GeV, $M_{\chi_0} = 3.4148$ GeV, $M_{\chi_1} = 3.5107$ GeV and $M_{\psi'} = 3.6861$ GeV. The $pp\pi^0$ coupling constant is taken to be $g_\pi = 13.5$, and the $p\bar{p}\Psi$ couplings are given in Table I. The resulting cross sections are shown in Fig. 2. The E760 and E835 data for the $p\bar{p} \to \pi^0 J/\psi$ total cross section near 3.5 GeV (also shown in Fig. 2) suggest that our results overestimate this cross section at this E_{cm} by about a factor of 2.

Evidently these cross sections share a rapid rise above threshold, followed by a slowly varying "plateau" region above $E_{cm} \approx 4$ GeV. The most remarkable feature may be the wide variation in the plateau values with the charmonium state Ψ. The largest cross section by far is for η_c production, which is roughly a factor of 30 larger than the J/ψ cross section. Second is the χ_0 cross section, roughly 5 times larger than J/ψ. Since the χ_0 has a radiative branching fraction to $\gamma J/\psi$ of $35.6 \pm 1.9\%$, this implies

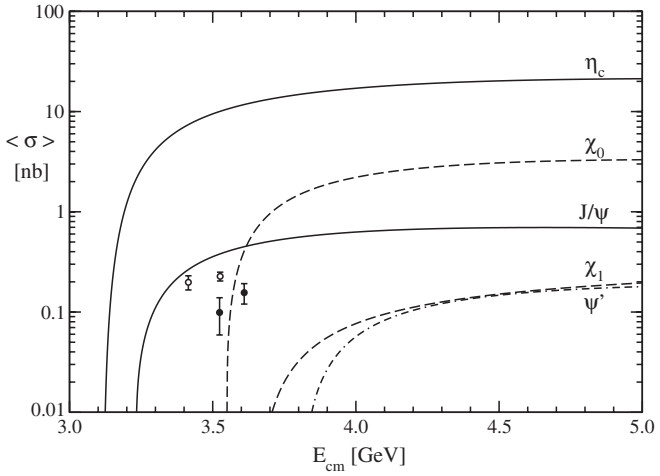

FIG. 2. Predicted unpolarized total cross sections for the processes $p\bar{p} \to \pi^0\Psi$, where $\Psi = \eta_c, J/\psi, \chi_0, \chi_1$ and ψ'. The data points are Fermilab measurements of the cross section for $p\bar{p} \to \pi^0 J/\psi$, from E760 [14] (filled) and E835 [15] (open). There are additional experimental results for this reaction from E835 [16] which have not yet been published as a physical cross section.

that J/ψ production through the radiative process $p\bar{p} \to \pi^0\chi_0$, $\chi_0 \to \gamma J/\psi$ is comparable to the direct process $p\bar{p} \to \pi^0 J/\psi$. Finally, the χ_1 and ψ' cross sections are smaller than the J/ψ by about a factor of 5–10. (For the ψ' to J/ψ ratio this is reminiscent of the 12% rule for a radial excitation.) These results suggest that the associated production of charmonium and charmonium hybrids with certain quantum numbers is strongly enhanced in $p\bar{p}$ production, and that $J^{PC} = 0^{-+}$ and 0^{++} states may be the most favored.

C. Angular distributions

The angular distributions predicted by this model of $p\bar{p} \to \pi^0\Psi$ are especially interesting, since they are far from isotropic and may be important for design of the PANDA detector. Two representative cases for $\langle d\sigma/d\Omega\rangle$ (*c.m.* frame) are shown in the figures; both show angular distributions normalized to unity in the forward direction, with E_{cm} in steps of 0.2 GeV up to a cutoff of $E_{cm} = 5.0$ GeV. The contours at $E_{cm} = 4.0$ GeV and $E_{cm} = 5.0$ GeV are highlighted.

The first angular distribution, in Fig. 3, shows the prediction of Eqs. (4) and (15) for the reaction $p\bar{p} \to \pi^0 J/\psi$. This distribution is isotropic as we approach threshold, but with increasing E_{cm} evidently becomes strongly forward- and backward-peaked. (All the unpolarized cross sections we consider are front-back symmetric.)

The second angular distribution is for the reaction $p\bar{p} \to \pi^0\eta_c$, which is predicted to be the largest associated charmonium production cross section by a considerable margin. This angular distribution, taken from Eqs. (3) and (13), is shown in Fig. 4. (The same conventions are used as in the previous figure.) This differential cross section shows a similar forward- and backward-peaking with increasing E_{cm}, and has in addition a very characteristic node at $t = u$, which is $\theta = 90^o$ in the *c.m.* frame. The large

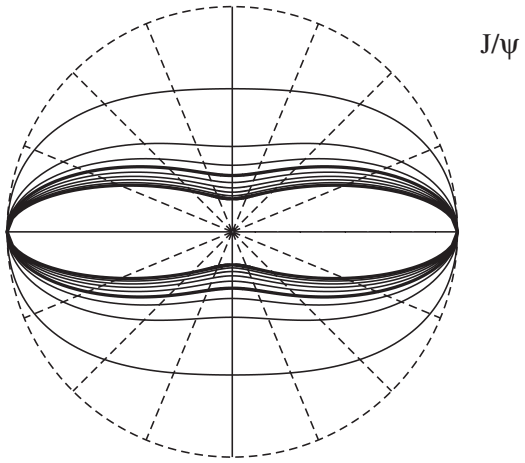

FIG. 3. Predicted *c.m.* frame unpolarized angular distribution $\langle d\sigma/d\Omega\rangle$ for the process $p\bar{p} \to \pi^0 J/\psi$, normalized to the forward intensity, for $E_{cm} = 3.4$–5.0 GeV in steps of 0.2 [GeV].

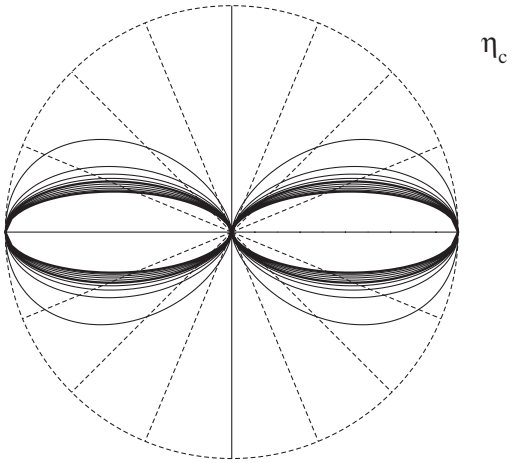

FIG. 4. The corresponding angular distribution for the reaction $p\bar{p} \to \pi^0 \eta_c$, for $E_{cm} = 3.2$–5.0 GeV in steps of 0.2 [GeV].

overall scale of this cross section suggests that the detection of unusual modes such as $p\bar{p} \to 4\gamma$ may be feasible (with both the π^0 and η_c decaying to $\gamma\gamma$).

IV. SUMMARY AND FUTURE

In this paper we have developed a hadronic pole model of charmonium production with an associated pion in proton-antiproton collisions. Given the Feynman diagrams of Fig. 1 we derived closed-form analytic results for the unpolarized differential and total cross sections for the processes $p\bar{p} \to \pi^0 \Psi$, where the quantum numbers considered for the charmonium state Ψ were 0^{-+}, 0^{++}, 1^{--} and 1^{++}. We quoted results for both massless and massive pions.

Besides the hadron masses this model has as free parameters the known $g_{pp\pi^0}$ and the coupling $g_{p\bar{p}\Psi}$ of the specified charmonium state Ψ to $p\bar{p}$. Here we used the experimental partial widths of light charmonium states to $p\bar{p}$ to estimate the coupling constants $\{g_{p\bar{p}\Psi}\}$. Given this information we numerically evaluated the differential and total cross sections for these reactions. In particular we gave numerical predictions for the total cross section for the cases $\Psi = \eta_c$, J/ψ, χ_0, χ_1 and ψ' (Fig. 2), and for the differential cross sections in two representative cases, $\Psi = J/\psi$ (Fig. 3) and η_c (Fig. 4).

The total cross sections predicted for the production of other charmonium states than the J/ψ are especially interesting. The reaction $p\bar{p} \to \pi^0 \eta_c$ is predicted to have the largest cross section by a considerable margin, followed by the χ_0. The two smallest cross sections are predicted for the χ_1 and ψ'. These results suggest that $J^{PC} = 0^{-+}$ and 0^{++} charmonium states may be the most copiously produced in the PANDA experiment. A comparison of the J/ψ and ψ' suggests that the first radial excitation cross sections are suppressed relative to the ground states by about a factor of 5–10 in the relevant PANDA energy regime.

Several future developments related to this type of model appear especially interesting. The important question of the size of the associated production cross sections of other charmonium states can be answered in this model given their $p\bar{p}$ branching fractions, so $B_{p\bar{p}}$ is a very important measurements for the charmonium states we have not considered here. Similarly, the cross sections for emission of a charmonium state Ψ accompanied by other light mesons $\{m\}$ can be studied; this may also be used to clarify poorly known ppm couplings. The importance of initial and final polarizations, which may be accessible at PANDA, can easily be addressed in this model. An important effect which has not been included is the contribution of intermediate N^* resonances to the $p\bar{p} \to \pi^0 \Psi$ transition amplitudes; the $NN^*\Psi$ couplings can be extracted from the corresponding $\Psi \to NN^*$ decays. It would also be of interest to determine the effect of replacing the pseudoscalar $pp\pi^0$ coupling we have assumed here by the axial-vector PCAC form, as this may significantly modify the predicted cross sections in the soft pion limit [13]. The large value of the coupling constant $g_{pp\pi}$ suggests that higher-order processes such as $p\bar{p} \to \pi\pi\Psi$ may be important in this model; this would also be an interesting calculation, and in the simple nucleon pole model requires no additional parameters. Finally, as our approximation of pointlike hadron vertices is unrealistic well above threshold, it would be very interesting to study the effect of plausible $pp\pi^0$ and $p\bar{p}\Psi$ form factors on our results.

ACKNOWLEDGMENTS

We are happy to acknowledge useful communications with D. Bettoni, C. Patrignani, T. Pedlar and K. Seth regarding experimental results for associated charmonium production cross sections at Fermilab, M. Pennington and W. Weise for discussions of PCAC, and W. Roberts for an independent check of the cross sections derived here. We also gratefully acknowledge support from K. Peters at GSI in Summer 2006, where this work was initiated. This research was supported in part by the U.S. National Science Foundation through grant No. NSF-PHY-0244786 at the University of Tennessee, and the U.S. Department of Energy under contract No. DE-AC05-00OR22725 at Oak Ridge National Laboratory.

[1] W.-M.Yao *et al.*, J. Phys. G **33**, 1 (2006).
[2] T. Barnes, S. Godfrey, and E. S. Swanson, Phys. Rev. D **72**, 054026 (2005).
[3] E. J. Eichten, K. Lane, and C. Quigg, Phys. Rev. D **69**,

094019 (2004).
[4] T. Barnes and S. Godfrey, Phys. Rev. D **69**, 054008 (2004).
[5] R. A. Briere *et al.* (CLEO-c Collaboration), Phys. Rev. Lett. **95**, 062001 (2005).
[6] J. Z. Bai *et al.* (BES Collaboration), Phys. Lett. B **510**, 75 (2001).
[7] M. Ablikim *et al.* (BES Collaboration), Phys. Rev. Lett. **97**, 062001 (2006).
[8] M. Ablikim *et al.* (BES Collaboration), Phys. Rev. D **71**, 072006 (2005).
[9] W. H. Liang, P. N. Shen, B. S. Zou, and A. Faessler, Eur. Phys. J. A **21**, 487 (2004).
[10] A. Lundborg, T. Barnes, and U. Wiedner, Phys. Rev. D **73**, 096003 (2006).
[11] Technical Progress Report for: P̄ANDA, Strong Interaction Studies with Antiprotons (Feb. 2005).
[12] M. K. Gaillard, L. Maiani, and R. Petronzio, Phys. Lett. B **110**, 489 (1982).
[13] W. Weise (private communication).
[14] T. A. Armstrong *et al.*, Phys. Rev. Lett. **69**, 2337 (1992).
[15] D. N. Joffe, hep-ex/0505007.
[16] M. Andreotti *et al.*, Phys. Rev. D **72**, 032001 (2005).

PHYSICAL REVIEW D **77,** 056001 (2008)

Evidence for a $J/\psi p\bar{p}$ Pauli strong coupling?

T. Barnes,[1,2,*] X. Li,[2,†] and W. Roberts[3,‡]

[1]*Physics Division, Oak Ridge National Laboratory, Oak Ridge, Tennessee 37831-6373, USA*
[2]*Department of Physics and Astronomy, University of Tennessee, Knoxville, Tennessee 37996-1200, USA*
[3]*Department of Physics and Astronomy, Florida State University, Tallahassee, Florida 32306-4350, USA*

(Received 2 January 2008; published 6 March 2008)

The couplings of charmonia and charmonium hybrids (generically Ψ) to $p\bar{p}$ are of great interest in view of future plans to study these states using an antiproton storage ring at GSI. These low to moderate energy $\Psi p\bar{p}$ couplings are not well understood theoretically, and currently must be determined from experiment. In this paper we note that the two independent Dirac (γ_μ) and Pauli ($\sigma_{\mu\nu}$) $p\bar{p}$ couplings of the J/ψ and ψ' can be constrained by the angular distribution of $e^+e^- \to (J/\psi, \psi') \to p\bar{p}$ on resonance. A comparison of our theoretical results to recent unpolarized data allows estimates of the $p\bar{p}$ couplings; in the better determined J/ψ case the data is inconsistent with a pure Dirac (γ_μ) coupling, and can be explained by the presence of a $\sigma_{\mu\nu}$ term. This Pauli coupling may significantly affect the cross section of the PANDA process $p\bar{p} \to \pi^0 J/\psi$ near threshold. There is a phase ambiguity that makes it impossible to uniquely determine the magnitudes and relative phase of the Dirac and Pauli couplings from the unpolarized angular distributions alone; we show in detail how this can be resolved through a study of the polarized reactions.

DOI: 10.1103/PhysRevD.77.056001 PACS numbers: 11.80.−m, 13.66.Bc, 13.88.+e, 14.40.Gx

I. INTRODUCTION

Charmonium is usually studied experimentally through e^+e^- annihilation or hadronic production, notably in $p\bar{p}$ annihilation. The $p\bar{p}$ annihilation process was employed by the fixed target experiments E760 and E835 at Fermilab, which despite small production cross sections succeeded in giving very accurate results for the masses and total widths of the narrow charmonium states J/ψ, ψ', χ_1, and χ_2. A future experimental program of charmonium and charmonium hybrid production using $p\bar{p}$ annihilation that is planned by the PANDA Collaboration [1] at GSI is one of the principal motivations for this study.

Obviously the strengths and detailed forms of the couplings of charmonium states to $p\bar{p}$ are crucial questions for any experimental program that uses $p\bar{p}$ annihilation to study charmonium; see, for example, the predictions for the associated production processes $p\bar{p} \to \pi^0\Psi$ in Refs. [2–4]. (We use Ψ to denote a generic charmonium or charmonium hybrid state, and ψ if the state has $J^{PC} = 1^{--}$.)

Unfortunately these low to moderate energy production reactions involve obscure and presumably rather complicated QCD processes, so for the present they are best inferred from experiment. In Ref. [4] we carried out this exercise by using the measured $p\bar{p}$ partial widths to estimate the coupling constants of the J/ψ, ψ', η_c, η_c', χ_0, and χ_1 to $p\bar{p}$, assuming that the simplest Dirac couplings were dominant. These $\Psi p\bar{p}$ couplings were then used in a PCAC-like model to give numerical predictions for several associated charmonium production cross sections of the type $p\bar{p} \to \pi^0\Psi$.

In this paper we generalize these results for the J/ψ and ψ' by relaxing the assumption of γ_μ dominance of the $\psi p\bar{p}$ vertex. We assume a $\psi p\bar{p}$ vertex with both Dirac (γ_μ) and Pauli ($\sigma_{\mu\nu}$) couplings, and derive the differential and total cross sections for $e^+e^- \to \psi \to p\bar{p}$ given this more general vertex. Both unpolarized and polarized processes are treated.

A comparison of our theoretical unpolarized angular distributions to recent experimental J/ψ results allows estimates of both the Dirac and Pauli $J/\psi p\bar{p}$ couplings. There is a phase ambiguity that precludes a precise determination of the (complex) ratio of the Pauli and Dirac $J/\psi p\bar{p}$ couplings from the unpolarized data; we shall see that an important interference effect between the Pauli and Dirac terms leads to a strong dependence of the unpolarized $p\bar{p} \to \pi^0 J/\psi$ cross section near threshold on the currently unknown phase between these terms.

Determining these couplings is evidently quite important for PANDA, and can be accomplished through studies of the polarized process $e^+e^- \to J/\psi \to p\bar{p}$. The angular distribution of the unpolarized, self-analyzing process $e^+e^- \to J/\psi \to \Lambda\bar{\Lambda}$ may also provide complementary information regarding the closely related $J/\psi\Lambda\bar{\Lambda}$ vertex. Both of these processes should be accessible at the upgraded BES-III facility.

II. UNPOLARIZED CROSS SECTION

The Feynman diagram used to model this process is shown in Fig. 1. We assume a vertex for the coupling of a generic 1^{--} vector charmonium state ψ to $p\bar{p}$ of the form

*tbarnes@utk.edu
†xli22@utk.edu
‡wroberts@fsu.edu

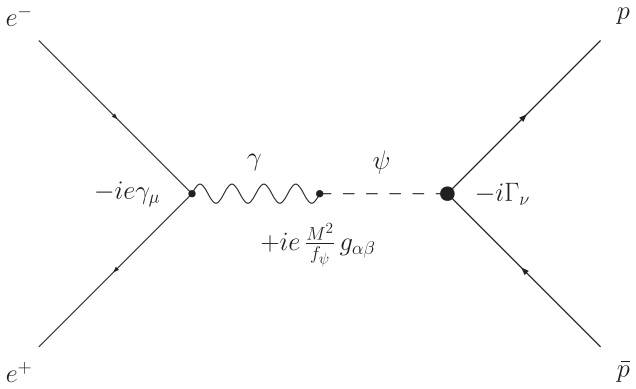

FIG. 1. The Feynman diagram assumed in this model of the generic reaction $e^+e^- \to \psi \to p\bar{p}$.

$$\Gamma_\mu^{(\psi p\bar{p})} = g\left(\gamma_\mu + \frac{i\kappa}{2m}\sigma_{\mu\nu}q_\nu\right). \quad (1)$$

In this paper m and M are the proton and charmonium mass, Γ is the charmonium total width, and we assume massless initial leptons. Following DIS conventions, q_ν is the four momentum transfer *from* the nucleon to the electron; thus in our reaction $e^+e^- \to p\bar{p}$ in the c.m. frame, we have $q = (-\sqrt{s}, \vec{0})$. The couplings g and κ are actually momentum-dependent form factors, but since we only access them very close to the kinematic point $q^2 = M^2$ in the reactions $e^+e^- \to (J/\psi, \psi') \to p\bar{p}$, we will treat them as constants.

The unpolarized differential and total cross sections for $e^+e^- \to \psi \to p\bar{p}$ may be expressed succinctly in terms of the strong $\psi p\bar{p}$ Sachs form factors $\mathcal{G}_E = g(1 + \kappa s/4m^2)$ and $\mathcal{G}_M = g(1 + \kappa)$. Both $\mathcal{G}_E$ and $\mathcal{G}_M$ are complex above $p\bar{p}$ threshold, in part because phases are induced by $p\bar{p}$ rescattering. If we assume that the lowest-order Feynman diagram of Fig. 1 is dominant, the phase of g itself is irrelevant, so here we take g to be real and positive. κ, however, has a nontrivial phase. We express this by introducing a Sachs form factor ratio, with magnitude $\rho \geq 0$ and phase χ;

$$\mathcal{G}_E/\mathcal{G}_M \equiv \rho e^{i\chi}. \quad (2)$$

The corresponding relation between the Pauli coupling constant κ and this Sachs form factor ratio is

$$\kappa \equiv |\kappa| e^{i\phi_\kappa} = \frac{\rho e^{i\chi} - 1}{(M^2/4m^2 - \rho e^{i\chi})}, \quad (3)$$

where we have assumed that we are on a narrow resonance, so we can replace s by M^2.

We will first consider the unpolarized process $e^+e^- \to \psi \to p\bar{p}$, and establish what the differential and total cross sections imply regarding the $\psi p\bar{p}$ vertex. The unpolarized total cross section predicted by Fig. 1 is

$$\langle\sigma\rangle = \frac{4\pi\alpha^2}{3f_\psi^2}\frac{M^4}{s^2}\frac{(1 - 4m^2/s)^{1/2}}{[(s - M^2)^2 + \Gamma^2M^2]} \times (2m^2|\mathcal{G}_E|^2 + s|\mathcal{G}_M|^2). \quad (4)$$

(We use angle brackets to denote a polarization averaged quantity.) Exactly on resonance (at $s = M^2$) this can be expressed in terms of the ψ partial widths

$$\Gamma_{\psi\to e^+e^-} = \frac{4\pi\alpha^2 M}{3f_\psi^2} \quad (5)$$

and

$$\Gamma_{\psi\to p\bar{p}} = \frac{(1 - 4m^2/M^2)^{1/2}}{12\pi M}(2m^2|\mathcal{G}_E|^2 + M^2|\mathcal{G}_M|^2), \quad (6)$$

which gives the familiar result

$$\langle\sigma\rangle|_{s=M^2} = \frac{12\pi}{M^2}B_{e^+e^-}B_{p\bar{p}}. \quad (7)$$

Here $B_{e^+e^-}$ and $B_{p\bar{p}}$ are the $\psi \to e^+e^-$ and $\psi \to p\bar{p}$ branching fractions.

Since the (unpolarized) $p\bar{p}$ width and total cross section on resonance involve only the single linear combination $(2m^2|\mathcal{G}_E|^2 + M^2|\mathcal{G}_M|^2)$, separating these two strong form factors requires additional information, such as the angular distribution. The unpolarized $e^+e^- \to \psi \to p\bar{p}$ differential cross section in the c.m. frame is given by

$$\left\langle\frac{d\sigma}{d\Omega}\right\rangle = \frac{\alpha^2}{4f_\psi^2}\frac{M^4}{s^2}\frac{(1 - 4m^2/s)^{1/2}}{[(s - M^2)^2 + \Gamma^2M^2]} \cdot [4m^2|\mathcal{G}_E|^2(1 - \mu^2) + s|\mathcal{G}_M|^2(1 + \mu^2)], \quad (8)$$

where $\mu = \cos(\theta_{c.m.})$. This angular distribution is often expressed as $1 + \alpha\mu^2$, where

$$\alpha = \frac{1 - (4m^2/s)|\mathcal{G}_E/\mathcal{G}_M|^2}{1 + (4m^2/s)|\mathcal{G}_E/\mathcal{G}_M|^2}. \quad (9)$$

Inspection of Eqs. (8) and (9) shows that one can determine the magnitude $\rho = |\mathcal{G}_E/\mathcal{G}_M|$ of the Sachs form factor ratio from the unpolarized differential cross section, but that the phase χ of $\mathcal{G}_E/\mathcal{G}_M$ is unconstrained.

The undetermined phase χ implies an unavoidable ambiguity in determining the magnitude and phase of the Dirac and Pauli $\psi p\bar{p}$ couplings g and κ from the unpolarized $e^+e^- \to (J/\psi, \psi') \to p\bar{p}$ angular distribution. We will discuss this ambiguity in the next section.

III. COMPARISON WITH EXPERIMENT

A. Summary of the data

Experimental values of α have been reported by several collaborations. The results for the J/ψ are [5–10]

$$\alpha = \begin{cases} 1.45 \pm 0.56, & \text{Mark I}[5] \\ 1.7 \pm 1.7, & \text{DASP}[6] \\ 0.61 \pm 0.23, & \text{Mark II}[7] \\ 0.56 \pm 0.14, & \text{Mark III}[8] \\ 0.62 \pm 0.11, & \text{DM2}[9] \\ 0.676 \pm 0.036 \pm 0.042, & \text{BES}[10]. \end{cases} \quad (10)$$

and for the ψ' [11,12]

$$\alpha = \begin{cases} 0.67 \pm 0.15 \pm 0.04, & \text{E835}[11] \\ 0.85 \pm 0.24 \pm 0.04, & \text{BES}[12]. \end{cases} \quad (11)$$

For our comparison with experiment we use the statistically most accurate measurement for each charmonium state, and combine the errors in quadrature. This gives experimental estimates for α of 0.676 ± 0.055 and 0.67 ± 0.155 for the J/ψ and ψ', respectively.

B. Testing the pure Dirac hypothesis

We first examine these experimental numbers using the "null hypothesis" of no Pauli term, $\kappa = 0$, in which case $\alpha = (1 - r)/(1 + r)$, where $r = 4m^2/M^2$. This $\kappa = 0$ formula was previously given by Claudson, Glashow, and Wise [13] and by Carimalo [14]; the value of α under various theoretical assumptions has been discussed by these references and by Brodsky and LePage [15], who predicted $\alpha = 1$. Figure 2 shows these two experimental values together with the pure Dirac (γ_μ) formula for α. The ψ' case is evidently consistent with a Dirac (γ_μ) $\psi' p\bar{p}$ coupling at present accuracy, but the better determined J/ψ angular distribution is inconsistent with a pure Dirac $J/\psi p\bar{p}$ coupling at the 4σ level.

The discrepancy evident in Fig. 2 may imply the presence of a Pauli term $(\kappa \neq 0)$ in the $J/\psi p\bar{p}$ vertex. Inspection of our result for α in the general case [Eq. (9)] shows that one can certainly accommodate this discrepancy by introducing a Pauli term.

C. Determining $\rho = |G_E/G_M|$ from α

The dependence of the predicted α on ρ at the J/ψ mass [from Eq. (9)] is shown in Fig. 3. The experimental value $\alpha = 0.676 \pm 0.055$ (shown) is consistent with the Sachs form factor magnitude ratio of

$$\rho = |G_E/G_M| = 0.726 \pm 0.074. \quad (12)$$

In terms of ρ and χ this completes our discussion: Given the unpolarized angular distribution, one obtains a result for $\rho = |G_E/G_M|$ from Eq. (9), but the phase χ of G_E/G_M is undetermined. However, one may ask the more fundamental question of what values of the Dirac and Pauli coupling constants g and κ in Eq. (1) are consistent with a given experimental unpolarized angular distribution.

D. Determining κ

First we consider the experimentally allowed values of κ. The unpolarized angular distribution provides us with a range of values of ρ [Eq. (12)], but χ is unconstrained; we may combine this information through Eq. (3) to determine the locus of allowed (complex) values of κ. This is shown in Fig. 4.

For $\chi = 0$, Eq. (3) implies that κ is real and negative, and takes on the smallest allowed magnitude. As we increase χ from 0, the allowed κ values proceed clockwise, since κ initially acquires a negative imaginary part. The extreme values of κ on the real axis in Fig. 4 are for $\chi = 0$, π, and are

$$\kappa = \begin{cases} -0.137 \pm 0.032, & \chi = 0 \\ -0.500 \pm 0.011, & \chi = \pi. \end{cases} \quad (13)$$

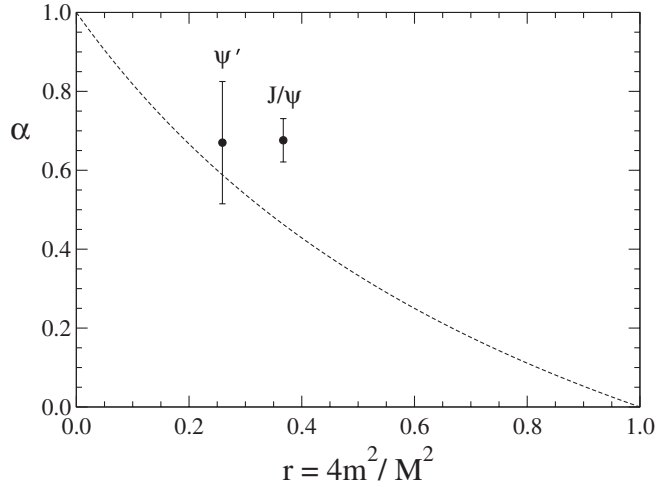

FIG. 2. The coefficient α observed in the unpolarized $e^+e^- \to (J/\psi, \psi') \to p\bar{p}$ angular distributions, together with the theoretical result $\alpha = (1 - r)/(1 + r)$ predicted by a pure Dirac (γ_μ) $\psi p\bar{p}$ coupling.

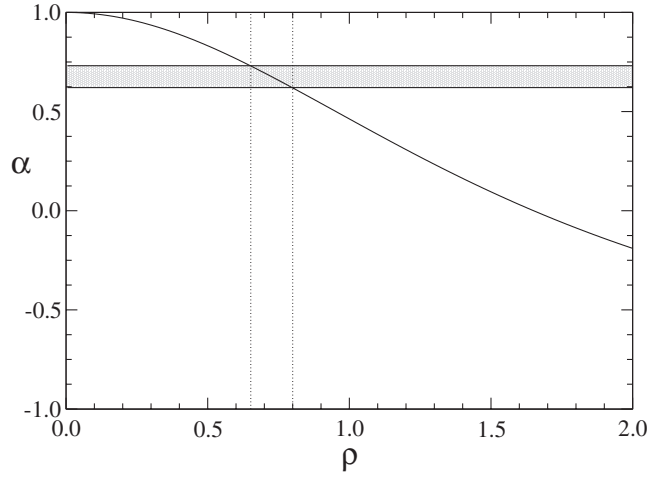

FIG. 3. The experimental value of the unpolarized $e^+e^- \to J/\psi \to p\bar{p}$ angular coefficient, $\alpha = 0.676 \pm 0.055$ (shaded), and the resulting Sachs $J/\psi p\bar{p}$ strong form factor magnitude ratio $\rho = |G_E/G_M|$ [Eq. (12)].

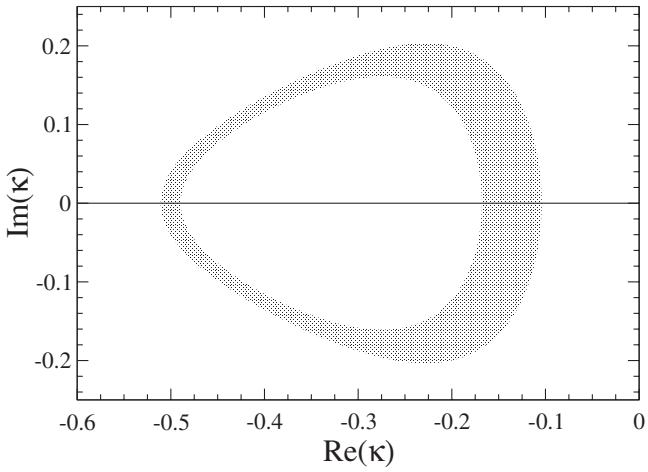

FIG. 4. The locus of complex κ (the $J/\psi p\bar{p}$ Pauli coupling) allowed by the experimental constraint $\rho = 0.726 \pm 0.074$, taken from the unpolarized differential cross section for $e^+e^- \to J/\psi \to p\bar{p}$.

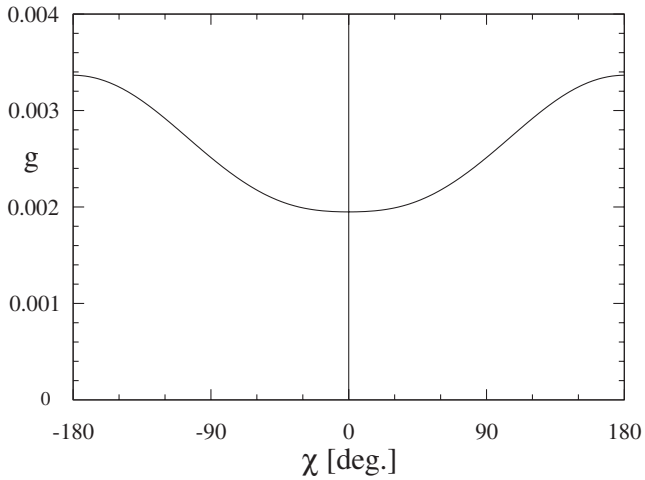

FIG. 5. The value of the overall $J/\psi p\bar{p}$ vertex strength g implied by the experimental $\Gamma_{J/\psi\to p\bar{p}}$ and ρ as a function of the unknown $J/\psi p\bar{p}$ Sachs phase χ.

E. Determining g

Next we consider the determination of the overall $J/\psi \to p\bar{p}$ vertex strength g. Since the differential and total cross sections for $e^+e^- \to J/\psi \to p\bar{p}$ only involve g through the ratio g/f_ψ, we must introduce additional experimental data to constrain g. The partial width for $J/\psi \to p\bar{p}$ is especially convenient in this regard, since it only involves the strong $J/\psi p\bar{p}$ vertex, and thus depends only on g and κ (and kinematic factors). This partial width was given in terms of the strong Sachs form factors in Eq. (6); as a function of g and κ it is

$$\Gamma_{\psi\to p\bar{p}} = \frac{1}{3}\frac{g^2}{4\pi} M\sqrt{1-r}\left[1 + \frac{r}{2} + 3\Re(\kappa) + \left(1 + \frac{1}{2r}\right)|\kappa|^2\right]. \tag{14}$$

This generalizes the $\kappa = 0$ result given in Eq. (27) of Ref. [4] to a nonzero Pauli coupling. Using the PDG values [16] of $\Gamma_{J/\psi} = 93.4 \pm 2.1$ keV and $B_{J/\psi\to p\bar{p}} = (2.17 \pm 0.07)\cdot 10^{-3}$, Eq. (14) implies a range of values of the overall vertex strength g for each value of the (unknown) phase χ. This is shown in Fig. 5. There is a range of uncertainty in g at each χ (not shown in the figure), due to the experimental errors in $\Gamma_{J/\psi}$, $B_{J/\psi\to p\bar{p}}$, and ρ, which is at most $\sim \pm 5\%$.

Note that g is bounded by the limits at $\chi = 0$ and π, for which $g \approx 2.0\cdot 10^{-3}$ and $\approx 3.4\cdot 10^{-3}$, respectively. The allowed values of g are somewhat larger than our previous estimate of $g = (1.62 \pm 0.03)\cdot 10^{-3}$ [4] assuming only a Dirac $J/\psi p\bar{p}$ coupling, as a result of destructive interference between the Pauli and Dirac terms.

IV. EFFECT ON $\sigma(p\bar{p} \to \pi^0 J/\psi)$

The effect of a $J/\psi p\bar{p}$ Pauli term on the $p\bar{p} \to \pi^0 J/\psi$ cross section may be of considerable interest for the PANDA project, since one might use this as a "calibration" reaction for associated charmonium production, and the Pauli term may be numerically important. (We note in passing that intermediate N* contributions may also be important in this and related processes [4] and should be considered in the future.) Although we have carried out this calculation with the vertex of Eq. (1) for general masses, the full result is rather complicated; here for illustration we discuss the much simpler massless pion limit.

For a massless pion the ratio of the unpolarized cross section $\langle\sigma(p\bar{p} \to \pi^0 J/\psi)\rangle$ with a Pauli term to the pure Dirac result (γ_μ only, denoted by D) is

$$\left.\frac{\langle\sigma(p\bar{p} \to \pi^0 J/\psi)\rangle}{\langle\sigma(p\bar{p} \to \pi^0 J/\psi)\rangle_D}\right|_{m_\pi=0} = \left[1 + 2\Re(\kappa) + \left(\frac{1}{2} + \frac{M^2}{8m^2}\right)|\kappa|^2 + \frac{(s-M^2)}{4m^2}\frac{\beta}{\ln[(1+\beta)/(1-\beta)]}|\kappa|^2\right], \tag{15}$$

where $\beta = \sqrt{1-4m^2/s}$ is the velocity of the annihilating p and $\bar{p}$ in the c.m. frame. The limit of this cross section ratio at threshold is shown in Fig. 6 for a range of complex κ.

Evidently there is destructive interference for a κ with a dominant negative real part, as is suggested by the unpolarized data. For the value $\kappa = -0.50$ [the larger solution in Eq. (13)] there is roughly a factor of 2 suppression in the cross section over the prediction for a pure Dirac coupling. The suppression, however, depends strongly on the phase of κ, and for imaginary κ has become a moderate enhancement. Thus, the near-threshold cross section for

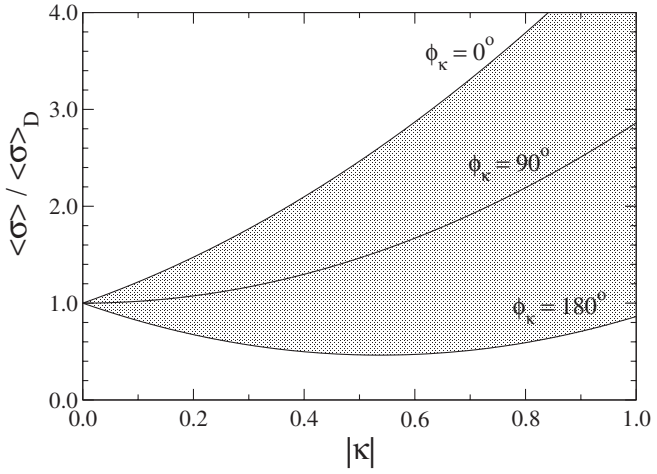

FIG. 6. The dependence of the unpolarized, near-threshold cross section $\langle\sigma(p\bar{p} \to \pi^0 J/\psi)\rangle$ on the (complex) Pauli coupling $\kappa = |\kappa| e^{i\phi_\kappa}$ [from Eq. (15)].

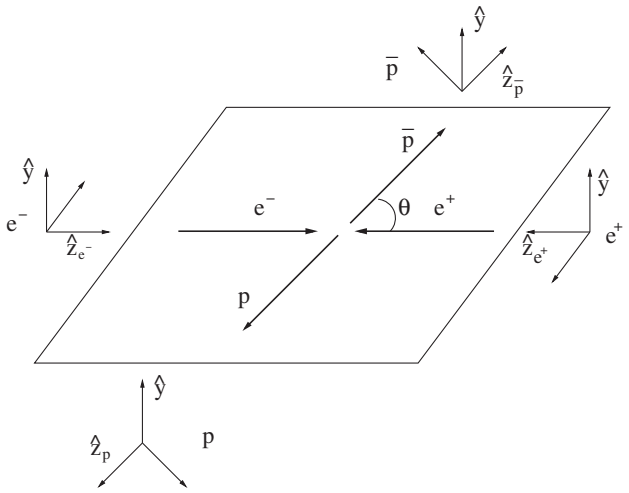

FIG. 7. Axes used to define the polarization observables.

$p\bar{p} \to \pi^0 J/\psi$ is quite sensitive to the strength and phase of the Pauli coupling; it will therefore be important for PANDA to have an accurate estimate of this quantity. In the next section we will show how both the magnitude and phase of κ can be determined in polarized $e^+e^- \to J/\psi \to p\bar{p}$ scattering, and may be accessible at BES.

V. POLARIZATION OBSERVABLES

The relative phase χ of the $J/\psi p\bar{p}$ Sachs strong form factors $\mathcal{G}_E$ and $\mathcal{G}_M$ may be determined experimentally through a study of the polarized process $e^+e^- \to J/\psi \to p\bar{p}$. As each of the external particles in this reaction has two possible helicity states, there are 16 helicity amplitudes in total. All the helicity amplitudes to the final $p\bar{p}$ helicity states $|p(\pm)\bar{p}(\pm)\rangle$ are proportional to $\mathcal{G}_E$, and all to $|p(\pm)\bar{p}(\mp)\rangle$ are proportional to $\mathcal{G}_M$. In the unpolarized case these are squared and summed, which leads to a cross section proportional to a weighted sum of $|\mathcal{G}_E|^2$ and $|\mathcal{G}_M|^2$. As we stressed earlier, this implies that the phase χ of $\mathcal{G}_E/\mathcal{G}_M$ is not determined by the unpolarized data.

To show how χ can be measured in polarized scattering, it is useful to introduce the polarization observables discussed by Paschke and Quinn [17]. These are angular asymmetries that arise when the polarizations of particles are aligned or antialigned along particular directions. For example, for our reaction $e^+e^- \to p\bar{p}$, $Q(0, 0, z, 0)$ is the difference of two angular distributions, $(d\sigma/d\Omega)_{p\uparrow} - (d\sigma/d\Omega)_{p\downarrow}$. Here we will use x and y for the two transverse axes and z for the longitudinal axis (see Fig. 7). $\hat{x}$ and $\hat{z}$ vary with the particle, and $\hat{y}$ is chosen to be common to all. An entry of 0 signifies an unpolarized particle. Since there are four possible arguments for each particle, 0, x, y, and z, there are $4^4 = 256$ polarization observables for this process. Of course there is considerable redundancy, since they are all determined by the 16 helicity amplitudes. The constraints of parity and charge conjugation reduce this set to 6 independent helicity amplitudes, and for massless leptons (as we assume here) this is further reduced to 3 independent nonzero helicity amplitudes.

We introduce the normalized polarization observables $\mathcal{Q}_{\epsilon_{e^+}\epsilon_{e^-}\epsilon_{\bar{p}}\epsilon_p} \equiv Q(\epsilon_{e^+}, \epsilon_{e^-}, \epsilon_{\bar{p}}, \epsilon_p)/Q(0, 0, 0, 0)$, where $Q(0, 0, 0, 0)$ is the unpolarized differential cross section. The (nonzero) polarization observables for this process satisfy the relations

$$
\begin{aligned}
&(a)\ \mathcal{Q}_{0000} = \mathcal{Q}_{xxyy} = \mathcal{Q}_{yyyy} = -\mathcal{Q}_{zz00} = 1,\\
&(b)\ \mathcal{Q}_{00y0} = \mathcal{Q}_{xx0y} = \mathcal{Q}_{yy0y} = \mathcal{Q}_{zz0y} = -\mathcal{Q}_{000y}\\
&\qquad = -\mathcal{Q}_{xxy0} = -\mathcal{Q}_{yyy0} = -\mathcal{Q}_{zzy0},\\
&(c)\ \mathcal{Q}_{xx00} = \mathcal{Q}_{yy00} = \mathcal{Q}_{00yy} = -\mathcal{Q}_{zzyy},\\
&(d)\ \mathcal{Q}_{z0\times0} = \mathcal{Q}_{z00x} = \mathcal{Q}_{yxyz} = \mathcal{Q}_{yxzy} = -\mathcal{Q}_{0zx0}\\
&\qquad = -\mathcal{Q}_{0z0x} = -\mathcal{Q}_{xyyz} = -\mathcal{Q}_{xyzy},\\
&(e)\ \mathcal{Q}_{z0z0} = \mathcal{Q}_{0z0z} = \mathcal{Q}_{xyxy} = \mathcal{Q}_{yxyx} = -\mathcal{Q}_{0zz0}\\
&\qquad = -\mathcal{Q}_{z00z} = -\mathcal{Q}_{yxxy} = -\mathcal{Q}_{xyyx}\\
&(f)\ \mathcal{Q}_{xxxx} = \mathcal{Q}_{yyxx} = \mathcal{Q}_{zzzz} = -\mathcal{Q}_{00zz},\\
&(g)\ \mathcal{Q}_{00xx} = -\mathcal{Q}_{zzxx} = -\mathcal{Q}_{xxzz} = -\mathcal{Q}_{yyzz},\\
&(h)\ \mathcal{Q}_{00xz} = \mathcal{Q}_{xxzx} = \mathcal{Q}_{yyzx} = \mathcal{Q}_{zzzx} = -\mathcal{Q}_{xxxz}\\
&\qquad = -\mathcal{Q}_{yyxz} = -\mathcal{Q}_{zzxz} = -\mathcal{Q}_{00zx},\\
&(i)\ \mathcal{Q}_{xyx0} = \mathcal{Q}_{xy0x} = \mathcal{Q}_{z0yz} = \mathcal{Q}_{z0zy} = -\mathcal{Q}_{yxx0}\\
&\qquad = -\mathcal{Q}_{yx0x} = -\mathcal{Q}_{0zyz} = -\mathcal{Q}_{0zzy}.
\end{aligned}
\tag{16}
$$

Explicit expressions for these observables are given in Table I.

The results in Table I suggest how we may determine χ experimentally. Inspection of the table shows that only four of the entries depend on χ; two are proportional to $\sin\chi$ and two to $\cos\chi$. Assuming that one knows ρ with suffi-

TABLE I. Nonzero inequivalent polarization observables in $e^+e^- \to J/\psi \to p\bar{p}$. The function F is $4 - 2(1-\rho^2)\sin^2\theta$.

Pol. observable	Result
$\mathcal{Q}_{0000}$	1
$\mathcal{Q}_{00y0}$	$4\rho\sin\chi\sin\theta\cos\theta/F$
$\mathcal{Q}_{xx00}$	$2(1-\rho^2)\sin^2\theta/F$
$\mathcal{Q}_{z0x0}$	$4\rho\cos\chi\sin\theta/F$
$\mathcal{Q}_{z0z0}$	$4\cos\theta/F$
$\mathcal{Q}_{00xz}$	$-4\rho\cos\chi\sin\theta\cos\theta/F$
$\mathcal{Q}_{xyx0}$	$-4\rho\sin\chi\sin\theta/F$
$\mathcal{Q}_{xxxx}$	$[4-2(1+\rho^2)\sin^2\theta]/F$
$\mathcal{Q}_{zzxx}$	$-2(1+\rho^2)\sin^2\theta/F$

cient accuracy from the unpolarized data, one may then determine χ unambiguously by extracting $\sin\chi$ and $\cos\chi$ from the measurement of two of these polarization observables.

The determination of $\sin\chi$ is the most straightforward, since it only requires the detection of a single final polarized particle (for example the proton, through $\mathcal{Q}_{00y0}$). If κ is close to real, which corresponds to $\chi \approx 0$ or $\approx \pi$, this observable may be relatively small. The other polarization observables that are proportional to $\sin\chi$ involve asymmetries with either one or three particles polarized; these are given in relations (b) and (i) of Eq. (16).

Determining $\cos\chi$ involves measuring double or quadruple polarization observables, which are given in relations (d) and (h) in Eq. (16). In the double polarization case, either one initial and one final polarization are measured (such as e^- and p) or the polarizations of both final particles (p and $\bar{p}$) are measured. In the first case the relevant observables (such as $\mathcal{Q}_{z0x0}$) require the initial lepton to have longitudinal ($\pm\hat{z}$) polarization, which is difficult to achieve experimentally. In the second case the initial e^+e^- beams are unpolarized, and the longitudinal polarization of one final particle and the transverse polarization of the other must be measured. Determining the $\bar{p}$ polarization may prove to be an experimental challenge.

Of these two general possibilities, the most attractive ''next experiment'' beyond unpolarized $e^+e^- \to J/\psi \to p\bar{p}$ scattering may be a measurement of the differential cross section with unpolarized leptons and only the final p polarization detected. This will determine $\sin\chi$, which specifies χ up to the usual trigonometric ambiguities.

Another interesting experimental possibility is to resolve the phase ambiguity in unpolarized $e^+e^- \to J/\psi \to p\bar{p}$ scattering through a study of the closely related reaction $e^+e^- \to J/\psi \to \Lambda\bar{\Lambda}$, which has recently been observed by *BABAR* [18] using the ISR technique. Since the $\psi p\bar{p}$ and $\psi\Lambda\bar{\Lambda}$ couplings are identical in the SU(3) flavor symmetry limit, a determination of $J/\psi\Lambda\bar{\Lambda}$ couplings would suggest plausible $J/\psi p\bar{p}$ couplings. This approach has some experimental advantages; as the Λ and $\bar{\Lambda}$ decays are self-analyzing, no rescattering of the final baryons is required to determine their polarization. In addition no beam polarization is required, since it suffices to measure the (odd-ρ) polarization observables $\mathcal{Q}_{00y0}$ and $\mathcal{Q}_{00xz}$. One may also measure the even-ρ observables $\mathcal{Q}_{00xx}$ and $\mathcal{Q}_{00zz}$ as a cross-check of the result for ρ.

Finally, we note in passing that it may also be possible to measure the appropriate polarization observables in the time-reversed reaction $p\bar{p} \to J/\psi \to e^+e^-$.

VI. SUMMARY AND CONCLUSIONS

The unpolarized angular distribution for the process $e^+e^- \to J/\psi \to p\bar{p}$, measured recently by the BES Collaboration, is inconsistent with theoretical expectations for a pure Dirac $J/\psi p\bar{p}$ coupling. In this paper we have derived the effect of an additional Pauli-type $J/\psi p\bar{p}$ coupling, and find that this can accommodate the observed angular distribution. The $J/\psi p\bar{p}$ Pauli coupling may significantly affect the cross section for the charmonium production reaction $p\bar{p} \to \pi^0 J/\psi$, which will be studied at PANDA. There is an ambiguity in determining the relative Dirac and Pauli $J/\psi p\bar{p}$ couplings from the unpolarized $e^+e^- \to J/\psi \to p\bar{p}$ data; we noted that this ambiguity can be fully resolved through measurements of the polarized reaction. The most attractive polarized process to study initially appears to be the case of unpolarized initial e^+e^- beams, with only the final p (transversely) polarized. Alternatively, measurement of the required polarization observables may also be possible using the time-reversed reaction $p\bar{p} \to J/\psi \to e^+e^-$. It may also be possible to use self-analyzing processes such as $e^+e^- \to J/\psi \to \Lambda\bar{\Lambda}$ to estimate the Dirac and Pauli couplings in the closely related $J/\psi\Lambda\bar{\Lambda}$ vertex.

ACKNOWLEDGMENTS

We are happy to acknowledge useful communications with W. M. Bugg, K.-T. Chao, V. Ciancolo, F. E. Close, S. Olsen, J.-M. Richard, K. Seth, S. Spanier, E. S. Swanson, U. Wiedner, C. Y. Wong, and Q. Zhao regarding this research. We also gratefully acknowledge the support of the Institute of High Energy Physics (Beijing) of the Chinese Academy of Sciences, the Department of Physics and Astronomy at the University of Tennessee, and the Department of Physics, the College of Arts and Sciences, and the Office of Research at Florida State University. This research was supported in part by the U.S. Department of Energy under Contract No. DE-AC05-00OR22725 at Oak Ridge National Laboratory and was authored by Jefferson Science Associates, LLC under U.S. DOE Contract No. DE-AC05-06OR23177 (W. R.).

[1] Technical progress report for PANDA, Strong Interaction Studies with Antiprotons (2005).
[2] M. K. Gaillard, L. Maiani, and R. Petronzio, Phys. Lett. **110B**, 489 (1982).
[3] A. Lundborg, T. Barnes, and U. Wiedner, Phys. Rev. D **73**, 096003 (2006).
[4] T. Barnes and X. Li, Phys. Rev. D **75**, 054018 (2007).
[5] I. Peruzzi *et al.* (MARK I Collaboration), Phys. Rev. D **17**, 2901 (1978).
[6] R. Brandelik *et al.* (DASP Collaboration), Z. Phys. C **1**, 233 (1979).
[7] M. W. Eaton *et al.* (MARK II Collaboration), Phys. Rev. D **29**, 804 (1984).
[8] J. S. Brown, Ph.D. thesis, Washington University (Seattle) [Report No. UMI84-19117, 1984].
[9] D. Pallin *et al.* (DM2 Collaboration), Nucl. Phys. **B292**, 653 (1987).
[10] J. Z. Bai *et al.* (BES Collaboration), Phys. Lett. B **591**, 42 (2004).
[11] M. Ambrogiani *et al.* (Fermilab E835 Collaboration), Phys. Lett. B **610**, 177 (2005).
[12] M. Ablikim *et al.* (BES Collaboration), Phys. Lett. B **648**, 149 (2007).
[13] M. Claudson, S. L. Glashow, and M. B. Wise, Phys. Rev. D **25**, 1345 (1982).
[14] C. Carimalo, Int. J. Mod. Phys. A **2**, 249 (1987).
[15] S. J. Brodsky and G. P. Lepage, Phys. Rev. D **24**, 2848 (1981).
[16] W. M. Yao *et al.* (Particle Data Group), J. Phys. G **33**, 1 (2006).
[17] K. Paschke and B. Quinn, Phys. Lett. B **495**, 49 (2000).
[18] B. Aubert *et al.* (*BABAR* Collaboration), Phys. Rev. D **76**, 092006 (2007).

PHYSICAL REVIEW D **81,** 034025 (2010)

Meson emission model of $\Psi \to N\bar{N}m$ charmonium strong decays

T. Barnes,[1,2,*] Xiaoguang Li,[2,†] and W. Roberts[3,‡]

[1]*Physics Division, Oak Ridge National Laboratory, Oak Ridge, Tennessee 37831-6373, USA*
[2]*Department of Physics and Astronomy, University of Tennessee, Knoxville, Tennessee 37996-1200, USA*
[3]*Department of Physics and Astronomy, Florida State University, Tallahassee, Florida 32306-4350, USA*
(Received 12 January 2010; revised manuscript received 25 January 2010; published 19 February 2010)

In this paper we consider a sequential ''meson emission'' mechanism for charmonium decays of the type $\Psi \to N\bar{N}m$, where Ψ is a generic charmonium state, N is a nucleon, and m is a light meson. This decay mechanism, which may not be dominant in general, assumes that an $N\bar{N}$ pair is created during charmonium annihilation, and the light meson m is emitted from the outgoing nucleon or antinucleon line. A straightforward generalization of this model can incorporate intermediate N^* resonances. We derive Dalitz plot event densities for the cases $\Psi = \eta_c$, J/ψ, χ_{c0}, χ_{c1}, and ψ'; and $m = \pi^0$, f_0, and ω (and implicitly, any 0^{-+}, 0^{++}, or 1^{--} final light meson). It may be possible to separate the contribution of this decay mechanism to the full decay amplitude through characteristic event densities. For the decay subset $\Psi \to p\bar{p}\pi^0$ the two model parameters are known, so we are able to predict absolute numerical partial widths for $\Gamma(\Psi \to p\bar{p}\pi^0)$. In the specific case $J/\psi \to p\bar{p}\pi^0$ the predicted partial width and $M_{p\pi}$ event distribution are intriguingly close to experiment. We also consider the possibility of scalar meson and glueball searches in $\Psi \to p\bar{p}f_0$. If the meson emission contributions to $\Psi \to N\bar{N}m$ decays can be isolated and quantified, they can be used to estimate meson-nucleon strong couplings $\{g_{NNm}\}$, which are typically poorly known, and are a crucial input in meson exchange models of the NN interaction. The determination of $g_{NN\pi}$ from $J/\psi \to p\bar{p}\pi^0$ and the (poorly known) $g_{NN\omega}$ and the anomalous ''strong magnetic'' coupling $\kappa_{NN\omega}$ from $J/\psi \to p\bar{p}\omega$ are considered as examples.

DOI: 10.1103/PhysRevD.81.034025 PACS numbers: 13.25.Gv, 13.75.Cs, 13.75.Gx, 21.30.−x

I. INTRODUCTION

Charmonium strong decays of the type $\Psi \to N\bar{N}m$, where Ψ is a generic charmonium state, N is a nucleon, and m is a light meson, have recently attracted interest both as sources of information regarding the N^* spectrum [1–5] and in searches for a low-energy $N\bar{N}$ enhancement ''$X(1835)$,'' which has been reported in $J/\psi \to \gamma p\bar{p}$ [6] and $J/\psi \to \gamma\pi^+\pi^-\eta'$ [7,8], but thus far not in $\Psi \to p\bar{p}m$. These decays are also of interest because their partial widths can be used to estimate the $p\bar{p} \to m\Psi$ associated charmonium production cross sections at $\bar{\text{P}}$ANDA [9,10]. As we shall show here, they may also provide information on NNm meson-nucleon coupling constants, which could be used to identify unusual resonances such as molecule or glueball candidates.

Specific $\Psi \to N\bar{N}m$ reactions that have recently been studied experimentally include $J/\psi \to p\bar{p}\pi^0$ [1], $p\bar{p}\eta$ and $p\bar{p}\eta'$ [4], and $p\bar{p}\omega$ [5]; $\psi' \to p\bar{p}\pi^0$ [2], $p\bar{p}\eta$ [2,11], $p\bar{n}\pi^-$ + H.c. [3], $p\bar{p}\rho$ [11] and $p\bar{p}\omega$ [11,12], and (upper limit) $p\bar{p}\phi$ [11,12]; and $\chi_{cJ} \to p\bar{p}\pi^0$ and $p\bar{p}\eta$ [13].

These decays may prove to be complicated processes in which several decay mechanisms contribute significantly. For this reason it will be useful to have predictions for $\Psi \to N\bar{N}m$ Dalitz plot (DP) event densities assuming various decay mechanisms; this paper provides these results for one such mechanism. In particular we derive the DP event densities that follow from sequential meson emission, in which the charmonium state (generically Ψ) decays to an intermediate $N\bar{N}$ state, which radiates the light meson from the N or $\bar{N}$ line, $\Psi \to N\bar{N} \to N\bar{N}m$. The two Feynman diagrams assumed in this model are shown in Fig. 1.

We emphasize that the actual relative importance of this and other $\Psi \to N\bar{N}m$ decay mechanisms is unclear at present, and may depend strongly on the charmonium state Ψ and the light meson m; one purpose of this paper is to determine the rates predicted by this meson emission decay model in isolation for comparison with experiment, so that the importance of this decay mechanism can be estimated.

The predictions of this $\Psi \to N\bar{N} \to N\bar{N}m$ decay model can be given in some cases with no free parameters, since the strengths of the *a priori* unknown couplings $\Psi N\bar{N}$ and NNm can be estimated from other processes. Here we will

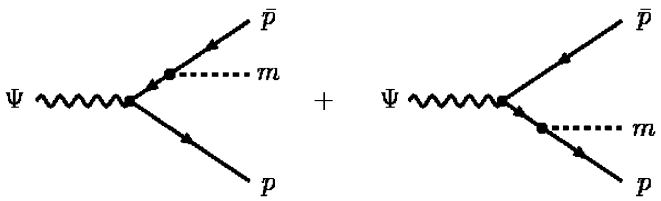

FIG. 1. Feynman diagrams of the meson emission model.

*tbarnes@utk.edu
†xli22@utk.edu
‡wroberts@fsu.edu

give absolute predictions for the set of partial widths $\{\Gamma(\Psi \to p\bar{p}\pi^0)\}$; we use the known partial widths $\{\Gamma(\Psi \to p\bar{p})\}$ to estimate the $\{\Psi NN\bar{}\}$ couplings, and the final $NN\pi$ coupling is of course well known.

Provided that the contribution of the $\Psi \to N\bar{N} \to N\bar{N}m$ decay mechanism can be isolated and quantified experimentally, this information can be used to estimate meson-nucleon strong coupling constants; these are generally poorly known, and play an important role in nuclear physics as input parameters in meson exchange models of the NN force [14–21].

We will also discuss the determination of the (well known) $p\bar{p}\pi^0$ and the (poorly known) $p\bar{p}\omega$ couplings from the decays $J/\psi \to p\bar{p}\pi^0$, $\psi' \to p\bar{p}\pi^0$, and $J/\psi \to p\bar{p}\omega$ as examples. This provides a third motivation for the study of $\Psi \to N\bar{N}m$ decays; they may prove useful for estimating NNm coupling constants, in addition to their relevance to N^* spectroscopy [1–5] and low-mass $p\bar{p}$ dynamics [6–8]. Another motivation for studying $\Psi \to N\bar{N}m$ is the possibility of observing light scalars, including the "σ," the 980 MeV states, and the scalar glueball, in the decays $\Psi \to p\bar{p}f_0$ (and a_0).

II. FORMULAS

Here we will usually specialize to charmonium decays to a $p\bar{p}$ pair and a neutral meson, $\Psi \to p\bar{p}m^0$; these decays are reasonably well studied, and enjoy the simplification of equal baryon and antibaryon masses. Our results employ conventions for kinematic variables, meson-baryon couplings, and masses that were used in Ref. [22]. In particular, M is the mass of the initial charmonium state, m_p is the proton mass, m_m is the mass of meson (subscript) m, and dimensionless mass ratios $R \equiv M/m_p$ and $r \equiv m_m/m_p$ are defined relative to the proton mass. (Hence the numerical values of R and r depend on the decay process.) We use scaled dimensionless variables $x = M^2_{pm}/m^2_p - 1$ and $y = M^2_{\bar{p}m}/m^2_p - 1$ and their inverses $u = 1/x$ and $v = 1/y$ to describe Dalitz plots; these greatly simplify our results. The DP event densities we present here are formally partial width densities in x and y, which are related to the more familiar differential partial widths by a trivial overall constant,

$$\frac{d^2\Gamma(\Psi \to p\bar{p}m)}{dxdy} = m_p^4 \frac{d^2\Gamma(\Psi \to p\bar{p}m)}{dM^2_{pm}dM^2_{\bar{p}m}}. \quad (1)$$

Before we give our results for these event densities, it is useful to recall some general properties of a $\Psi \to p\bar{p}m$ Dalitz plot. The boundary in the dimensionless variables (x, y) is specified by the curves

$$y_\pm = \frac{r^2R^2 + (r^2 + R^2 - 2)x - x^2 \pm F_m F_\Psi}{2(1 + x)}, \quad (2)$$

where $F_m = F(r, x)$ and $F_\Psi = F(R, x)$, with

$$F(a, x) \equiv (a^2(a^2 - 4) - 2a^2x + x^2)^{1/2}. \quad (3)$$

The range of values of x (and y) in the physical region is

$$r(r + 2) \le x \le R(R - 2). \quad (4)$$

The areas $\{A_D\}$ of these Dalitz plots are useful for estimating $\Gamma(\Psi \to p\bar{p}m)$ partial widths [9]. Although A_D can be evaluated in closed form for $\Psi \to p\bar{p}m$ with general mass ratios r and R, the resulting expression is quite lengthy, so when required we will simply evaluate each A_D numerically.

In deriving the DP event densities we have usually assumed that the $\Psi p\bar{p}$ coupling is a constant $g_{\Psi p\bar{p}}$ times the simplest relevant Dirac matrix for the given Ψ quantum numbers; for example, for the J/ψ we use a pure vector $J/\psi p\bar{p}$ vertex, $-ig_{J/\psi p\bar{p}}\gamma_\mu$. The order of the hadron labels in g_{abc} is meant to reflect the fact that the numerical value of this coupling constant is taken from an $a \to bc$ transition, here $J/\psi \to p\bar{p}$. This could be a significant concern if form factor effects are large.

We proceed similarly for the light mesons π^0 and f_0; for the pion we use a pure pseudoscalar $NN\pi$ coupling, with vertex $g_{NN\pi}\gamma_5$, and $-ig_{NNf_0}I$ for the NNf_0 vertex. Since light vector mesons (generically represented by the ω) have two interesting strong couplings, Dirac (vector) and Pauli (anomalous magnetic), for this special case we assume a vertex with two interactions,

$$\Gamma^{(\omega)}_\mu = -ig_{NN\omega}(\gamma_\mu + i(\kappa_{NN\omega}/2m_p)\sigma_{\mu\nu}q_\nu). \quad (5)$$

Reference [23] assumed a similar $J/\psi p\bar{p}$ vertex; see Ref. [22] for additional details regarding the couplings assumed here. We generally abbreviate these coupling constants as $g_\Psi \equiv g_{\Psi N\bar{N}}$ and $g_m \equiv g_{NNm}$; rationalized squared couplings $\alpha_\Psi \equiv g^2_\Psi/4\pi$ and $\alpha_m \equiv g^2_m/4\pi$ are also used.

For the special case of $p\bar{p}\pi^0$ final states, these event densities can be obtained by applying crossing relations to our previously published results for the unpolarized differential cross sections for the $2 \to 2$ processes $p\bar{p} \to \pi^0\Psi$ [22]; the other (f_0 and ω) cases have not been considered previously. The results for all cases considered here are given below.

$$\frac{d^2\Gamma(\eta_c \to p\bar{p}\pi^0)}{dxdy} = \alpha_{\eta_c}\alpha_\pi \frac{m_p}{8\pi R^3} \times \left\{(u - v)^2 \cdot \left(\frac{1}{uv} - r^2R^2\right)\right\} \quad (6)$$

$$\frac{d^2\Gamma(J/\psi \to p\bar{p}\pi^0)}{dxdy} = \alpha_{J/\psi}\alpha_\pi \frac{m_p}{12\pi R^3}\left\{\frac{(u + v)^2}{uv} - 2(u + v)(u + v + 1)r^2 + 2uvr^4 - (u^2 + v^2) \cdot r^2R^2\right\} \quad (7)$$

$$\frac{d^2\Gamma(\chi_{c0} \to p\bar{p}\pi^0)}{dxdy} = \alpha_{\chi_{c0}}\alpha_\pi \frac{m_p}{8\pi R^3}\left\{(u+v)^2 \cdot \left(\frac{1}{uv} + 4r^2 - r^2R^2\right)\right\} \tag{8}$$

$$\frac{d^2\Gamma(\chi_{c1} \to p\bar{p}\pi^0)}{dxdy} = \alpha_{\chi_{c1}}\alpha_\pi \frac{m_p}{6\pi R^5}\left\{-\frac{(u+v)}{uv} \cdot (u+v+1) + r^2 + \frac{(u^2+v^2)}{2uv}R^2 + (2(u^2+v^2)+u+v)r^2R^2 - uvr^4R^2 - \frac{(u^2+v^2)}{2}r^2R^4\right\} \tag{9}$$

$$\frac{d^2\Gamma(\eta_c \to p\bar{p}f_0)}{dxdy} = \alpha_{\eta_c}\alpha_{f_0} \frac{m_p}{8\pi R^3}\left\{(u+v)^2 \cdot \left(\frac{1}{uv} + 4R^2 - r^2R^2\right)\right\} \tag{10}$$

$$\frac{d^2\Gamma(J/\psi \to p\bar{p}f_0)}{dxdy} = \alpha_{J/\psi}\alpha_{f_0} \frac{m_p}{12\pi R^3}\left\{\frac{(u+v)^2}{uv} + 8(u+v)(u+v+1) - 2(u(u+1)+v(v+1) + 6uv)r^2 + 4(u+v)^2R^2 + 2uvr^4 - (u^2+v^2)\cdot r^2R^2\right\} \tag{11}$$

$$\frac{d^2\Gamma(\chi_{c0} \to p\bar{p}f_0)}{dxdy} = \alpha_{\chi_{c0}}\alpha_{f_0} \frac{m_p}{8\pi R^3}\left\{\frac{(u-v)^2}{uv} - 16(u+v)(u+v+1) + 4(u+v)^2(r^2+R^2) - (u-v)^2r^2R^2\right\} \tag{12}$$

$$\frac{d^2\Gamma(\chi_{c1} \to p\bar{p}f_0)}{dxdy} = \alpha_{\chi_{c1}}\alpha_{f_0} \frac{m_p}{6\pi R^5}\left\{-\frac{(u+v)}{uv}\cdot(u+v+1) + r^2 + \left(\frac{(u^2+v^2)}{2uv} - 8(u+v)\cdot(u+v+1)\right)R^2 + (2(u^2+v^2)+8uv+u+v)r^2R^2 + 2(u+v)^2R^4 - uvr^4R^2 - \frac{(u^2+v^2)}{2}r^2R^4\right\} \tag{13}$$

$$\frac{d^2\Gamma(\eta_c \to p\bar{p}\omega)}{dxdy} = \alpha_{\eta_c}\alpha_\omega \frac{m_p}{4\pi R^3}\left\{\left[\frac{(u+v)^2}{uv} - 2(u+v)(u+v+1)R^2 - (u^2+v^2)r^2R^2 + 2uvR^4\right] + \kappa_\omega\left[-\frac{2(u+v)^2}{uv} + (3(u^2+v^2)+2uv)r^2R^2\right] + \kappa_\omega^2\left[\frac{(u+v)(u+v-1)}{2uv} + \frac{(u+v)^2}{8uv}r^2 + \frac{1}{2}R^2 + \left(\frac{(u+v)}{2} - (u^2+v^2)\right)r^2R^2 - \frac{(u+v)^2}{8}r^4R^2 - \frac{uv}{2}r^2R^4\right]\right\} \tag{14}$$

$$\frac{d^2\Gamma(J/\psi \to p\bar{p}\omega)}{dxdy} = \alpha_{J/\psi}\alpha_\omega \frac{m_p}{6\pi R^3}\left\{\left[\frac{(u^2+v^2)}{uv} - 4(u+v)(u+v+1) - 2(u(u+1)+v(v+1))\cdot(r^2+R^2) + 2uvr^4 - (u^2+v^2-4uv)r^2R^2 + 2uvR^4\right] + \kappa_\omega\left[-\frac{(u+v)^2}{uv} + 6(u+v)(u+v+1)r^2 - 6uvr^4 + (3(u^2+v^2)-8uv)r^2R^2\right] + \kappa_\omega^2\left[-\frac{(u+v)}{2uv} + \left(\frac{(u+v)^2}{8uv} - 2(u+v)(u+v+1)\right)r^2 + \frac{1}{2}R^2 - \frac{1}{4}(u(u+1)+v(v+1)-6uv)r^4 - (u-v)^2r^2R^2 + \frac{1}{4}uvr^6 - \frac{1}{8}(u^2+v^2-4uv)r^4R^2\right]\right\} \tag{15}$$

$$\frac{d^2\Gamma(\chi_{c0} \to p\bar{p}\omega)}{dxdy} = \alpha_{\chi_{c0}}\alpha_\omega \frac{m_p}{4\pi R^3}\left\{\left[\frac{(u+v)^2}{uv} + 8(u+v)(u+v+1) + 4(u+v)^2r^2 - 2(u(u+1)+v(v+1) + 6uv)R^2 - (u^2+v^2)r^2R^2 + 2uvR^4\right] + \kappa_\omega\left[-12(u+v)\left(u+v+\frac{1}{2}\right)r^2 + 3(u+v)^2r^2R^2\right] + \kappa_\omega^2\left[-\frac{(u+v)(u+v+1)}{2uv} + \left(\frac{(u^2+6uv+v^2)}{8uv} + 4(u+v)(u+v+1)\right)r^2 + \frac{1}{2}R^2 + \frac{(u+v)^2}{2}r^4 - \left(u^2+4uv+v^2+\frac{(u+v)}{2}\right)r^2R^2 - \frac{(u-v)^2}{8}r^4R^2 + \frac{uv}{2}r^2R^4\right]\right\} \tag{16}$$

$$\frac{d^2\Gamma(\chi_{c1}\to p\bar{p}\omega)}{dxdy}=\alpha_{\chi_{c1}}\alpha_\omega\frac{m_p}{3\pi R^5}\Big\{\Big[\frac{(u+v)^2}{uv}+\Big(\frac{(u^2+v^2)}{2uv}+4(u+v)(u+v+1)\Big)R^2+(2(u-v)^2-u-v)r^2R^2$$
$$-(u^2+v^2+6uv+u+v)R^4+uvr^4R^2+\Big(2uv-\frac{(u^2+v^2)}{2}\Big)r^2R^4+uvR^6\Big]$$
$$+\kappa_\omega\Big[-\frac{(u+v)^2}{uv}-r^2-\frac{(u^2+v^2-4uv)}{2uv}\cdot R^2-(6(u^2+v^2)+u+v)r^2R^2-uvr^4R^2$$
$$+\frac{3}{2}(u^2+v^2)r^2R^4\Big]+\kappa_\omega^2\Big[\frac{(1+2(u+v)+2(u+v)^2)}{4uv}-\frac{(u+v+(u-v)^2)}{8uv}r^2-\Big(\frac{3}{2}+\frac{(u+v)}{4uv}\Big)R^2$$
$$+\frac{1}{8}r^4+\Big(2(u^2+v^2-uv)+\frac{(u+v)}{2}+\frac{(u^2+v^2+4uv)}{16uv}\Big)\cdot r^2R^2+\frac{1}{4}R^4+\frac{1}{8}(u+v+2(u^2+v^2$$
$$+6uv))r^4R^2-\frac{1}{2}(u^2+v^2-uv)r^2R^4-\frac{1}{8}uvr^6R^2-\frac{1}{16}(u^2+v^2+4uv)r^4R^4\Big]\Big\}. \quad (17)$$

The symmetry of these event densities under (x, y) and hence (u, v) interchange is a consequence of C-parity invariance. There are singularities in these events densities along the lines $x = 0$ $(u = \infty)$ and $y = 0$ $(v = \infty)$, corresponding to $M^2_{pm} = m_p^2$ and $M^2_{\bar{p}m} = m_p^2$. These are due to the poles of the p and $\bar{p}$ propagators in the Feynman diagrams for the decay process $\Psi \to p\bar{p} \to p\bar{p}m$ (Fig. 1) and lie outside the physical regions of the Dalitz plots.

III. APPLICATIONS

A. The $J/\psi \to p\bar{p}\pi^0$ partial width

As a first application we will evaluate the partial width for $J/\psi \to p\bar{p}\pi^0$ assuming this meson emission decay mechanism. The Particle Data Group (PDG) [24] quotes a branching fraction of

$$B(J/\psi \to p\bar{p}\pi^0) = 1.09 \pm 0.09 \cdot 10^{-3}, \quad (18)$$

which is the average of early measurements by Mark-I [25], DASP [26], and Mark-II [27]. There are also more recent experimental results on this decay from BES-II [1]. Using the current PDG value for the J/ψ total width of 93.2 ± 2.1 keV, this branching fraction corresponds to a partial width of

$$\Gamma(J/\psi \to p\bar{p}\pi^0) = 102 \pm 9 \text{ eV}. \quad (19)$$

To evaluate this partial width in the meson emission model we simply integrate the theoretical event density (7) over the Dalitz plot. This event density is given by

$$\frac{d^2\Gamma(J/\psi \to p\bar{p}\pi^0)}{dxdy} = \alpha_{J/\psi}\alpha_\pi m_p \rho(x, y), \quad (20)$$

where the dimensionless density function ρ is

$$\rho(x, y) = \frac{1}{12\pi R^3}\Big\{\frac{(u+v)^2}{uv} - 2(u+v)(u+v+1)r^2 + 2uvr^4 - (u^2+v^2)r^2R^2\Big\}. \quad (21)$$

This (parameter-free) relative event density, scaled to the maximum value in the physical region, is shown in Fig. 2. Integrating (20) over the Dalitz plot gives

$$\Gamma(J/\psi \to p\bar{p}\pi^0) = \alpha_{J/\psi}\alpha_\pi m_p \cdot \langle\rho\rangle \cdot A_D/m_p^4, \quad (22)$$

where $\langle\rho\rangle$ is the mean value of $\rho(x, y)$ in the Dalitz plot, which has (physical) area A_D;

$$\iint_{\text{DP}} \rho dxdy = \langle\rho\rangle \cdot A_D/m_p^4. \quad (23)$$

We evaluate $\langle\rho\rangle$ and A_D numerically, assuming physical hadron masses; we use PDG masses rounded to 0.1 MeV; $m_{\pi^0} = 0.1350$ GeV, $m_p = 0.9383$ GeV, and $m_{J/\psi} = 3.0969$ GeV, which leads to $\langle\rho\rangle = 3.070 \cdot 10^{-3}$ and $A_D = 9.265$ GeV^4, and a partial width of

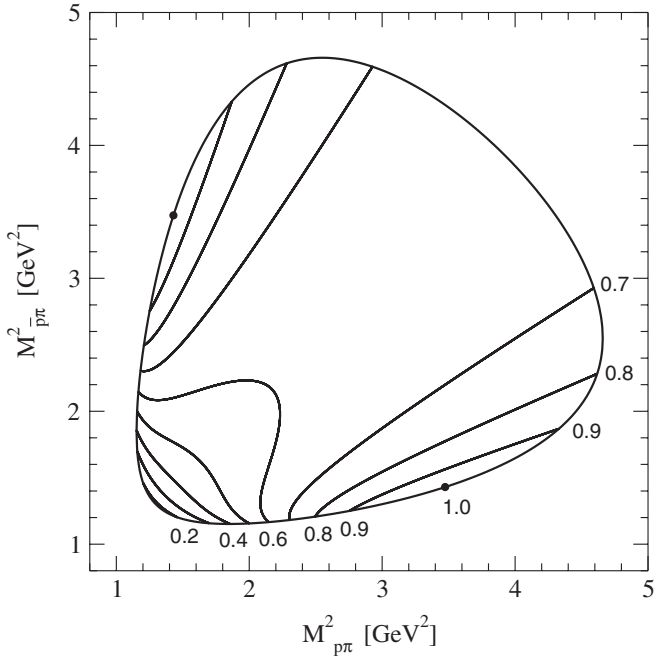

FIG. 2. The $J/\psi \to p\bar{p}\pi^0$ DP event density predicted by the meson emission decay mechanism $J/\psi \to p\bar{p} \to p\bar{p}\pi^0$, Eq. (7). Contours of equal density are shown.

$$\Gamma(J/\psi \to p\bar{p}\pi^0) = 34.44 \cdot \alpha_{J/\psi}\alpha_\pi \text{ MeV}. \quad (24)$$

To complete this estimate we require numerical values for the $NN\pi$ and $J/\psi N\bar{N}$ coupling constants. For $NN\pi$ there is general agreement from meson exchange models of NN scattering that $g_{NN\pi} \approx 13$ (see for example [14–21]); we accordingly set $g_{NN\pi} = 13.0$. The value of the $J/\psi N\bar{N}$ coupling constant (here $g_{J/\psi p\bar{p}}$) can be estimated from the measured partial width to $p\bar{p}$, which is (again using PDG numbers) $\Gamma(J/\psi \to p\bar{p}) = 202 \pm 8$ eV. Equating this to the theoretical decay rate

$$\Gamma(J/\psi \to p\bar{p}) = \alpha_{J/\psi}\beta_p(1 + 2/R^2)M/3 \quad (25)$$

gives a value of $g_{J/\psi p\bar{p}} = 1.62 \cdot 10^{-3}$, as was quoted previously in Ref. [22]. Using these couplings in Eq. (24) gives our meson emission model prediction

$$\Gamma(J/\psi \to p\bar{p}\pi^0) = 97 \text{ eV}. \quad (26)$$

This is consistent with the experimental value of 102 ± 9 eV quoted in Eq. (19). This excellent agreement is somewhat fortuitous, since this version of the model does not include the N^* contributions evident in the $J/\psi \to p\bar{p}\pi^0$ Dalitz plot [1] (see also Fig. 3).

We note in passing that the charged-pion cases $J/\psi \to p\bar{n}\pi^-$ and $n\bar{p}\pi^+$ should have branching fractions close to twice $B(J/\psi \to p\bar{p}\pi^0)$, reflecting an isospin factor of two. Experimentally this is indeed the case; the ratio of the PDG J/ψ branching fractions to $p\bar{n}\pi^-$ and $p\bar{p}\pi^0$ is $B(J/\psi \to p\bar{n}\pi^-)/B(J/\psi \to p\bar{p}\pi^0) = 1.94 \pm 0.18$.

B. Projected $J/\psi \to p\bar{p}\pi^0$ event densities

Projections of DP event densities onto the invariant mass of one pair of particles are useful in searches for intermediate resonances. For $J/\psi \to p\bar{p}\pi^0$, the BES Collaboration has published acceptance-corrected event densities in $M_{p\pi}$ and $M_{\bar{p}\pi}$ invariant mass (Fig. 6 of Ref. [1]), which show clear evidence for N^* resonances. Here we will generate the corresponding theoretical $M_{p\pi}$-projected event distributions in the meson emission model for comparison with experiment. Although N^* resonances are not incorporated in our calculation, this comparison will test the relative importance of the meson emission decay mechanism in this decay, and establish whether the model predicts a non-N^* "background" invariant mass distribution that is similar to the data in form and magnitude.

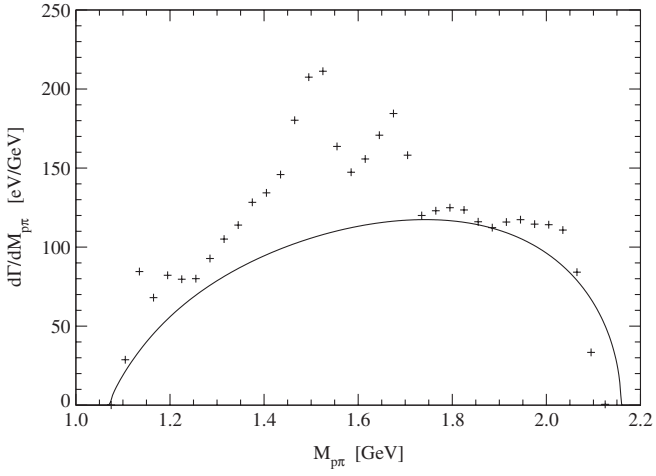

FIG. 3. $J/\psi \to p\bar{p}\pi^0$ experimental (BES) and theoretical (meson emission model, Fig. 2) Dalitz plot (DP) event densities, projected onto $M_{p\pi}$. This is not a fit; see text for discussion.

The full two-dimensional DP event density $d^2\Gamma/dxdy$ predicted by the meson emission model is given by Eq. (7). Projecting this onto $M_{p\pi}$ is straightforward; first one integrates over $y = M^2_{\bar{p}\pi}/m_p^2 - 1$ between the DP boundaries $y_\pm(x)$ of Eq. (2), which gives $d\Gamma/dx$. Converting this into a distribution in $M_{p\pi}$ introduces a Jacobean, which is specified by the definition $x = M^2_{p\pi}/m_p^2 - 1$. This gives

$$\frac{d\Gamma(J/\psi \to p\bar{p}\pi^0)}{dM_{p\pi}} = \frac{2M_{p\pi}}{m_p^2}\int_{y_-(x)}^{y_+(x)} dy \times \frac{d^2\Gamma(J/\psi \to p\bar{p}\pi^0)}{dxdy}. \quad (27)$$

We have evaluated this distribution numerically, given the $d^2\Gamma(J/\psi \to p\bar{p}\pi^0)/dxdy$ of Eq. (7) and the masses and couplings $\alpha_{J/\psi}$ and α_π used in Sec. III A. The result is shown in Fig. 3, together with an experimental distribution provided by BES (reported in Ref. [1]), using a common scale. The data are the combined acceptance-corrected $M_{p\pi}$ and $M_{\bar{p}\pi}$ distribution, scaled to give their reported $B(J/\psi \to p\bar{p}\pi^0) = 1.33 \cdot 10^{-3}$ rather than the PDG value of $1.09 \cdot 10^{-3}$.

Clearly there is a close resemblance between the meson emission model prediction for the $J/\psi \to p\bar{p}\pi^0$ event distribution in $M_{p\pi}$ and the observed BES distribution, both in form and magnitude. This suggests that a study of this reaction assuming this model for the experimental background combined with N^* resonance contributions would be an interesting exercise. Although BES [1] recently reported a similar study, they introduced an *ad hoc* $s_{\pi N}(= M^2_{p\pi})$-dependent form factor that suppressed this background meson emission amplitude relative to N^* contributions. The similarity to experiment evident in Fig. 3 suggests that this mechanism merits additional consideration.

C. Other $\Psi \to p\bar{p}\pi^0$ partial widths

Since the two meson emission model parameters $g_{\Psi p\bar{p}}$ and g_{NNm} are both known for several $\Psi \to p\bar{p}\pi^0$ decays, we are able to give absolute predictions for these partial widths. (We previously used $\Gamma(\Psi \to p\bar{p})$ to estimate $g_{\Psi p\bar{p}}$ [22]; here we again use these values, and set $g_{NN\pi} = 13$.) These $\Psi \to p\bar{p}\pi^0$ partial widths are given in Table I,

TABLE I. Comparison of theory (meson emission model) and experiment for $\Gamma(\Psi \to p\bar{p}\pi^0)$ (see text).

Ψ	$10^3 g_{\Psi p\bar{p}}$	$10^3\langle\rho\rangle$	A_D [GeV^4]	$\Gamma^{\rm thy}_{p\bar{p}\pi^0}$	$\Gamma^{\rm expt}_{p\bar{p}\pi^0}$
η_c	19.0	0.530	6.862	1.7 keV	-
J/ψ	1.62	3.070	9.265	97 eV	102 ± 9 eV
χ_0	5.42	3.691	18.605	2.6 keV	6.0 ± 1.3 keV
χ_1	1.03	0.554	22.351	17 eV	103 ± 43 eV
ψ'	0.97	2.010	30.501	75 eV	41 ± 5 eV

together with some intermediate theoretical quantities and the experimental widths. (These experimental values are the PDG total widths times branching fractions, with errors added in quadrature.)

These rates were derived using Eq. (22), with the appropriate density function ρ chosen from the set Eqs. (6)–(9). In addition to the rates, Table I also gives the coupling constants assumed, the average of the density function ρ over the Dalitz plot, and the DP area A_D in physical units.

It is clear from the table that the wide variation in the absolute scale of partial widths observed experimentally is approximately reproduced by the model, at least at a ''factor-of-two'' level of accuracy. This suggests that the meson emission decay mechanism may indeed be an important component of the decay amplitude in all these decays; a more definitive test would involve a direct comparison of the DP event densities or their two-body projections, as in Fig. 3.

The χ_{c1} case appears to be an exception to this approximate agreement, however in view of the large experimental error it is not clear if this is a real discrepancy; theory and experiment only differ by 2σ.

Although the single experimentally unobserved decay $\eta_c \to p\bar{p}\pi^0$ is predicted by the meson emission model to have a relatively large partial width of 1.7 keV, it is actually considerably suppressed by the presence of an on-diagonal node in the DP event distribution. An experimental study of $\eta_c \to p\bar{p}\pi^0$ would accordingly be very interesting, since the contributions of other decay mechanisms may be easier to identify in the region of the DP where the meson emission model gives a zero or weak contribution.

D. $g_{NN\pi}$ from $B(J/\psi \to p\bar{p}\pi^0)/B(J/\psi \to p\bar{p})$

Previously we noted that $\Psi \to p\bar{p}m$ decays can be used to estimate NNm couplings, provided that the contribution of the meson emission decay mechanism to the decay amplitude can be quantified experimentally. In the following we will use the decay $J/\psi \to p\bar{p}\pi^0$ as an illustration of this approach, since the agreement between the experimental and theoretical partial widths suggests that domination of this decay by meson emission is a reasonable first approximation.

Since the *a priori* unknown coupling $\alpha_{J/\psi}$ cancels in the theoretical branching fraction ratio $B(J/\psi \to p\bar{p}\pi^0)/B(J/\psi \to p\bar{p})$, we can use it to estimate $g_{NN\pi}$ directly. The meson emission model decay width for $\Gamma(J/\psi \to p\bar{p}\pi^0)$ (7) and the two-body decay width (25) imply the following relation between this ratio and the coupling $\alpha_\pi \equiv g^2_{NN\pi}/4\pi$:

$$\alpha_\pi = (1 - 4/R^2)^{1/2} \frac{(R + 2/R)}{3\langle\rho\rangle A_D/m_p^4} \cdot \frac{B(J/\psi \to p\bar{p}\pi^0)}{B(J/\psi \to p\bar{p})}. \tag{28}$$

Substitution of the experimental PDG numbers $B(J/\psi \to p\bar{p}\pi^0) = (1.09 \pm 0.09) \cdot 10^{-3}$ and $B(J/\psi \to p\bar{p}) = (2.17 \pm 0.07) \cdot 10^{-3}$ for these branching fractions leads to the estimate

$$g_{NN\pi}|_{J/\psi \to p\bar{p}\pi^0} = 13.3 \pm 0.6, \tag{29}$$

which is consistent with NN meson exchange model values.

We expect to find approximately equal $g_{NN\pi}$ estimates from other $\Psi \to p\bar{p}$ and $p\bar{p}m$ decay pairs if the meson emission decay mechanism $\Psi \to p\bar{p} \to p\bar{p}\pi^0$ is indeed dominant. A second state Ψ that can be use to estimate $g_{NN\pi}$ is the $\psi'(3686)$. Since the ψ' has the same quantum numbers as the J/ψ, Eq. (28) is again appropriate for our coupling constant estimate. This ψ' case has a much larger $p\bar{p}\pi^0$ DP area A_D than the J/ψ, which is partially compensated by a smaller mean event density $\langle\rho\rangle$. (These quantities are given in Table I.) Using $M = 3.6861$ GeV and the PDG branching fractions $B(\psi' \to p\bar{p}\pi^0) = (1.33 \pm 0.17) \cdot 10^{-4}$ and $B(\psi' \to p\bar{p}) = (2.75 \pm 0.12) \cdot 10^{-4}$, we find the ψ'-based $g_{NN\pi}$ estimate

$$g_{NN\pi}|_{\psi' \to p\bar{p}\pi^0} = 9.9 \pm 0.7. \tag{30}$$

This is similar to but somewhat smaller than the estimate obtained above from J/ψ decays (29), and may give an indication of the accuracy of this approach for estimating NNm coupling constants.

Of course the other relations for α_m analogous to (28) will only be useful if the meson emission decay mechanism is dominant in those decays as well. Otherwise the contribution of this mechanism to the decay must be identified and quantified, for example, through a detailed study of the DP event density.

E. Scalar mesons in $\Psi \to N\bar{N}m$

The long-standing interest in the light scalars makes the possibility of studying them using these decays an attractive prospect. This motivated our inclusion of decay formulas for the processes $\Psi \to p\bar{p}f_0$ in our set of theoretical DP event densities.

Here we will give meson emission model predictions for the branching fractions $B(\Psi \to p\bar{p}f_0)$, where $\Psi = \eta_c$, J/ψ, χ_{c0}, χ_{c1}, and ψ', for a light ''sigma'' meson with $m_{f_0} = 0.5$ GeV. To evaluate these partial widths we proceed as in Sec. III C, and integrate the appropriate decay

width formula from the set Eqs. (10)–(13) over the Dalitz plot. We again use the $\Psi p\bar{p}$ coupling constants of Sec. III C, as given in Table I. The total widths used to convert the calculated partial widths to branching fractions are the current PDG values, $\Gamma(\eta_c) = 27.4$ MeV, $\Gamma(J/\psi) = 93.2$ keV, $\Gamma(\chi_{c0}) = 10.4$ MeV, $\Gamma(\chi_{c1}) = 0.86$ MeV, and $\Gamma(\psi') = 309$ keV. Our results are given in Table II. Since there is no general agreement regarding an $NNf_0(500)$ coupling constant, in the table we first give the predicted branching fraction relative to $B(J/\psi \to p\bar{p}f_0(500)) \equiv B_0$, which is numerically $0.338 \cdot 10^{-4} \cdot g^2_{NNf_0}$. (The unknown g_{NNf_0} cancels in these ratios.) The next column gives absolute $B(\Psi \to p\bar{p}f_0(500))$ branching fractions for a rather arbitrarily chosen $g_{NNf_0} = 10$. Finally, the table quotes experimental branching fractions for the related processes $\Psi \to p\bar{p}\pi^+\pi^-$ for comparison.

The relative theoretical branching fractions (Table II, column 2) suggest that the best channel for identifying a light scalar in $\Psi \to p\bar{p}f_0$ is $J/\psi \to p\bar{p}f_0$ itself (assuming that the meson emission model is a reasonable guide). Given a somewhat larger event sample, $\psi' \to p\bar{p}f_0$ should be competitive with J/ψ, and has the advantage of more phase space, so the scalars near 1 GeV and the $f_0(1500)$ could also be investigated. $\eta_c \to p\bar{p}f_0$ has a comparable theoretical branching fraction, but the difficulty of producing the η_c makes this a less attractive channel. Finally, the χ_{cJ} states are predicted to have much smaller $p\bar{p}f_0$ branching fractions than $J/\psi \to p\bar{p}f_0$, and accordingly are less attractive experimentally if this decay model is accurate.

We have also estimated the effect of an $f_0(500)$ width on these results. Imposing a Breit-Wigner f_0 mass profile with $\Gamma_{f_0} = 0.5$ GeV, truncated at $2m_\pi$, decreases all the absolute theoretical $\Psi \to p\bar{p}f_0(500)$ branching fractions in Table II (column 3) by $\approx 10\%$. The *relative* theoretical branching fractions (column 2) are even less sensitive to the $f_0(500)$ width, and become 0.41, 0.048, 0.017, and 0.21.

A light scalar f_0 meson would presumably decay strongly and perhaps dominantly to $\pi\pi$, so decays of the type $\Psi \to p\bar{p}\pi\pi$ are of special interest, notably $J/\psi \to p\bar{p}\pi\pi$ (in view of our large theoretical $B(J/\psi \to p\bar{p}f_0(500))$). The charged case $J/\psi \to p\bar{p}\pi^+\pi^-$ has been studied by Mark-I [25], DESY [28], and Mark-II [27]. Although no light scalar mesons have yet been identified in this decay, it is suggestive that $J/\psi \to p\bar{p}\pi^+\pi^-$ is the largest known exclusive $J/\psi \to p\bar{p}X$ mode, with a branching fraction of $B(J/\psi \to p\bar{p}\pi^+\pi^-) = (6.0 \pm 0.5) \cdot 10^{-3}$.

TABLE II. Theoretical (meson emission model) branching fractions for light scalar meson production. The numerical columns are (1) the ratio $B(\Psi \to p\bar{p}f_0(500))/B(J/\psi \to p\bar{p}f_0(500))$; (2) $10^3 \cdot B(\Psi \to p\bar{p}f_0(500))$ for $g_{NNf_0} = 10$; (3) $10^3 \cdot B^{\text{expt}}(\Psi \to p\bar{p}\pi^+\pi^-)$, for comparison with (2). (See text.)

Ψ	$B^{\text{thy}}_{p\bar{p}f_0}/B_0$	$10^3 B^{\text{thy}(g=10)}_{p\bar{p}f_0}$	$10^3 B^{\text{expt}}_{p\bar{p}\pi^+\pi^-}$
η_c	0.40	1.4	<12 (90% C.L.)
J/ψ	$\equiv 1$	3.4	6.0 ± 0.5
χ_0	0.045	0.15	2.1 ± 0.7
χ_1	0.016	0.054	0.50 ± 0.19
ψ'	0.21	0.72	0.60 ± 0.04

In addition to the $p\bar{p}f_0$ intermediate state of interest here, this decay may also receive important contributions from NN^*, N^*N^*, and $\Delta\Delta$, as well as other two-baryon and NNm states; this may complicate the comparison with experiment considerably. Reference [27], which has the largest event sample, finds a large but not dominant $\Delta\Delta$ contribution, $B(J/\psi \to \Delta^{++}\bar{\Delta}^{--}) = (1.10 \pm 0.29) \cdot 10^{-3}$, and gives a rather tight upper limit of $\approx 5\%$ on the contributing subprocess $J/\psi \to p\bar{p}\rho^0$; $B(J/\psi \to p\bar{p}\rho^0) < 3.1 \cdot 10^{-4}$ (90% C.L.). As Ref. [27] shows in their Fig. 31, that the $\pi^+\pi^-$ invariant mass distribution from non-$\Delta\Delta$ events is a broad sigmalike distribution, there may well be a large $J/\psi \to p\bar{p}f_0(\sim 500) \to p\bar{p}\pi^+\pi^-$ contribution to this decay, with a branching fraction comparable to the theoretical $3.4 \cdot 10^{-3}$ predicted for $g_{NNf_0} = 10$ (see Table II). It will be very interesting to investigate this possible light f_0 contribution in a future experimental study, as well as to search for the $f_0(980)$ and $a_0(980)$ scalar states and the scalar glueball candidate $f_0(1500)$ in (higher-mass) charmonium decays, notably of the ψ'.

F. Decays to $NN\omega$ and NNV

Charmonium decays to $N\bar{N}\omega$ are especially interesting, since the ω plays a crucial role in meson exchange models of the NN force, as the dominant origin of the short-ranged "hard core repulsion," through t-channel ω exchange. Conceptual problems with this ω-exchange mechanism include (1) the very small NN separation implied by this mechanism ($R_{NN} \approx 1/m_V \approx 0.3$ fm), at which quark-gluon dynamics may be a more appropriate description of the interaction; and (2) the prediction of a corresponding short-ranged $N\bar{N}$ attraction and deeply bound $N\bar{N}$ states, which are not observed. (See, for example, Refs. [29–31], and references cited therein.)

There are two strong coupling constants in the $NN\omega$ vertex, as summarized by Eq. (5), the overall strength $g_{NN\omega}$ of the Dirac (γ_μ) coupling, and the relative strong magnetic Pauli coupling $\kappa_{NN\omega}$ (here abbreviated g_ω and κ_ω, with $\alpha_\omega = g^2_\omega/4\pi$). Unfortunately the NNV couplings in the meson exchange models are not *a priori* well established experimentally, and are therefore usually fitted directly to NN scattering data. These NN scattering studies are thus fits to the data rather than predictions that test the assumed vector-meson-exchange scattering mechanism. These NN fits typically find $g_\omega \approx 10$–15 for the Dirac $NN\omega$ coupling, whereas the $NN\omega$ Pauli coupling has remained poorly determined; examples of $NN\omega$ parameter

sets from the NN scattering literature include $(g_\omega, \kappa_\omega) = (12.2, -0.12)$ (Paris), $(12.5, +0.66)$ (Nijmegen), and $(15.9, 0)$ (CD-Bonn) (these are cited in Ref. [32]). Independent estimates of the $NN\omega$ coupling from experiment have been reported by Sato and Lee [33] (from pion photoproduction) and by Mergell, Meissner, and Drechsel [34] (from nucleon electromagnetic form factors). Sato *et al.* assumed $\kappa_\omega = 0$, and quoted the range $g_\omega = 7$–10.5 for experimentally favored values of the Dirac coupling. Mergell *et al.* found a small κ_ω but a much larger Dirac coupling, $(g_\omega, \kappa_\omega) = (20.86 \pm 0.25, -0.16 \pm 0.01)$. Theoretical calculations include a QCD sum rule result of Zhu [35], who finds $(g_\omega, \kappa_\omega) = (18 \pm 8, 0.8 \pm 0.4)$, and a recent $^3P_0$ quark model calculation of NNm couplings [32] which found the analytic result $\kappa_\omega = -3/2$.

Charmonium decays to $p\bar{p}\omega$ final states (and $N\bar{N}V$ more generally) may allow independent estimates of these $NN\omega$ and NNV couplings, again provided that they are dominated by the meson emission decay mechanism, or at least that this contribution to the decay amplitude can be isolated and quantified. In the following discussion we will consider the decay $J/\psi \to p\bar{p}\omega$ as an example.

Results from experimental studies of the decay $J/\psi \to p\bar{p}\omega$ have been published by Mark-I [25], Mark-II [27], and most recently BES-II [5]. The PDG value of the $J/\psi \to p\bar{p}\omega$ branching fraction, estimated from these results, is $B(J/\psi \to p\bar{p}\omega) = (1.10 \pm 0.15) \cdot 10^{-3}$, which combined with the PDG J/ψ total width gives an experimental partial width of

$$\Gamma(J/\psi \to p\bar{p}\omega) = 103 \pm 14 \text{ eV}. \tag{31}$$

The fact that this is approximately equal to the $p\bar{p}\pi^0$ partial width (19) despite the much smaller phase space suggests a robust $NN\omega$ coupling.

On evaluating this theoretical decay rate by integrating Eq. (15) numerically with physical masses, both $NN\omega$ couplings free, and (as used previously) $g_{J/\psi p\bar{p}} = 1.62 \cdot 10^{-3}$, we find

$$\Gamma(J/\psi \to p\bar{p}\omega) = \alpha_\omega \cdot (2.468 - 1.101\kappa_\omega + 0.886\kappa_\omega^2) \text{ eV}. \tag{32}$$

The single number $\Gamma(J/\psi \to p\bar{p}\omega)$ alone does not suffice to determine the $NN\omega$ strong couplings since there are two free parameters, g_ω and κ_ω. If we set $\kappa_\omega = 0$, following CD-Bonn [15] and the Sato-Lee photoproduction study [33], the measured partial width (31) and the theoretical decay rate (32) imply $g_\omega = 23 \pm 3$ (provided that meson emission dominates this decay). This g_ω is rather larger than these references prefer for g_ω; it is consistent however with the electromagnetic form factor fit of Mergell *et al.* [34] and the range 18 ± 8 reported by Zhu [35] from QCD sum rules. If we instead assume the $^3P_0$ quark model value $\kappa_\omega = -3/2$ for the Pauli term [32], we find $g_\omega = 14.6 \pm 2.0$, which is consistent with the values quoted by NN scattering studies, and is somewhat larger than the photoproduction value.

It is possible to estimate the two parameters g_ω and κ_ω independently through a more detailed comparison between $J/\psi \to p\bar{p}\omega$ data and the theoretical DP event density, Eq. (15). This theoretical event density is strongly dependent on the Pauli coefficient κ_ω; with $\kappa_\omega = 0$ the event density at lower $M_{p\bar{p}}$ is strongly suppressed (see Fig. 4).

In contrast, for moderately large $|\kappa_\omega|$, such as the quark model value $\kappa_\omega = -3/2$, the theoretical DP event density is closer to uniform. This is illustrated in Fig. 5, which shows this event density along the diagonal $M^2_{p\omega} = M^2_{\bar{p}\omega}$ (relative to the maximum value on diagonal) for various $\kappa_\omega \le 0$. If the meson emission model does give a good description of this decay, evidently it may be possible to determine κ_ω by comparing the $J/\psi \to p\bar{p}\omega$ DP event density on diagonal to the prediction in Fig. 5.

G. Other $\Psi \to p\bar{p}V$ decays

Other decays to $p\bar{p}V$ final states that are closely related to $J/\psi \to p\bar{p}\omega$ include $J/\psi \to p\bar{p}\rho^0$ and $J/\psi \to p\bar{p}\phi$. In the meson emission model these are both described by the decay formula (15), albeit with different vector meson masses and NNV couplings. Given the rounded PDG masses $m_{\rho^0} = 0.7755$ GeV and $m_\phi = 1.0195$ GeV, we predict the numerical decay widths

$$\Gamma(J/\psi \to p\bar{p}\rho^0) = \alpha_\rho \cdot (2.614 - 1.155\kappa_\rho + 0.930\kappa_\rho^2) \text{ eV} \tag{33}$$

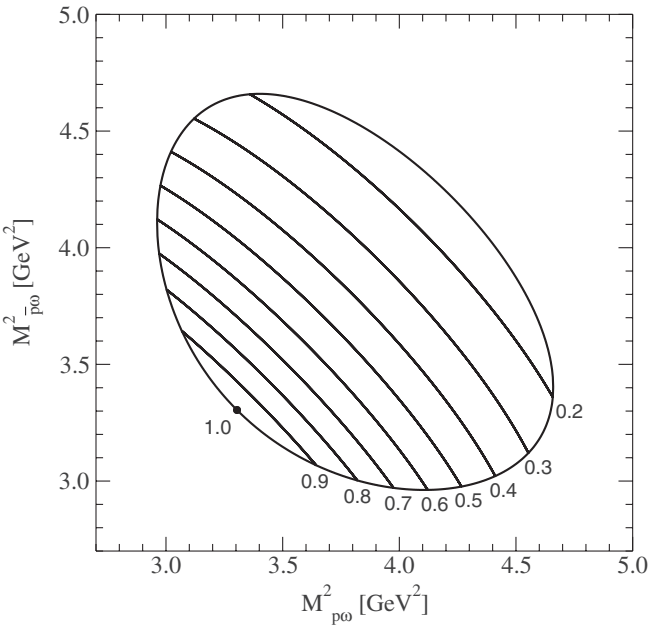

FIG. 4. Theoretical relative $J/\psi \to p\bar{p}\omega$ DP event density for $\kappa_\omega = 0$, from Eq. (15). Note the suppression near $p\bar{p}$ threshold (upper right).

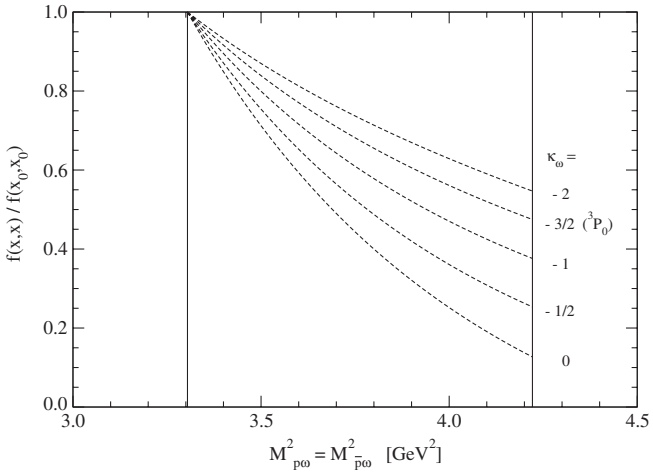

FIG. 5. Theoretical $J/\psi \to p\bar{p}\omega$ DP event density along the diagonal $M^2_{p\omega} = M^2_{\bar{p}\omega}$, showing the strong κ_ω dependence.

and

$$\Gamma(J/\psi \to p\bar{p}\phi) = \alpha_\phi \cdot (0.184 - 0.109\kappa_\phi + 0.087\kappa_\phi^2)\ \text{eV}. \tag{34}$$

The ρ^0 case is especially interesting due to the range of values reported for κ_ρ, as discussed by Brown and Machleidt [36]. Although vector dominance predicts $\kappa_\rho = 3.7$ "weak ρ," and some data have been interpreted as supporting this, fits to $\pi\pi \to N\bar{N}$ and S-D mixing in NN scattering prefer a larger value "strong ρ"; the Bonn potential model, for example, uses $(\alpha_\rho, \kappa_\rho) = (0.84, 6.1)$ [14]. A QCD sum rule calculation by Zhu [37] finds $(g_\rho, \kappa_\rho) = (2.5 \pm 0.2, 8.0 \pm 2.0)$, comparable to the fitted Bonn values. In contrast, the valence quark model with a $^3P_0$ $NN\rho$ coupling predicts a much smaller $\kappa_\rho = -\kappa_\omega = +3/2$ [32].

Using Eq. (33) we can give meson emission model predictions for $\Gamma(J/\psi \to p\bar{p}\rho^0)$ that follow from these various (g_ρ, κ_ρ) parameters. The Bonn parameters cited above give $\Gamma(J/\psi \to p\bar{p}\rho^0) = 25$ eV and $B(J/\psi \to p\bar{p}\rho^0) = 2.7 \cdot 10^{-4}$; this is essentially equal to the current experimental upper limit [24,27] of $3.1 \cdot 10^{-4}$ (90% C.L.), which is a Mark-II result dating from 1984. The Zhu QCD sum rule central values for (g_ρ, κ_ρ) give essentially identical results. In contrast the valence quark model with $^3P_0$ couplings $g_\rho = g_\omega/3$ and $\kappa_\rho = +3/2$ (and using $g_\rho = 14.6$ from the $J/\psi \to p\bar{p}\omega$ discussion above) gives a much lower $\Gamma(J/\psi \to p\bar{p}\rho^0) = 5.6$ eV and hence $B(J/\psi \to p\bar{p}\rho^0) = 6.0 \cdot 10^{-5}$, which is about a factor of 5 below the current experimental limit. The proximity of the Bonn and QCD sum rule parameter predictions for $B(J/\psi \to p\bar{p}\rho^0)$ to the current limit suggests that an experimental study with significantly improved sensitivity could make a useful contribution to establishing $NN\rho$ couplings.

The decay $J/\psi \to p\bar{p}\phi$ in contrast *has* been observed, and has an experimental (PDG) branching fraction of $B^{\text{expt}}(J/\psi \to p\bar{p}\phi) = (4.5 \pm 1.5) \cdot 10^{-5}$, corresponding to $\Gamma^{\text{expt}}(J/\psi \to p\bar{p}\phi) = 4.2 \pm 1.4$ eV. Unfortunately in this case we do not have a theoretical estimate for either α_ϕ or κ_ϕ, since the (valence level, leading-order) $^3P_0$ model predicts no $NN\phi$ coupling. Clearly it would be very interesting to obtain experimental values for these couplings, since little is known about the properties of Zweig-suppressed vertices. Again, if the meson emission model gives a good description of this decay, a comparison of Eq. (15) to the experimental $J/\psi \to p\bar{p}\phi$ DP event distribution should allow an experimental determination of the $NN\phi$ couplings.

Finally, we note in passing that ψ' decays to NNV are apparently not in agreement with the meson emission model; proceeding as above, we would predict a branching fraction of $B(\psi' \to p\bar{p}\omega) = 9.4 \cdot 10^{-4}$, whereas the PDG experimental value is an order of magnitude smaller, $B^{\text{expt}}(\psi' \to p\bar{p}\omega) = (6.9 \pm 2.1) \cdot 10^{-5}$. Possible explanations for this discrepancy, including form factors and (destructive interference with) additional decay mechanisms, are discussed in the next section. Since the total $\psi' \to p\bar{p}\omega$ data sample reported by CLEO [11] and BES [12] comprises only about 35 events, it is not yet possible to establish the reason for this large discrepancy between experiment and the meson emission model. This would ideally involve a comparison between the predicted and observed Dalitz plot event densities. Hopefully this comparison will be possible using the large ψ' data set being accumulated at BES-III.

IV. SUMMARY, CONCLUSIONS, AND FUTURE DEVELOPMENTS

In this paper we have presented and developed a hadron-level "meson emission model" of charmonium decays of the type $\Psi \to N\bar{N}m$, where Ψ is a generic charmonium resonance, N is a nucleon, and m is a light meson. The model assumes that the decays take place through meson emission from the nucleon or antinucleon line, as a hadronic "final state radiation" correction to a $\Psi \to N\bar{N}$ transition. As the model is relatively simple, we are able to evaluate the predicted DP event densities for many experimentally accessible and measured processes; in particular, we give event densities for $\Psi = \eta_c, J/\psi$ (and ψ'), χ_{c0}, χ_{c1}, and ψ'; and $m = \pi^0, f_0$, and ω; and implicitly all cases with the same J^{PC} quantum numbers.

We used the reaction $J/\psi \to p\bar{p}\pi^0$ as a test case with no free parameters (the $J/\psi p\bar{p}$ and $NN\pi$ couplings are known), and compared the meson emission model predictions for the projected event density in $M_{p\pi}$ and the partial width $\Gamma(J/\psi \to p\bar{p}\pi^0)$ to experiment; the partial width is in good agreement, and the $M_{p\pi}$ event density appears to describe the non-N^* background contribution to this reaction observed experimentally. We also give predictions for

$\Gamma(\Psi \to p\bar{p}\pi^0)$ for all Ψ cases considered here; the overall trend of large and small widths, and their approximate scale is reproduced by the model.

We also considered scalar and vector meson production. We estimated $\Psi \to p\bar{p}f_0$ branching fractions for a light $f_0(500)$, and noted that the J/ψ and ψ' are favored for these studies, and the ψ' is favored for glueball searches. In vector production we considered $J/\psi \to p\bar{p}\omega$ in particular, and noted that a high-statistics study of this reaction could be used to estimate the $NN\omega$ couplings (g_ω and κ_ω), which play a crucial role in meson exchange models of the NN force. We showed that the $J/\psi \to p\bar{p}\omega$ Dalitz plot event density is rather sensitive to the poorly known $NN\omega$ Pauli coupling κ_ω. Determination of meson-nucleon strong couplings is a potentially very interesting application of $\Psi \to p\bar{p}m$ decays.

There are several theoretical developments that will be very important for future applications of this model. One should incorporate N^* resonances; this is conceptually straightforward but may be technically complicated, as it will introduce many new and poorly known resonance coupling parameters and phases. This development is of course crucial to describe the data in reactions such as $J/\psi \to p\bar{p}\pi^0$, which clearly shows N^* resonance peaks (Fig. 3). Another important development is the substitution of plausible $\Psi N^{(*)}\bar{N}^{(*)}$ and $N^{(*)}Nm$ hadron vertex form factors for the assumed coupling constants; the difficulty here is that hadronic form factors are poorly known, and models such as $^3P_0$ that predict form factors have not been adequately developed and tested. Another interesting generalization of the strong vertices assumed here would be to include a $J/\psi p\bar{p}$ Pauli coupling; as we noted previously [23], this can explain the observed $e^+e^- \to J/\psi \to p\bar{p}$ angular distribution. Finally, one should include other significant decay mechanisms, as they become apparent through high-statistics studies of experimental Dalitz plots. These additional mechanisms might include intermediate meson resonances m' that couple strongly to $N\bar{N}$, as in $\Psi \to m'm \to p\bar{p}m$; if the m' resonances lie in the physical region, they will give rise to characteristic m' resonance bands in $M_{p\bar{p}}$ that could be identified and incorporated in a more complete decay model.

ACKNOWLEDGMENTS

We are happy to acknowledge useful communications with R. Mitchell, K. Seth, M. Shepherd, E. S. Swanson, and B. S. Zou regarding this research, and Shu-Min Li and Xiao-Yan Shen in particular for contributing the BES data used in preparing Fig. 3. We also gratefully acknowledge the support of the Department of Physics and Astronomy of the University of Tennessee, the Physics Division of Oak Ridge National Laboratory, and the Department of Physics, the College of Arts and Sciences, and the Office of Research at Florida State University. This research was sponsored in part by the Office of Nuclear Physics, U.S. Department of Energy.

[1] M. Ablikim *et al.* (BES Collaboration), Phys. Rev. D **80**, 052004 (2009).
[2] M. Ablikim *et al.* (BES Collaboration), Phys. Rev. D **71**, 072006 (2005).
[3] M. Ablikim *et al.* (BES Collaboration), Phys. Rev. D **74**, 012004 (2006).
[4] M. Ablikim *et al.* (BES Collaboration), arXiv:0902.3501.
[5] M. Ablikim *et al.* (BES Collaboration), Eur. Phys. J. C **53**, 15 (2008).
[6] J. Z. Bai *et al.* (BES Collaboration), Phys. Rev. Lett. **91**, 022001 (2003).
[7] M. Ablikim *et al.* (BES Collaboration), Phys. Rev. Lett. **95**, 262001 (2005).
[8] Y. Huang, "Confirmation of proton-antiproton mass threshold enhancement structure and X(1835) at BES-III" in Proceedings of HADRON 2009, Florida State University, Tallahassee (unpublished).
[9] A. Lundborg, T. Barnes, and U. Wiedner, Phys. Rev. D **73**, 096003 (2006).
[10] M. Kotulla *et al.* ($\bar{\text{P}}$ANDA Collaboration), "*Technical Progress Report for* $\bar{\text{P}}$ANDA*, Strong Interaction Studies with Antiprotons*," 2005 (unpublished).
[11] R. A. Briere *et al.* (CLEO Collaboration), Phys. Rev. Lett. **95**, 062001 (2005).
[12] J. Z. Bai *et al.* (BES Collaboration), Phys. Rev. D **67**, 052002 (2003).
[13] S. B. Athar *et al.* (CLEO Collaboration), Phys. Rev. D **75**, 032002 (2007).
[14] R. Machleidt, K. Holinde, and C. Elster, Phys. Rep. **149**, 1 (1987).
[15] R. Machleidt, Phys. Rev. C **63**, 024001 (2001).
[16] M. M. Nagels, T. A. Rijken, and J. J. de Swart, Phys. Rev. D **15**, 2547 (1977).
[17] M. M. Nagels, T. A. Rijken, and J. J. de Swart, Phys. Rev. D **20**, 1633 (1979).
[18] V. G. J. Stoks, R. A. M. Klomp, C. P. F. Terheggen, and J. J. de Swart, Phys. Rev. C **49**, 2950 (1994).
[19] W. N. Cottingham, M. Lacombe, B. Loiseau, J. M. Richard, and R. Vinh Mau, Phys. Rev. D **8**, 800 (1973).
[20] M. Lacombe, B. Loiseau, J. M. Richard, R. Vinh Mau, J. Conte, P. Pires, and R. de Tourreil, Phys. Rev. C **21**, 861 (1980).
[21] C. Downum and D. Phil, Oxford University, 2009 (unpublished).
[22] T. Barnes and X. Li, Phys. Rev. D **75**, 054018 (2007).

[23] T. Barnes, X. Li, and W. Roberts, Phys. Rev. D **77**, 056001 (2008).
[24] C. Amsler *et al.* (Particle Data Group), Phys. Lett. B **667**, 1 (2008), and 2009 partial update for the 2010 edition.
[25] I. Peruzzi *et al.*, Phys. Rev. D **17**, 2901 (1978).
[26] R. Brandelik *et al.* (DASP Collaboration), Z. Phys. C **1**, 233 (1979).
[27] M. W. Eaton *et al.*, Phys. Rev. D **29**, 804 (1984).
[28] H. J. Besch *et al.*, Z. Phys. C **8**, 1 (1981).
[29] K. Maltman and N. Isgur, Phys. Rev. Lett. **50**, 1827 (1983).
[30] K. Maltman and N. Isgur, Phys. Rev. D **29**, 952 (1984).
[31] T. Barnes, S. Capstick, M. D. Kovarik, and E. S. Swanson, Phys. Rev. C **48**, 539 (1993).
[32] C. Downum, T. Barnes, J. R. Stone, and E. S. Swanson, Phys. Lett. B **638**, 455 (2006).
[33] T. Sato and T. S. H. Lee, Phys. Rev. C **54**, 2660 (1996).
[34] P. Mergell, U. G. Meissner, and D. Drechsel, Nucl. Phys. **A596**, 367 (1996).
[35] Shi-Lin Zhu, Phys. Rev. C **59**, 3455 (1999).
[36] G. E. Brown and R. Machleidt, Phys. Rev. C **50**, 1731 (1994).
[37] Shi-Lin Zhu, Phys. Rev. C **59**, 435 (1999).

Bibliography

Bibliography

[1] G. Ruthemann, Annalen der Physik, **437**, 113 (1948).

[2] C. J. Powell and J. B. Swan, Phys. Rev., **116**, 81 (1959).

[3] C. J. Powell and J. B. Swan, Phys. Rev., **115**, 869 (1959).

[4] D. R. Smith, J. B. Pendry, and M. C. K. Wiltshire, Science, **305**, 788 (2004).

[5] J. Pendry, Nat Mater, **5**, 599 (2006).

[6] T. Ando, A. B. Fowler, and F. Stern, Rev. Mod. Phys., **54**, 437 (1982).

[7] M. Z. Hasan and C. L. Kane, Rev. Mod. Phys., **82**, 3045 (2010).

[8] I. Žutić, J. Fabian, and S. Das Sarma, Rev. Mod. Phys., **76**, 323 (2004).

[9] M. N. Baibich, *et al.*, Phys. Rev. Lett., **61**, 2472 (1988).

[10] R. T. Tung, Materials Science and Engineering: R: Reports, **35**, 1 (2001).

[11] S. K. Cheung and N. W. Cheung, Applied Physics Letters, **49**, 85 (1986).

[12] M. W. Knight, H. Sobhani, P. Nordlander, and N. J. Halas, Science, **332**, 702 (2011).

[13] F. D. M. Haldane, Journal of Physics C: Solid State Physics, **14**, 2585 (1981).

[14] M. Imada, A. Fujimori, and Y. Tokura, Rev. Mod. Phys., **70**, 1039 (1998).

[15] B. Renker, *et al.*, Phys. Rev. Lett., **30**, 1144 (1973).

[16] P. T. Sprunger, *et al.*, Science, **275**, 1764 (1997).

[17] J. M. Pitarke, V. M. Silkin, E. V. Chulkov, and P. M. Echenique, Reports on Progress in Physics, **70**, 1 (2007).

[18] H. Xu, E. J. Bjerneld, M. Käll, and L. Börjesson, Phys. Rev. Lett., **83**, 4357 (1999).

[19] K. Kneipp *et al.*, Phys. Rev. Lett., **78**, 1667 (1997).

[20] H. A. Atwater and A. Polman, Nature Mater., **9**, 205 (2010).

[21] D. Pines and D. Bohm, Phys. Rev., **85**, 338 (1952).

[22] R. H. Ritchie, Phys. Rev., **106**, 874 (1957).

[23] G. M. Harris, Phys. Rev., **125**, 1131 (1962).

[24] P. J. Feibelman, Phys. Rev. B, **9**, 5077 (1974).

[25] P. Drude, Annalen der Physik, **306**, 566 (1900).

[26] N. W. Ashcroft and N. D. Mermin, *Solid State Physics* (Saunders College, Philadelphia, 1976).

[27] C. W. J. Beenakker, Rev. Mod. Phys., **69**, 731 (1997).

[28] R. Landauer, Philosophical Magazine, **21**, 863 (1970).

[29] P. Hohenberg and W. Kohn, Phys. Rev., **136**, B864 (1964).

[30] W. Kohn and L. J. Sham, Phys. Rev., **140**, A1133 (1965).

[31] R. Lake, G. Klimeck, R. C. Bowen, and D. Jovanovic, J. Appl. Phys., **81**, 7845 (1997).

[32] M. P. L. Sancho, J. M. L. Sancho, and J. Rubio, J. Phys. F: Met. Phys, **14**, 1205 (1984).

[33] U. Kreibig and M. Volmer, *Optical Properties of Metal Clusters* (Springer-Verlag, Berlin, 1995).

[34] W. L. Barnes, A. Dereux, and T. W. Ebbesen, Nature, **424**, 824 (2003).

[35] E. Ozbay, Science, **311**, 189 (2006).

[36] J. N. Anker *et al.*, Nature Mater., **7**, 442 (2008).

[37] K. Matsubara, S. Kawata, and S. Minami, Appl. Opt., **27**, 1160 (1988).

[38] W. Srituravanich *et al.*, Nano Lett., **4**, 1085 (2004).

[39] X. Luo and T. Ishihara, Appl. Phys. Lett., **84**, 4780 (2004).

[40] J. Zuloaga, E. Prodan, and P. Nordlander, Nano Lett., **9**, 887 (2009).

[41] K. Zhao, *et al.*, Phys. Rev. Lett., **102**, 186804 (2009).

[42] J.-J. Chang and D. C. Langreth, Phys. Rev. B, **5**, 3512 (1972).

[43] J.-J. Chang and D. C. Langreth, Phys. Rev. B, **8**, 4638 (1973).

[44] T. R. Jensen, M. D. Malinsky, C. L. Haynes, and R. P. Van Duyne, J. Phys. Chem. B, **104**, 10549 (2000).

[45] E. Prodan and P. Nordlander, Nano Lett., **3**, 543 (2003).

[46] E. Zaremba and B. N. J. Persson, Phys. Rev. B, **35**, 596 (1987).

[47] T. Klar *et al.*, Phys. Rev. Lett., **80**, 4249 (1998).

[48] F. Stietz *et al.*, Phys. Rev. Lett., **84**, 5644 (2000).

[49] U. Kreibig and C. v. Fragstein, Z. Physik, **224**, 307 (1969).

[50] A. Kawabata and R. Kubo, J. Phys. Soc. Japan, **21**, 1765 (1966).

[51] Z. Yuan and S. Gao, Phys. Rev. B, **73**, 155411 (2006).

[52] A. G. Eguiluz, Phys. Rev. Lett., **51**, 1907 (1983).

[53] W. Ekardt, Phys. Rev. B, **31**, 6360 (1985).

[54] E. Prodan and P. Nordlander, Chem. Phys. Lett., **352**, 140 (2002).

[55] Z. Yuan and S. Gao, Surf. Sci., **602**, 460 (2008).

[56] E. Prodan and P. Nordlander, J. Chem. Phys., **120**, 5444 (2004).

[57] E. Prodan, C. Radloff, N. J. Halas, and P. Nordlander, Science, **302**, 419 (2003).

[58] C. Yannouleas, E. Vigezzi, and R. A. Broglia, Phys. Rev. B, **47**, 9849 (1993).

[59] K.-D. Tsuei, *et al.*, Phys. Rev. Lett., **64**, 44 (1990).

[60] K. D. Tsuei, *et al.*, Surface Science, **247**, 302 (1991).

[61] P. T. Sprunger, G. M. Watson, and E. W. Plummer, Surface Science, **269-270**, 551 (1992).

[62] H. Ishida and A. Liebsch, Phys. Rev. B, **54**, 14127 (1996).

[63] A. J. Bennett, Phys. Rev. B, **1**, 203 (1970).

[64] C. Kunz, Zeitschrift für Physik A Hadrons and Nuclei, **196**, 311 (1966-08-01).

[65] K.-D. Tsuei, E. W. Plummer, and P. J. Feibelman, Phys. Rev. Lett., **63**, 2256 (1989).

[66] J. A. Gaspar, A. G. Eguiluz, K.-D. Tsuei, and E. W. Plummer, Phys. Rev. Lett., **67**, 2854 (1991).

[67] G. Chiarello, *et al.*, Phys. Rev. B, **55**, 1376 (1997).

[68] S. R. Barman, *et al.*, Phys. Rev. B, **64**, 195410 (2001).

[69] A. Liebsch, Phys. Rev. Lett., **67**, 2858 (1991).

[70] A. Liebsch, B.-O. Kim, and E. W. Plummer, Phys. Rev. B, **63**, 125416 (2001).

[71] K. S. Novoselov, *et al.*, Science, **306**, 666 (2004).

[72] A. H. C. Neto, *et al.*, Rev. Mod. Phys., **81**, 109 (2009).

[73] A. K. Geim, Science, **324**, 1530 (2009).

[74] A. K. Geim and K. S. Novoselov, Nat Mater, **6**, 183 (2007).

[75] M. I. Katsnelson, Eur. Phys. J. B, **51**, 157 (2006).

[76] M. I. Katsnelson, K. S. Novoselov, and A. K. Geim, Nat Phys, **2**, 620 (2006).

[77] X. Du, I. Skachko, A. Barker, and E. Y. Andrei, Nat Nano, **3**, 491 (2008).

[78] S. V. Morozov, *et al.*, Phys. Rev. Lett., **100**, 016602 (2008).

[79] K. I. Bolotin, *et al.*, Solid State Commun, **146**, 351 (2008).

[80] K. S. Novoselov, *et al.*, Nature, **438**, 197 (2005).

[81] Y. Zhang, Y.-W. Tan, H. L. Stormer, and P. Kim, Nature, **438**, 201 (2005).

[82] K. S. Novoselov, *et al.*, Nat Phys, **2**, 177 (2006).

[83] E. McCann and V. I. Fal'ko, Phys. Rev. Lett., **96**, 086805 (2006).

[84] R. N. Costa Filho, G. A. Farias, and F. M. Peeters, Phys. Rev. B, **76**, 193409 (2007).

[85] Y.-W. Son, M. L. Cohen, and S. G. Louie, Nature, **444**, 347 (2006).

[86] M. Koshino and T. Ando, Phys. Rev. B, **73**, 245403 (2006).

[87] M. I. Katsnelson, Eur. Phys. J. B, **52**, 151 (2006).

[88] T. Ludwig, Phys. Rev. B, **75**, 195322 (2007).

[89] I. Snyman and C. W. J. Beenakker, Phys. Rev. B, **75**, 045322 (2007).

[90] J. Cserti, A. Csordás, and G. Dávid, Phys. Rev. Lett., **99**, 066802 (2007).

[91] R. V. Gorbachev, *et al.*, Phys. Rev. Lett., **98**, 176805 (2007).

[92] J. Nilsson, A. H. C. Neto, F. Guinea, and N. M. R. Peres, Phys. Rev. B, **76**, 165416 (2007).

[93] J. Nilsson and A. H. C. Neto, Phys. Rev. Lett., **98**, 126801 (2007).

[94] S. Adam and S. D. Sarma, Phys. Rev. B, **77**, 115436 (2008).

[95] E. A. Henriksen, *et al.*, Phys. Rev. Lett., **100**, 087403 (2008).

[96] B. Sahu, H. Min, A. H. MacDonald, and S. K. Banerjee, Phys. Rev. B, **78**, 045404 (2008).

[97] J. Nilsson, A. H. C. Neto, F. Guinea, and N. M. R. Peres, Phys. Rev. B, **78**, 045405 (2008).

[98] I. Martin, Y. M. Blanter, and A. F. Morpurgo, Phys. Rev. Lett., **100**, 036804 (2008).

[99] D. S. L. Abergel and T. Chakraborty, Applied Physics Letters, **95**, 062107 (2009).

[100] D. Culcer and R. Winkler, Phys. Rev. B, **79**, 165422 (2009).

[101] H. Xu, T. Heinzel, and I. V. Zozoulenko, Phys. Rev. B, **80**, 045308 (2009).

[102] S. Park and H.-S. Sim, Phys. Rev. Lett., **103**, 196802 (2009).

[103] E. McCann, Phys. Rev. B, **74**, 161403 (2006).

[104] T. Ohta, *et al.*, Science, **313**, 951 (2006).

[105] H. Min, B. Sahu, S. K. Banerjee, and A. H. MacDonald, Phys. Rev. B, **75**, 155115 (2007).

[106] E. V. Castro, *et al.*, Phys. Rev. Lett., **99**, 216802 (2007).

[107] Y. Zhang, *et al.*, Nature, **459**, 820 (2009).

[108] S. H. Abedinpour, *et al.*, Phys. Rev. Lett., **99**, 206802 (2007).

[109] H. Min, G. Borghi, M. Polini, and A. H. MacDonald, Phys. Rev. B, **77**, 041407 (2008).

[110] P. San-Jose, E. Prada, E. McCann, and H. Schomerus, Phys. Rev. Lett., **102**, 247204 (2009).

[111] M. Fujita, K. Wakabayashi, K. Nakada, and K. Kusakabe, J. Phys. Soc. Jpn., **65**, 1920 (1996).

[112] K. Nakada, M. Fujita, G. Dresselhaus, and M. S. Dresselhaus, Phys. Rev. B, **54**, 17954 (1996).

[113] K. Wakabayashi, Phys. Rev. B, **64**, 125428 (2001).

[114] W. Liu, *et al.*, Phys. Rev. B, **80**, 233405 (2009).

[115] E. V. Castro, *et al.*, Phys. Rev. Lett., **100**, 026802 (2008).

[116] R. E. Peierls, Helv. phys. Acta, **7** (1924).

[117] R. E. Peierls, Ann. Inst. Henri Poincaré, **5**, 177 (1935).

[118] L. D. Landau, Phys. Z. SU, **11**, 26 (1937).

[119] N. D. Mermin, Phys. Rev., **176**, 250 (1968).

[120] P. R. Wallace, Phys. Rev., **71**, 622 (1947).

[121] T. Ando, Phys. Rev. B, **44**, 8017 (1991).

[122] K. Wakabayashi and M. Sigrist, Phys. Rev. Lett., **84**, 3390 (2000).

[123] S. Krompiewski, J. Martinek, and J. Barnaś, Phys. Rev. B, **66**, 073412 (2002).

[124] K. Wakabayashi, J. Phys. Soc. Jpn., **71**, 2500 (2002).

[125] M. Evaldsson, I. V. Zozoulenko, H. Xu, and T. Heinzel, Phys. Rev. B, **78**, 161407 (2008).

[126] T. C. Li and S.-P. Lu, Phys. Rev. B, **77**, 085408 (2008).

[127] T. Low, Phys. Rev. B, **80**, 205423 (2009).

[128] T. Low and J. Appenzeller, Phys. Rev. B, **80**, 155406 (2009).

[129] K. Wakabayashi, Y. Takane, M. Yamamoto, and M. Sigrist, Carbon, **47**, 124 (2009).

[130] E. R. Mucciolo, A. H. Castro Neto, and C. H. Lewenkopf, Phys. Rev. B, **79**, 075407 (2009).

[131] X. Jia, *et al.*, Science, **323**, 1701 (2009).

[132] A. Rycerz, J. Tworzydlo, and C. W. J. Beenakker, Nat Phys, **3**, 172 (2007).

[133] D. A. Areshkin, D. Gunlycke, and C. T. White, Nano Letters, **7**, 204 (2006).

[134] L. Chico, L. X. Benedict, S. G. Louie, and M. L. Cohen, Phys. Rev. B, **54**, 2600 (1996).

[135] H. Chen, W. Zhu, and Z. Zhang, Phys. Rev. Lett., **104**, 186101 (2010).

[136] E. Loginova, *et al.*, Phys. Rev. B, **80**, 085430 (2009).

[137] P. W. Sutter, J.-I. Flege, and E. A. Sutter, Nat Mater, **7**, 406 (2008).

[138] E. L. et al, New Journal of Physics, **10** (2008).

[139] X. Li, W. Cai, L. Colombo, and R. S. Ruoff, Nano Letters, **9**, 4268 (2009).

[140] E. Loginova, N. C. Bartelt, P. J. Feibelman, and K. F. McCarty, New Journal of Physics, **11**, 063046 (2009).

[141] J. Wintterlin and M. L. Bocquet, Surface Science, **603**, 1841 (2009).

[142] Q. Yu, *et al.*, Applied Physics Letters, **93**, 113103 (2008).

[143] P. Lacovig, *et al.*, Phys. Rev. Lett., **103**, 166101 (2009).

[144] J. Coraux, *et al.*, New Journal of Physics, **11**, 023006 (2009).

[145] K. F. McCarty, P. J. Feibelman, E. Loginova, and N. C. Bartelt, Carbon, **47**, 1806 (2009).

[146] K. S. Kim, *et al.*, Nature, **457**, 706 (2009).

[147] S. Marchini, S. Günther, and J. Wintterlin, Phys. Rev. B, **76**, 075429 (2007).

[148] R. van Gastel, *et al.*, Applied Physics Letters, **95**, 121901 (2009).

[149] J. Coraux, A. T. N'Diaye, C. Busse, and T. Michely, Nano Letters, **8**, 565 (2008).

[150] A. T. N'Diaye, S. Bleikamp, P. J. Feibelman, and T. Michely, Phys. Rev. Lett., **97**, 215501 (2006).

[151] P. Sutter, J. T. Sadowski, and E. Sutter, Phys. Rev. B, **80**, 245411 (2009).

[152] A. N. Sidorov, *et al.*, Nanotechnology, **18**, 135301 (2007).

[153] Y. Miyamoto, H. Zhang, and D. Tománek, Phys. Rev. Lett., **104**, 208302 (2010).

[154] M. J. Shea and R. N. Compton, Phys. Rev. B, **47**, 9967 (1993).

[155] R. H. Ritchie, J. R. Manson, and P. M. Echenique, Phys. Rev. B, **49**, 2963 (1994).

[156] H.-J. Ernst, F. Charra, and L. Douillard, Science, **279**, 679 (1998).

[157] R. Jin, *et al.*, Science, **294**, 1901 (2001).

[158] R. Jin, *et al.*, Nature, **425**, 487 (2003).

[159] M. Brandbyge, *et al.*, Phys. Rev. B, **52**, 6042 (1995).

[160] T. Barnes, X. Li, and W. Roberts, Phys. Rev. D, **81**, 034025 (2010).

[161] T. Barnes, X. Li, and W. Roberts, Phys. Rev. D, **77**, 056001 (2008).

[162] T. Barnes and X. Li, Phys. Rev. D, **75**, 054018 (2007).

Vita

Xiaoguang Li was born at Chengdu, China on Oct. 13, 1980. After graduating from Shude high school, he entered University of Science and Technology of China at Hefei, where he spent five years as an undergraduate student in department of modern physics. In August of 2004, he came to the University of Tennessee to pursue PhD in physics and started research with Prof. Ted Barnes in high energy physics. In fall of 2008, he joined Prof. Zhenyu Zhang's group to work on condensed matter physics and finish a series of works in this thesis. In summer of 2010, he married his wife Ruochen Li in Miami. he completed his Doctor of Philosophy degree in 2011.